TU/e EINDHOVEN UNIVERSITY OF TECHNOLOGY

Concepts in theoretical heterogeneous catalytic reactivity

Citation for published version (APA):
Santen, van, R. A., & Neurock, M. (1995). Concepts in theoretical heterogeneous catalytic reactivity. *Catalysis Reviews : Science and Engineering*, *37*(4), 557-698. https://doi.org/10.1080/01614949508006451

DOI:
10.1080/01614949508006451

Document status and date:
Published: 01/01/1995

Document Version:
Publisher's PDF, also known as Version of Record (includes final page, issue and volume numbers)

Please check the document version of this publication:

• A submitted manuscript is the version of the article upon submission and before peer-review. There can be important differences between the submitted version and the official published version of record. People interested in the research are advised to contact the author for the final version of the publication, or visit the DOI to the publisher's website.
• The final author version and the galley proof are versions of the publication after peer review.
• The final published version features the final layout of the paper including the volume, issue and page numbers.

Link to publication

General rights
Copyright and moral rights for the publications made accessible in the public portal are retained by the authors and/or other copyright owners and it is a condition of accessing publications that users recognise and abide by the legal requirements associated with these rights.

• Users may download and print one copy of any publication from the public portal for the purpose of private study or research.
• You may not further distribute the material or use it for any profit-making activity or commercial gain
• You may freely distribute the URL identifying the publication in the public portal.

If the publication is distributed under the terms of Article 25fa of the Dutch Copyright Act, indicated by the "Taverne" license above, please follow below link for the End User Agreement:

www.tue.nl/taverne

Take down policy
If you believe that this document breaches copyright please contact us at:

openaccess@tue.nl

providing details and we will investigate your claim.

Download date: 25. Aug. 2022

CATAL. REV.—SCI. ENG., 37(4), 557–698 (1995)

Concepts in Theoretical Heterogeneous Catalytic Reactivity

RUTGER A. VAN SANTEN

Schuit Institute of Catalysis
Faculty of Chemical Engineering
Eindhoven University of Technology
Eindhoven, The Netherlands

MATTHEW NEUROCK

DuPont Central Research and Development
Experimental Station
Wilmington, Delaware 19880-0262, USA

Copyright © 1995 by Marcel Dekker, Inc.

I. INTRODUCTION

A. General

The heart of many commercial catalytic processes involves chemistry on transition metal particles and surfaces. The success in designing active surface ensembles, promoters, and selective poisons is inevitably tied to our knowledge of the fundamental principles which control transition metal surface chemistry. One extreme would be the rigorous description and energetic predictions for each elementary reaction step of an entire catalytic cycle from first-principle theoretical methods. While desirable, this has to date been an unattainable goal due to the limitations in both raw computer (CPU) requirements and the accuracy of the available computational methods. Recent advances in both quantum-chemical methods and computational resources, however, are driving this goal closer to reality. Theoretical treatments of adsorbate–surface interactions have rapidly advanced to the stage where detailed understandings of the governing structural and electronic features are readily available. In many cases, reliable quantitative predictions of the structure and energetics can also be made. While an exhaustive review of all theoretical treatments of adsorbate surface interactions and catalytic reactivity would be of great value, the tremendous volume published in this area makes this a difficult goal. Instead, we high-

light a set of essential theoretical concepts which govern important aspects of surface reactivity and describe how they dictate both activity and selectivity. We specifically target the catalytic chemist and reaction engineer, with the hope that these concepts will lead to a more advanced set of levers to aid and facilitate the design of new and improved catalyst formulations and optimal operating conditions.

The philosophy above is, in many ways, a theoretical complement to some of the ideas recently expressed by Dumesic et al. [1]. The general goal of both is the prediction of measurable catalytic kinetics based on mechanistic information for every elementary reaction step in the overall cycle, as well as competing surface phenomena operative at catalytic conditions.

A fundamental understanding of the kinetics of heterogeneous catalytic systems, however, is complex due to the multisite nature of the catalyst and the array of competing elementary surface steps that occur. Both the activity and the selectivity are functions of the chemical makeup of a particular catalytic site. They can easily change as the surface becomes covered with reaction intermediates or as an adlayer of unreactive surface species (spectator species) forms. Surface reconstruction can also be predominant and lead to altered surface sites and phases.

In general, the overall catalytic reaction cycle consists of at least four basic elementary reaction steps: molecular adsorption, dissociation, recombination, and molecular desorption. The slow reaction steps are typically dissociation and/or molecular desorption. Both act to control the activity of the catalyst. Selectivity, however, is really a function of several factors. When a molecule has several reaction channels—take CO, for example, which can either dissociate or react with other surface adspecies—a competition exists between the rate of dissociation and the rate of recombination with coadsorbates. This competition ultimately determines selectivity. In addition, surface composition can significantly alter selectivity by changing the relative probabilities for collision of different species. Therefore, the outcome of bimolecular elementary steps, such as surface recombination, is a strong function of the operative surface compositions. Elucidating each of the elements comprising the reaction mechanism is, therefore, of great importance toward predicting the selectivity of the overall reaction.

Quantum-chemical methods which range from semiempirical to first-principles techniques are, therefore, reliable tools which can be used to probe ideas and predict properties, that is, structure and energetics. Semiempirical and empirical quantum-chemical approaches, such as the extended-Hückel method and classical bond order conservation methods, have made important contributions toward mechanistic understandings of various catalytic chemistries through reaction mode analysis of the surface chemistry in terms of detailed orbital interactions. This subsequently enables the deductive comparison of relative interaction energies. More recently, first-

principle quantum-chemical calculations which employ the cluster approximation have become applicable to chemically more realistic model systems. They have been successful in the prediction of adsorption geometries and energetics of ground state species, surface intermediates, and even in finding (estimating) transition states. The latter is necessary to compute reaction rate constants.

The application of quantum-chemical techniques not only provides the basis for understanding the structural and electronic features which govern kinetics, but also enables us to readily probe the effects of altering the surface transition metal, manipulating the nature of the active site or changing the active particle size ensemble. This is a first step toward the long-term goal of catalyst design. In this work, we analyze the effects of changes in transition metal and particle size on the kinetics of various elementary steps.

We focus on the concepts which appear to control different surface reactions and present theoretical results which help to support these ideas. A more extensive technical review which covers the mathematical treatment of the quantum-chemical methods, the formulation of the governing electronic–energetic interactions, and the application to various catalyzed chemistries can be found in Ref. 2.

The electronic structure and fundamental nature of the surface chemical bond has been extensively reported on and is the subject of a series of excellent surface science [3] and theoretical reviews [4]. Initial theoretical treatments were targeted at the solid-state aspects of the metal surface [5]. The formal chemisorption theory which evolved has proven to be a valuable tool. It has been used to describe the surface chemical bond in terms of changes in the local electronic density of states at the surface and has helped aid the interpretation of spectroscopic data of adsorbates on surfaces. *Formal chemisorption theory*, used throughout this review, refers to the analytic solution of applied Green's functions to the surface adsorption problem. The idea of a surface molecule and the qualitative differences between *strong* and *weak* chemisorptive bonds were formulated for the first time within the context of this formal chemisorption theory (see also Ref. 2 for an extensive review of the theory and results).

We begin our discussion with the quantum-chemist's view of chemisorption. This is chemically much more transparent. We comment on the results from formal chemisorption theory throughout the text to help offer conceptual insight. Chemisorption is dictated by the adsorbate–surface interaction. The strength of the adsorbate–surface chemical bond governs the stability of the reactive surface intermediates and, in many respects, controls their fate (whether they desorb, diffuse, or react). Analyzing the distribution of electrons over bonding and antibonding adsorbate–surface fragment orbitals provides direct insight into the adsorbate–surface bond strength as well as adsorbate reactivity. Chemisorption of molecules on transition metals is considered intermediate between the so-called *weak*

adsorption limit and the surface molecule *strong adsorption* limit. In the weak adsorption limit, metal–metal bonding is significantly greater than adsorbate–metal bonding. Adsorbate–surface interactions are, therefore, more appropriately analyzed through perturbation theory. In the strong adsorption limit, the metal–adsorbate surface bonds are substantially stronger, and to a first approximation, result in a strong surface complex such as that present in chemisorption.

The first section of this review is introductory in nature, whereby many of the basic concepts and underlying theoretical constructs are highlighted. A more extensive treatment which contains the detailed derivations can be found in Ref. 2. Much of the analyses which follow rely on concepts from frontier molecular orbital theory [6], whereby the highest occupied (HOMO) and lowest unoccupied (LUMO) molecular orbitals play a dominant role in understanding and predicting the attractive and repulsive features of the interaction between adsorbate and surface. Chemisorption of CO is used as an illustrative example for the application of the HOMO–LUMO concept to surface–chemical bonding. While the concept of electron donation and backdonation provides a satisfying description of the attractive part of the interaction potential, there is no estimation of the repulsion part of the potential. Little information about the coordination of molecules to surfaces can be gained without an accurate understanding of the repulsion effects. By a proper treatment of both bonding and antibonding interactions of the surface–adsorbate fragment orbitals, however, a more complete identification and quantification of Pauli repulsion terms can be provided [7].

Chemical bonding in transition metal systems derives from the interaction of valence d-electron atomic orbitals and the s- and p-valence electrons. The s- and p-atomic orbitals are spatially extended and form a broad valence electron band with an approximate electron occupation of one electron per atom. The occupied metal s-p orbitals are predominantly bonding in nature. The d-atomic orbitals, however, have a much smaller spatial extension and form a much narrower valence electron band with a varying number of electrons per metal atom. Bonding, as well as antibonding, involves the occupation of the metal d-valence electron orbitals. The adsorbate interaction at the metal surface with these valence electron bands is qualitatively very different. The adsorbate–surface interaction is often dominated by the adsorbates interaction with the surface s,p-valence electron band of the surface. Differences in reactivity on different transition metal surfaces, however, are primarily controlled by the interaction with the d-valence electrons.

Chemical bonding features are analyzed here to help determine the relative stability of admolecules or adatoms on geometrically different surface sites. The interaction energies of admolecules typically show only small variations with respect to changes in adsorption sites or geometries. Adatoms, on the other hand, are much more sensitive to variation in

adsorption sites, whereby energies can change considerable from low to high coordination sites.

Much of the quantum-chemical-derived results published in the literature rely on the cluster approximation. The limitations of this approach are discussed in the following sections on methods. The results imply that both nearest as well as next-nearest neighbors with respect to adsorption site are required for reasonable electronic models of the surface.

B. Methods

The quantitative accuracy of a given quantum-chemical calculation toward the prediction of adsorbate–surface binding or surface reactivity is highly dependent upon the method used as well as the choice of the cluster (both size and configuration) chosen to model the surface. Our aim is to overview important quantum-chemical principles controlling adsorption and reaction on catalytic transition metal surfaces or particles. While some of the concepts can be illustrated through qualitative predictions, many others require more accurate calculations. In this section, we briefly highlight various available quantum-chemical methods and discuss their relevance toward understanding and predicting surface chemistry on different transition metal surfaces. The ensuing Methods section is simply an over view of relevant quantum-chemical approaches applied to heterogeneous catalytic systems. More in-depth reviews exist elsewhere in the literature for any given approach. Ruette, for example, has compiled an excellent overview and book on quantum chemistry applied to heterogeneous catalytic systems [28b].

The hierarchical breakdown of the methods employed to study various aspects of chemisorption and catalysis on transition metal surfaces is divided into four major areas: formal theory (analytic solutions), empirical, semi-empirical, *ab initio* molecular orbital theory, and density functional theory. The latter three methods can be further subdivided in terms of the type of calculations, cluster versus slab. A summary of the sampling of the current literature is provided in Table 1 (Sec. I.C).

1. Formal Chemisorption Theory

The formal theory of chemisorption, as discussed earlier, often involves analytical solutions of surface–adsorbate interactions within theoretical approximations that provide parameter-dependent models for chemisorption. Two approaches are distinguished. The first is an extension of molecular orbital theory to the surface chemisorption problem. This approach treats the covalent bonding aspects of the surface–chemical bond. Electron–electron interactions are only implicitly considered through one- and two-center electron repulsion integrals [5, 6a]. Solutions of the chemisorption are sought for the semi-infinite surface problem as a function of valence electron band

occupation, delocalization of surface electrons and overlap between surface and adsorbate orbitals. Two of the most important concepts brought forth by these studies were: (1) the surface complex strongly depends on the ratio of the adsorbate–surface interaction and the bandwidth of the surface valence electron band, and (2) the surface magnetism relates to the ratio of the effective one-electron repulsion integrals and adatom electron residence times [5]. A dependence on the local density of states at the Fermi level can only be expected in the weak adsorption limit and is rarely obeyed by chemisorbing species. The concepts of Tamm and Shockley surface states have also been defined within this theoretical framework (Ref. 2 and references therein).

The second approach starts with the free-electron model of a metal. In the jellium model, electrons are treated as free electrons where discrete attraction potentials due to positive nuclei are replaced by a continuous positive background. The density is chosen such that the electron–nuclear attraction is equal but opposite in sign to the electron–electron repulsion. Perturbation theory is used in different examples to explicitly account for the discreteness of the metal and adsorbate atoms. This treatment is well adapted to examine the consequences of electron–electron interactions [5].

The presence of a surface dipole layer has been explained within the surface-jellium model as due to the spillover of electrons due to their finite kinetic energy. Smoluchowski [8] used this idea to explain the decrease in the work function on more corrugated surfaces where electrons can spill over into the spaces between the atoms. The surface-jellium model has also been used to describe the screening of charge on the surface atoms by the development of an induced image charge. This primarily arises as a consequence of the solution of the Poisson equation and has been extensively analyzed within the jellium model framework.

Effective medium theory, a popular semiempirical method, proposed by Norskov [4a, 31a, 31b], was born out of the jellium model which approximately describes both s- and p-valence metal electrons. The effective medium theory, in essence, is a combination of the tight-binding molecular orbital approach, sketched above, and the jellium model description of the metal s,p-valence electrons.

A more elaborate discussion on formal chemisorption theory and its utility in heterogeneous catalysis is provided in Ref. 2.

A method which is intermediate between effective medium theory and rigorous density functional theory (to be discussed later) is the scattered Xα theory which originated with Slater [9–11]. This method approximates the solid by spheres of constant potential [12]. The metal solid or molecule is then described by equations of motion of a free electron, scattered by the spheres and their corresponding potentials that represent the atoms. Sphere radii and potentials are adjustable parameters. While the agreement between predicted and measurable electronic structures is sometimes quite

good, the method is not accurate enough to predict bond or adsorption energies [9–14].

2. *Empirical Methods*

A recently developed empirical treatment of surface adsorption and reaction energetics is the bond order conservation–Morse potential (BOC–MP) method which was pioneered by Shustorovich [15]. Features of the adsorption complex which require the explicit solution of the equation of motion for the valence electrons within the formal chemisorption theory framework are provided much more simply in the BOC–MP method through a series of analytical expressions. Adsorption energies, interaction energies, and estimated activation barriers are readily predicted. Its special value lies in the important chemical insights it provides. This is effectively demonstrated for various different examples throughout the remainder of this review. Shustorovich [15], Bell [16], Benziger [17], Sellers [18], and Baetzhold [19] have been instrumental in extending the method to treat real catalytic systems. Shustorovich recently assembled an interesting text comprised of a series of review chapters on the application of BOC–MP to heterogeneous catalysis [20]. Due the simplicity and elegance of the BOC approach, we use some of its basic ideas herein to express various concepts. We, therefore, present a short synopsis of the BOC theory.

According to covalent bonding theory the bond order of a chemical bond is defined as:

$$x = e^{-\frac{r-r_0}{a}} \tag{1}$$

where r_0 is the equilibrium bond distance, and a is a bond constant. When the two-center interaction is described by a Morse potential, a simple relation follows between potential, $Q(r)$, and bond order

$$Q(r) = -Q_0(2x - x^2) \tag{2}$$

Q_0 is the bond energy at equilibrium.

For nondirected bonding, the assumption of bond order conservation enables the derivation of analytical expressions that relate the bond strength of an atom–atom bond to the number and the strength of the nearest-neighbor interactions. The assumption of bond order conservation implies the following:

1. If atom A has n neighbors rather than one, the bond strength $Q(n)$ can be written as a sum of two-body interactions:

$$Q(n) = -\sum_{i=1}^{n} Q_i \tag{3a}$$

2. The total bond order is conserved:

$$x_n = \sum_{i=1}^{n} x_i = 1 \tag{3b}$$

If the bonds are equivalent, then x_i can be written as:

$$x_i = \frac{1}{n} = e^{-\frac{r-r_0'}{a}} \tag{4}$$

It then follows that the equilibrium bond length has to increase as the number of neighbors n increases. Substitution of (4) into (2) gives:

$$Q(n) = -Q_0\left(2 - \frac{1}{n}\right) \tag{5}$$

The total interaction increases much less rapidly with the number of metal atom neighbors, then predicted assuming each bond to be independent. The principle of bond order conservation assigns a particular bonding valence to each atom. This valence is assumed to be constant and distributed over the bonds that are directed to that atom. The more bonds there are, the more the bonding valence is distributed over them and the weaker each bond becomes. The principle of bond order conservation is an approximate concept based on the assumption of nondirected bonding. As we will see, its consequences are useful in the analysis of first-principle calculation results. When expressions for interaction energies are properly parametrized, the result is a formalism that enables predictions of adsorption energies and reaction energy changes. Shustorovich and Bell [21, 22, 23] have explored this extensively for several reactions, such as methanol synthesis [15c], CO hydrogenation [21], and formic acid decomposition [16]. The bond order conservation expression for the heat of adsorption of molecule AB to the metal surface [2] is obtained by additional algebra. Assuming perpendicular adsorption through atom A, the energy of adsorption works out to be:

$$\Delta E_{AB}(n) = -\frac{\left\{Q_A - D_{mm}\left(1 - \frac{1}{n'}\right)\right\}^2}{\frac{Q_A}{n} + D_{AB} + \frac{D_{mm}}{n'}} \tag{6}$$

where Q_A is the bond strength between a metal atom and A; D_{AB} is the dissociation energy of molecule AB; and D_{mm} the bond strength between two metal atoms. The variables n and n' are the coordination number of atom A with the surface and the number of nearest-neighbor metal atoms associated with the surface adsorption site, respectively.

The corresponding expression for the heat of adsorption of atom A alone is:

$$\Delta E_A(n) = -\frac{\left\{Q_A - D_{mm}\left(1 - \frac{1}{n'}\right)\right\}^2}{\frac{Q_A}{n} + \frac{D_{mm}}{n'}} \tag{7}$$

In comparing Eq. (6) with Eq. (7), it becomes evident that $|\Delta E_{AB}(n)| < |\Delta E_A(n)|$. This is well established experimentally and a fundamental characteristic of bond order conservation. The molecule binds more weakly to the metal surface than an atom, due to the fact that in the molecule atom A already has a bond to atom B. The corresponding weakening of the metal–adatom bond is a function of the molecular bond energy D_{AB}.

According to expressions (6) and (7), the heat of adsorption increases with the strength of the atom A–metal atom interaction. This is counteracted by the interaction of the surface atom with its nearest-neighbor metal atoms, in agreement with the quantum-chemical results. According to bond order conservation, molecule AB will always favor the higher-fold coordination sites. This clearly illustrates the limitation of the method. As is discussed in sections II.D.2 and II.B, CO and NH_3 often prefer adsorption to low coordination sites. This is due to directional bonding which now becomes important.

3. *Semiempirical Methods*

The tight-binding method, better known to the chemistry community as the Hückel method, is the most extensively used semiempirical molecular orbital method [24]. This approach, which was originally introduced to treat electronic structure problems in organic chemistry, can also be used to study clusters or slabs [2, 6a]. Nonorthogonality of the atomic orbitals which comprise the basis for the molecular orbitals is essential for treating inorganic systems. Pauli repulsion effects, which are crucial in understanding the electronic adsorbate surface (cluster) binding, require the explicit accounting of this nonorthogonality. The absence of this requirement is a gross limitation of the simple Hückel method. The extended Hückel method (EHT), developed by Hoffmann, specifically treats nonorthogonality of the atomic orbits, and is therefore a far more realistic approach for modeling transition metal systems.

An extension of the EHT approach that empirically accounts for repulsive interactions, was introduced by Anderson and labeled the atomic superposition and delocalization (ASED) molecular orbital method [25, 26]. The repulsive part of the bond is determined through the superposition of fragment electron densities with a correction for the delocalization of electron density. This tends to provide somewhat more reliable adsorption

geometries and energetic trends. ASED is, therefore, used to describe CO and CH_3 adsorption phenomena later in this review.

More advanced semiempirical treatments which explicitly treat electron–electron interaction effects have also been employed in the analysis of the surface reaction chemistry. MNDO [27a], AM1 [27b], PM3 [27c], SAM1 [27d] methods (Hamiltonians and parameter sets) appear to be the most widely used methods for dependable and reasonably accurate treatment of organic systems [27e]. The current absence of parameters for transition metal systems, however, renders most of them inapplicable to the treatment of catalytic surface problems. The development of parameter sets for transition metal systems, however, is a currently ongoing task for a number of research groups and could prove to be quite valuable in modeling catalytic systems. Other semiempirical approaches, such as CNDO and INDO methods, offer little more than just qualitative insight and are hard to justify over the simple EHT approach. Ruette's text nicely summarizes an extensive summary of CNDO, INDO, MNDO semiempirical approaches applied to heterogeneous catalysis [28]. The well-parametrized ZINDO algorithm by Zerner [29] has been the lone exception, and has been used in a number of interesting catalytic studies [30] to provide reasonably accurate structural and spectral data.

Effective medium theory [31], discussed earlier, and the related embedded-atom method [32] are semiempirical techniques which have been developed strictly for the analysis of extended metal systems. The atomic electron density is manipulated to handle the effects of embedding into an extended lattice. A distinction is made between contributions to bonding by highly delocalized s,p-valence electrons, and the more localized and lower density d-valence electrons. We describe the two methods further and compare their utility in Ref. 2.

4. *First-Principle Methods*

The difficulty in properly treating electron–electron interactions and electron correlation is an inherent limitation of nearly all of the proposed methods described above. This problem is further complicated when one attempts to treat transition metal systems which contain significant numbers of d-electrons and degenerate eigenstates. Incomplete descriptions of electron correlation effects lead to gross errors in bonding energetics. Accurate assessments of the energies therefore require implicit or explicit accounting of electron correlation. While density functional methods (discussed later) treat correlation explicitly, *ab initio* approaches typically require extensive configuration interaction (CI) treatments.

Historically, *ab initio* approaches were severely limited due to the very small system sizes which could be examined. Current computational quantum-chemistry, however, has reached a level of sophistication where much larger and more scientifically meaningful calculations are now routinely

possible. Quantitatively reliable predictions of geometric structure, interaction energies, and electronic properties can be made for organics, metals, and even transition metal systems (see Refs. 33–37). At the highest levels of calculation, differences between theoretically computed and experimental values reflect limitations in the model choice rather than intrinsic limitations of the calculation method used to solve for the electronic structure. Both *ab initio* molecular orbital methods and density functional methods, which are derived from first principles, have proven successful in predicting the electronic and energetic properties of transition metal containing systems.

a. Ab initio *Molecular Orbital Methods.* The most basic *ab initio* molecular orbital approach is the Hartree–Fock self-consistent field approach (HF–SCF). Simple Hartree–Fock which scales as N^4 (where N is the number of basis functions) is known to yield poor geometries and energetics for transition metal containing systems due to the absence of electron correlation treatments. Electron correlation approaches are essential in treating the near-degeneracy effects and the multireference wave character which accompany transition metal systems. This is particularly important in correctly treating the chemical bond formation and breaking processes involved in chemical reactions.

Electron correlation can be incorporated by expanding the many-electron state function into a linear combination of Slater determinants. In this approach, the Slater determinant many-electron representations are built from the Hartree–Fock one-electron functions. In this way a more complete representation of the active configurational space is formed. For larger systems, such a full CI expansion is computationally inconceivable at this point in time. Instead the configurational state functions are expanded to include single, double, and triple excitations, CCSID(T) before being truncated. Size consistent treatments include either the coupled pair functional (CPF) method by Ahlrichs et al. [38] or the modified coupled pair functional (MCP) method by Chong and Langhoff [39]. Other approaches also aimed at capturing correlation effects include many body perturbations techniques and coupled cluster approaches [40].

Alternatively, one can use methods that vary the initial one-electron functions and expand the many-electron wave function in a linear combination of Slater determinants to incorporate a more complete representation of the active configurational space. These approaches are concurrent with the SCF and provide a more accurate reference wave function. The complete active space SCF (CASSCF) MCSCF (multireference configurational SCF) method is the most well known approach.

While the most accurate MO solution techniques to transition metal systems involve coupled static/dynamic CI approaches, the computational burden which scales as N^n ($n > 7$) is clearly a severe limitation. Balasubramanian [41] and Langhoff and Bauschlicher [33] have been quite active

and have authored a series of excellent papers in this area. Due to the computational expenditures, the results have been limited to systems with fewer than five metal atoms. The MCSCF and MCPF (multiple coupled pair functional) approaches are computationally more realistic methods for analyzing larger transition metal clusters.

The level of CI corrections as well as the basis set choice strongly dictate both the computational efforts and the reliability of the results. Various methods have been proposed in the literature to reduce the computational expenditures involved in treating larger transition metal systems. Pseudopotentials (14, 15), for example, were introduced to describe the potentials far from the chemisorption center. This involves freezing the d-electrons in their valence state [14]. In a second related approach [15], electrons are redistributed into the set of cluster orbitals to save in terms of computational effort. Most of the methods involved in reducing CPU requirements are based on assumptions and/or approximations which are highly specific to the systems studies. This, in general, limits their applicability.

b. Density Functional Methods. An alternative first-principle approach is that of density functional theory (DFT). Parr and Yang provide an elegant overview on the historical developments of DFT. They provide an extensive mathematical treatment of the theory and demonstrate its application to chemical systems [42]. While the roots of DFT date back to Thomas and Fermi [43, 42] in 1926, the formal development of density functional theory as a rigorous first-principles treatment is attributed to Hohenberg and Kohn [44, 42], who demonstrated that the energy is a unique functional of the density. The electron density is computed by solving the set of Kohn–Sham equations in a self-consistent manner [45, 42]. The inherent advantage of DFT approach is that the total electronic energy is directly tied to electron density. Electron interactions and configurational interactions are treated explicitly as a functional of the density. This reduces the computational burden of treating intensive and cumbersome electron–electron interaction terms. DFT methods, therefore, scale by N^3 rather than the N^5 (or higher) required for *ab initio* CI calculations. The accuracy of DFT methods is comparable with that of the more rigorous *ab initio* CI methods.

Ziegler has written an excellent review on the DFT theory, relevant solution methods, and its current accuracy for predicting properties of organic and organometallic systems [46]. DFT calculations which include nonlocal gradient corrections for correlation and exchange typically yield bond lengths to within 0.01–0.05 Å, bond angles within 1–2°, bond energies to within 20 kJ/mol, and infrared and UV shifts to within 5% of the experimental values for both organic and transition metal containing organometallic systems. Transition metal systems are typically predicted with somewhat less accuracy than the all-organic systems. Additional properties

such as the dipole and quadrapole moments, excitation energies, NMR shifts, and photoelectric spectra are also possible, but the accuracy of DFT is still relatively untested.

Labanowski and Andzelm [47] compiled a comprehensive series of papers from a DFT workshop in 1991 which further discuss theoretical as well as algorithmic developments. In addition, there is a substantial collection of "application" contributions which help demonstrate the accuracy for organic, organometallic and catalytic systems.

Most of the efforts to date aimed at computing heterogeneous catalytic systems have employed molecular cluster models of the local surface adsorption or reaction site. DFT can also be used to treat bulk solids, extended surfaces, and slabs. Algorithm specifics include the choice of exchange-correlation functional, nonlocal gradient corrections (Becke, Perdew, Lee–Yang–Parr, Perdew–Stoll), basis set functions (Gaussian, Slater, plane-wave), degree of grid accuracy, gradient and second-derivative solutions (analytic vs. numeric) used as well as a number of other features. Basis sets have been rigorously optimized and can in many situations provide better solutions than their *ab initio* counterparts due to a better representation of the unfilled valence orbitals. Most of the calculations described herein use double or triple zeta basis sets with polarization. Currently available programs include the Amsterdam density functional (ADF) program by Baerends and colleagues [48a], DGauss from Cray Research Inc. [48b], DMol from Biosym [48c], deMon from Salahub [48d], and G92/DFT from Gaussian [48e]. It has become clear that for the chemisorption problem, reasonably accurate computational results can be obtained provided that both nonlocal corrections to the exchange-correlation potential and adsorbate–surface geometry optimization are included. The degree of accuracy is on the order of stringent *ab initio* CI approaches discussed above. While a concise and systematic study of different adsorbates on transition metal clusters and surfaces has yet to be established, a summary of the recent literature indicates that the accuracy is on the order of that discussed by Ziegler for transition metal–ligand systems [34]. All DFT results discussed in this paper are based on these common foundations.

5. *Cluster Models*

Due to limited computational resources, many of first principle based treatments of the reactive surface involve the application of finite cluster models. While the local coordination about the active surface site in a model cluster may correctly mimic the real surface, the chemical bonding and the electronic structure may still be quite different. In small clusters, the changes in cluster size may have significant effects on the interaction energy. Such differences are well known experimentally [49]. While there are no definitive analyses between cluster sizes and adsorption properties, there have been a number of theoretical studies aimed at understanding these issues

[50]. The reliability of DFT results makes them well suited as quantitative probes for the changes in adsorption with changes in cluster size. Adsorption properties vary strongly with cluster size for clusters with only a few atoms. For larger clusters, convergence of adsorption properties have been found to strongly depend on the shape of the clusters [50a, 50b]. Cluster convergence is facilitated when comparisons are made between clusters which have been completely geometry optimized.

One very effective proposal introduced by Whitten [51] involves a rigorous optimization the local interactions between adsorbate and a small cluster of surface/bulk atoms. The resulting system is then embedded into larger clusters to treat the interactions due to the bulk. A second proposal treats the full electronic structure of the local adsorption complex but adapts frozen core d-valence electron or pseudopotential methodology [52] to model the remaining cluster atoms. This enables the calculation of much larger cluster sizes. A third proposal involves the redistribution of electrons in the cluster, so as to electronically populate the strongly interacting orbitals [52] that are empty in the small cluster but become occupied on the surface due to the additional interactions with neighboring atoms. While these approaches are successful in modeling particular systems, they tend to introduce some sense of arbitrariness into the calculation which makes them difficult to adapt in a more general sense. Pseudopotential methods, for example, have occasionally led to significant errors [53].

Siegbahn was one of the first to recognize that changes in the local surface orbitals available for binding change as a function of cluster size. In an effort to counter the spurious changes in energy which follow this effect, he proposed the "bond preparation" scheme [50a, 50b]. The highest occupied surface molecular orbital is either partially filled and available to easily accept an adsorbate electron or completely filled whereby an electron must first be promoted to the lowest unoccupied orbital before adsorption. The energy cost associated with accepting electrons into the actual bulk situation would be very small and negligible due to the continuous nature of the band. In these finite clusters, however, the HOMO–LUMO gap can be quite high. The cost for promoting an electron for binding would therefore be substantial. To reduce this anomalous energy cost, the "bond preparation" scheme manipulates the electronic state of the bare cluster so as to mimic the electronic state of the bulk, therefore making the cluster more favorable for adsorbate binding. Mijoule et al. [50e–50g] proposed a different approach to reduce the adsorption energy fluctuations on small clusters. In this method, the binding energy is decomposed into three steps. Binding energy fluctuations are removed by substituting in the actual work function of the metal for the discrete ionization potential of the cluster. Various charged clusters are computed to find the charge, $x+$, which remains nearly constant over different cluster sizes.

Interestingly, these adsorption energy fluctuations with cluster size are

much more predominant for MO–HF-based methods. Carefully optimized cluster geometries which include adsorbate–cluster interactions substantially reduce the magnitude of the adsorption energy oscillations [50i, 50j, 54]. Salahub has suggested that the more precise prediction from DFT calculations is attributed to DFT's ability to more accurately represent the energy levels of the virtual (unoccupied) orbitals [50k]. We find for various different adsorbates on a series of different-sized palladium clusters that the adsorption energy fluctuations are on the order of 20 kJ/mol and tend to oscillate about the measured experimental value [54]. There are continuing efforts aimed at understanding cluster dependence. We discuss more of our own results in modeling adsorption of NH_3 on Cu_y clusters in Sec. II.B, CO on Co in Sec. II.E, and potassium on Rh clusters in Sec. II.F.

6. *Slab Methods*

Both *ab initio* and DFT methods now offer extended two- and three-dimensional slab/surface algorithms which treat the infinite solid. The CRYSTAL program by Pisani and Roetti [55] is a Hartree–Fock *ab initio* method which computes extended unit cell systems. The solution method is based on an HF–SCF algorithm, where a set of Fock matrices are built in direct space and subsequently used to generate reciprocal space Fock matrices which can then be diagonalized and solved to obtain a set of crystal orbitals and energies. This yields a new set of direct space Fock matrices. The process is iterated until a self-consistent field is obtained. The unit cell can be repeated in one, two, or three dimensions which allows the solution for chains, surfaces, and extended crystal materials. The approach has been applied to a number of different metal oxides systems [56] as a means to explicitly evaluate the Madelung potential and various structural aspects which would be difficult to analyze with cluster calculations, such as the interactions of zeolite pore walls.

Analogously, a number of different extended system DFT algorithms have also been developed. Teter developed a LAPW-based algorithm termed CORNING to study the electronic structure of different silicon oxides [57]. te Velde and Baerends extended their molecular code efforts and established a precision-based DFT method which utilizes the LCAO formalism [58]. Feibelman [59a, 59b] Boettger [59c], Norskov et al. [59d], Chelikowsky et al. [59e, 59f], and Kasowski et al. [59h] have developed similar LDF algorithms to treat extended two- and three-dimensional systems. A number of the necessary features essential for quantitatively accurate predictions, however, have yet to be implemented. Geometry optimization and *in situ* SCF nonlocal gradient corrections are just a few of these items. The Car–Parinello DFT dynamic algorithm also appears to be very promising avenue for exploring molecular surface dynamics.

Most of the results discussed herein are derived from the formal theory,

extended Hückel (ASED) and first-principle DFT approaches. Formal theory serves to emphasize the concepts governing chemisorption on catalytic surfaces, while EHT results are used to further expand these constructs. DFT results are used to provide quantitative estimates for adsorption as well as surface reaction energetics. The primary role of the three is to establish a set of governing concepts on the nature of adsorbate–surface bonding and its relationship to surface chemistry.

C. *Applied Theory in Catalysis: Literature Review*

An all-encompassing review of the literature of theoretical treatments of transition metal systems is a difficult task due to the tremendous number of papers written on the subject. Instead we attempt to provide a concise synopsis of the various types of calculations which have been performed and an overview of some of the systems which have been studied. We summarize this in terms of the general method employed and method specifics, that is, transition metal atoms clusters or surfaces, adsorbate binding, adsorption site specifics, and reactions examined. Table 1 details a list of the specific papers categorized by: (1) methods employed which range from empirical BOC to first-principle (*ab initio* and DFT) cluster to slab calculations, and (2) authors' citation. The specifics for each citation are broken down into the following: transition metal cluster, adsorbates, CI, adsorption sites, cluster geometry optimization, adsorbate geometry optimization, electronic analysis, magnetic properties, binding/adsorption energies, energy decomposition, and frequencies. Many of these are self-explanatory.

Transition metal clusters refer to the type of transition metal framework used in the calculation, that is, single metal atom center, cluster, or surface. Various papers on organometallic complex calculation which provide invaluable insights on the molecular control of the chemistry are cited here as well. Clusters are denoted by their ordered layers. For example, "(4, 1)" refers to four atoms in the surface layer and one atom in the second layer. The adsorbates studied are listed next. This is followed by information on method specifics, that is, the type of CI used in the *ab initio* MO methods or the nonlocal gradient corrections employed in the DFT calculation. The next three columns tabulate the adsorption sites considered, whether or not the cluster geometry was optimized, and whether or not the adsorbate was optimized. *Electronic orbital analysis* indicates the analysis used to describe the governing electronic features of the results. Many of the papers listed analyze specific orbital interactions, charge-transfer mechanisms, orbital population analysis, relative density of states, etc., and are identified as such. The treatment of accurate spin states and cluster magnetic moments can be very important for the quantitative prediction of binding energies and adsorption site specifics. We point out which of these studies explicitly account for these effects. The *binding energy/adsorption energy* column

TABLE 1

Method	Ref., author(s)[a]	Transition metal clusters	Adsorbates	CI	Adsorption sites
BOC-MP	[T1] Bell	Cu, Pd	Formic acid	—	—
		Cu, Pt, Ni, Fe/W	CH_x and CO species	—	—
		Fe/W, Ni, Pt	CH_x species	—	—
				—	—
	[T2] Benziger	Ni, Cu, Mo, Ru, Rh, Pd, Ag, W, Ir, Pt, Au	Various small molecules	—	—
	[T3] Paredes et al.	Pd, Pt, Ag, Au	H_2, O_2, OH, OOH, H_2O	—	—
	[T4] Patrito et al.	Pt, Pd, Rh, Ni	OH	—	—
	[T5] Sellers	Au	CH_3SH, SH, H	—	—
	[T6] Sellers	Au	CH_3SH and SH	—	Favorable paths
		Ni	H_2		
	[T7] Shustorovich and Bell	Pd, CU	CO, CO_2, HCO, H_2CO, H_3CO, MeOH, HCOO, H_2O, H_2, H	—	—
	[T8] Shustorovich and Bell	Ni, Pd, Pt	C, O, H, CO, HCO, CH_x	—	—
	[T9] Shustorovich and Bell	Ag, Cu, Ni, W	O, N, H, OH, NH, H_2O, NH_2, NH_3 CH_3O, MeOH, $HCOO_x$, CH_x	—	—
	[T10] Shustorovich	Fe, Ni, Cu, W, Rh, Pt, Re, Ag, Pd	H, N, C, O, NO, CH_x, CH_xO, CH_3OH	—	—
EHT	[T11] Sautet and Paul	Pd, Pt	Ethylene, butadiene	—	π vs. di-σ
	[T12] Minot et al.	Pt(7,3), Pt(10,5) Pt(12,7) Slab calc.	CH_x fragments	—	1-, 2-, 3-fold
	[T13] Zheng et al.	Ti(0001), Cr(100), Co(0001) Slab calcs.	CH_3, CH_2, CH	—	Site preference
	[T14] Saillard and Hoffmann	Ni and Ti ML_x complexes (111) surfaces	H_2 and CH_4	—	1-, 2-, 3-fold

Summary of Empirical, Semiempirical, *Ab Initio*, and Density Functional Quantum-Chemical Analyses Applied to Chemisorption on Transition Metal Clusters: Calculations, Clusters, and Analysis

Geometry optimization		Electronic orbital analysis	Magnetic properties	Binding/ adsorption energy	Energy decomposition	Frequencies
Cluster	Adsorbate					
—	—	—	—	Empirical	—	—
—	—	—	—	Empirical	—	—
—	—	—	—	Empirical	—	—
—	—	—	—	Empirical	—	—
—	—	—	—	Empirical	—	—
—	—	—	—	Empirical	—	—
—	—	—	—	Empirical	—	—
—	—	—	—	Empirical	—	—
—	—	—	—	Empirical	—	—
—	—	—	—	Empirical	—	—
—	—	—	—	Empirical	—	—
—	—	—	—	Empirical	—	—
—	—	Charge transfer	—	Estimates	—	—
No	No	Electron charge transfer	—	Estimates	—	—
No	Yes	Charge transfer, DOS analysis, Orbital analysis	—	Estimates	—	—
No	Yes	Charge transfer, DOS, orbital	—	Estimates	—	—

(*continued*)

TABLE 1.

Method	Ref., author(s)[a]	Transition metal clusters	Adsorbates	CI	Adsorption sites
	[T15] Sung and Hoffmann	Ni(100), Ni(111), Co(0001), Fe(110), Cr(110)	CO	—	1-, 2-, and 3-fold
	[T16] Sung et al.	Ni(111) slabs	NO	—	1-, 2-, 3-
	[T17] Anderson and Choe	Pt_{15}	Ethylidine, ethylene	—	1-, 2-, 3-, di-σ
	[T18] Simon and Bigot	Ni(111), 605 atoms	K	—	3-fold
DIM	[T19] Richtsmeier et al.	Cu_3, Ag_3, and Au_3	—	—	—
	[T20] Richtsmeier et al.	Cu_n, Ag_n, and Au_n (n = 4–6)	—	—	—
	[T21] Richtsmeier et al.	Li_3, Na_3, K_3, Rb_3, Cs_3, Cu_3, Ag_3, Au_3	—	—	—
ZINDO	[T22] Estiu and Zerner	Rh_{13} and Rh_{19} clusters	—	—	—
	[T23] Estiu and Zerner	Rh_2–Rh_{14}	—	—	—
	[T24] Estiu and Zerner	Ni_2, Ni_4, Ni_{13}	—	INDO/S, CAHF CI	—
GVB	[T25] Upton and Goddard	Ni_{20} and Ni_{28}: (100), (111), (110)	H, Cl, Na, O, S	MCSCF	10 unique sites
	[T26] Upton et al.	Ag_{24}(110)	O_2	Double and single	Long bridge site
	[T27] Low and Goddard	Pd atom	H, CH_3, H_2, C_2H_6	MCSCF	—
	[T28] Zakharov et al.	Ni(7,3)	H_2O	HF–SCF	1-fold
	[T29] Ohanessian and Goddard	Sc^+–Cu^+ Y^+–Ag^+ La^+ Hf^+–Au^+	H, H^+	—	—
	[T30] Anslyn and Goddard	Mo $MoCl_3$ $MoCl_4$	Alkylidene, ethylene	GVB with perfect pairing wave function	—

Continued

Geometry optimization		Electronic orbital analysis	Magnetic properties	Binding/ adsorption energy	Energy decomposition	Frequencies
Cluster	Adsorbate					
No	Yes	Charge transfer, DOS, orbitals, electron density	—	Estimates	—	—
No	Yes	Charge transfer, DOS, orbital	—	Estimates	—	—
No	Yes	Orbital	—	Estimates	—	—
No	No	LDOS occupation	—	—	—	—
Yes	—	—	—	Binding energy Cohesive energy Dissoc. energy	—	Yes
Yes	—	—	—	Binding energy Cohesive energy Dissoc. energy	—	Yes
Yes	—	—	Spin	Binding energy Cohesive energy Dissoc. energy	Yes	—
Yes	—	Orbitals (some)	High spin state anal.	—	—	—
Yes	—	Orbitals (some)	High spin state anal.	—	—	—
Yes	—	Orbitals, population, valence E	Magnetism	—	—	—
No	Yes	Orbital	High spin state anal.	Yes	—	Yes
No	Yes	Orbital charge	High spin and excited states	Yes	—	Yes
—	Yes	Orbital	Yes	Yes	—	—
—	Yes	—	—	Yes	—	—
Yes	Yes	Charge transfer, orbitals, exchange energy	Spin states	Yes	Bond energies, exchange energies, dissociation energies	—
Yes	Yes	Orbitals, overlap, population	—	—	—	—

(*continued*)

TABLE 1.

Method	Ref., author(s)[a]	Transition metal clusters	Adsorbates	CI	Adsorption sites
	[T31] Carter and Goddard	Ag clusters	O, O_2, OH, C_2H_x, C_3H_x OCH_2CH_2, OCH_2CHCH_3, $OCHCH_2$, $OCHCHCH_3$ OCH_2CHCH_2, C_2H_4O cycle, C_3H_6O cycle, OCH_2CH	GVB–PP GVB–CCCI	—
	[T32] Carter and Goddard	Ag_3X	X = O, O_2, Cl, OH, $C_2H_4^+$	GVB–PP–CCCI	1-, 2-, 3-fold
	[T33] Carter and Goddard	VO^+ and RuO^+, ScO^+ vs. NiO^+	—	GVBCI GVB–PP GVB–RCI	—
	[T34] McAdon and Goddard	Lin and Lin^+ (n = 3–13 clusters)	—	GVB–PP GVB–CCI	—
	[T35] McAdon and Goddard	Cu, Ag, Au, Li, and Na	—	GVB–PP GVB–CI	—
HF-SCF	[T36] Blomberg and Siegbahn	Ni atom	H and H_2	CASSCF CCI	—
	[T37] Siegbahn et al.	Ni_{13}, Ni_{14}, Ni_{34}, [100]	H_2 and H	MCSCF SDCI	Atop bridge diss.
	[T38] Jensen and Siegbahn	Zr^+, Ti^+, Be^+, Mg^+, Al^+, Si^+	CH_3, ethylene	MCPF	—
	[T39] Mitchell et al.	Ni atom	H, OH, H_2O	MCPF CCSD(T)	—
	[T40] Siegbahn and Wahlgren	Ni_5, Ni_9, Ni_{17}, Ni_{25}, Ni_{33}, Ni_{37}, Ni_{41}	O	MCPF CPP	3-, 4-fold sites
	[T41] Blomberg et al.	Pd_2	CH_4, CH_3, H	MCPF	—
	[T42] Backvall et al.	Pd atom	Cyclopropane	CSSCF CCI	—
	[T43] Panas et al.	Ni(9,4) Ni(6,8,6), Ni(2,9,4)	O, O_2	CASSCF CCI	1-, 2-, 4-fold
	[T44] Blomberg et al.	Pd, Rh, Ni, Fe, Co atoms	C_2H_6, CH_3	CASSCF CCI	—
	[T45] Siegbahn and Panas	Ni_3, Ni(4,1), Ni(12,9,4)	CH_x (x = 1, 3)	CASSCF CCI	3-, 4-fold, (111) (100)
	[T46] Siegbahn et al.	2nd row trans. metal atoms	C_2H_4	MCPF CCSD(T)	—
	[T47] Blomberg et al.	2nd row trans. metal atoms	C_2H_4	MCPF CCSD(T)	—
	[T48] Siegbahn	2nd row trans. metal atoms	C_2H_2	MCPF CCSD(T)	—
	[T49] Siegbahn and Blomberg	2nd row trans. metal atoms	CH_4 and H_2	MCPF QCISD	—

Continued

Geometry optimization		Electronic orbital analysis	Magnetic properties	Binding/ adsorption energy	Energy decomposition	Frequencies
Cluster	Adsorbate					
Yes	Yes	Orbitals	Spin states	Yes	—	—
Yes	Yes	Orbitals	Spin state	Yes	No	Yes
—	Yes	Orbitals, charge transfer, overlap	Detailed spin state anal.	Yes	—	Yes
Yes	—	orbitals	Spin state	Binding energies	—	—
Yes	—	Orbitals	Spin state	Binding, cohesive, and atomiz. energies	Yes	—
—	Yes	Detailed state and PES	—	Yes	Yes	—
—	Yes	Detailed state analysis	—	Yes	Yes	—
—	Yes	Population analysis	Spin states	Yes	—	—
—	Yes	—	Spin state	Yes	—	—
—	—	Orbitals	Spin state	Yes, bond prep.	—	—
Yes	Yes	Population	Spin state	Yes	—	—
—	Yes	Orbital character	—	Yes	—	—
—	Yes	Orbital occupation	—	Yes	—	—
—	Yes	Population	—	Yes	—	—
Ni_5 only	Yes	—	—	Yes, bond prep.	—	Yes
—	Yes	Population	Spin state	Yes	—	—
—	Yes	Population	Spin state	Yes	—	—
—	Yes	Population	Spin state	Yes	—	—
—	Yes	—	Spin state	Yes	—	—

(*continued*)

TABLE 1.

Method	Ref., author(s)[a]	Transition metal clusters	Adsorbates	CI	Adsorption sites
	[T50] Siegbahn	2nd row trans. metal atoms	CH_4, H	MCPF MP2 QSID	—
	[T51] Blomberg et al.	Pd(2+) complexes	Cyclopropane	CASSCF CCI	—
	[T52] Siegbahn et al.	2nd row trans. metal hydrides (MH_x)	CH_4	MCPF	—
	[T53] Siegbahn and Svensson	2nd row trans. metal atom hydrides	CH_x	MCPF QCISD MP2	—
	[T54] Siegbahn et al.	Ni_n (n = 4–40), Ni(100) models, Cu_{n+} clusters	H, O, CH_2	MCPF ECP	4-fold
	[T55] Blomberg et al.	2nd row trans. metal atoms	CO, H, CH_3	MCPF QCISD	—
	[T56] Blomberg et al.	2nd row trans. metal cations	CH_4	MCPF	—
	[T57] Blomberg et al.	Pd and Pd_2	CO	CASSCF MCCI CPF	—
	[T58] Blomberg et al.	Ni and Pd atom	H_2, CH_3, CH_3-CH_3	CASSCF CCI	—
	[T59] Siegbahn and Blomberg	1st row trans. metal atoms	Ethane, cyclopropane, cyclobutane	CASSCF CCSD(T)	—
	[T60] Blomberg et al.	2nd row trans. metal atoms	NH_3	MCPF CCSD(T)	—
	[T61] Blomberg and Siegbahn	Ti, Y, Zr, Nb	N_2	CASSCF MCPF	Parallel Perpendicular to M–M
	[T62] Hermann et al.	Cu_1, Cu_3, Cu_4, Cu_6, Cu_7, Cu_9, Cu_{10}, Cu_{13}, Cu_{15}, Cu_{16}, Cu_{18}, Cu_{19}, Cu_{22}, Cu_{25}, Cu(111) models	OH	HF–SCF CI	Top, bridge, 3-fold FCC, and HCP
	[T63] Bagus and Illas	Ag_4	NO	MCSCF	3-fold site
	[T64] Bagus and Illas	Cu_5	O	HF–SCF	4-fold site
	[T65] Bagus et al.	Cu_4 and Cu_5	NO	MCSCF	4-fold site
	[T66] Bagus and Pacchioni	Cu(16,9) Cu_5 Ag_5	K, NO SCN	SCF Limited MCSCF	4-fold
	[T67] Ricart et al.	Cu(1,4)	CO	HF–SCF CCI	1-fold site

Continued

Geometry optimization		Electronic orbital analysis	Magnetic properties	Binding/ adsorption energy	Energy decomposition	Frequencies
Cluster	Adsorbate					
—	Yes	Population	Spin state	Yes	—	—
Yes	Yes	Population	Spin state	Yes	—	—
Yes	Yes	—	Spin state	Yes	Yes	—
Yes	Yes	—	Spin state	Yes	—	—
—	Yes	Population	—	—	—	—
Yes	Yes	Population	Spin state	Yes	—	—
Yes	Yes	—	Spin state	Yes	—	—
—	Yes	Population	Spin state	Yes	—	—
—	Yes	—	Spin state	Yes	—	—
—	Yes	Population	Spin state	Yes	—	—
—	Yes	Population	Spin state	Yes	—	—
Yes	Yes	Population	Spin states	Yes	—	Yes
—	Yes	Ionization potentials, charge transfer	—	Yes	—	—
—	Yes	Dipole	—	Yes	—	Yes
—	Yes	Dipole populations	—	Interaction energy	CSOV	—
—	Yes	Dipole anal	Spin state	Yes	—	Yes
—	Yes	Dipole population	—	Interaction energy	CSOV	—
—	Yes	—	Spin state	Interaction energy	CSOV	—

(continued)

TABLE 1.

Method	Ref., author(s)[a]	Transition metal clusters	Adsorbates	CI	Adsorption sites
	[T68] Fernández-Garcia et al.	Cu(4,1)	NO	HF–SCF	1-, 2-, and 3-fold site
	[T69] Illas et al.	Cu(4,1), Ag(4,1)	O	SCF CASCI, MP2, CIPSI	4-fold
	[T70] Bagus and Hermann	Cu(1,4)	CO and NH_3	HF–SCF	Atop
	[T71] Ricart et al.	Cu(4,1), Ag(4,1), Cu(16,9), Ag(16,9), Cu(169,16), Ag(16,9,16)	O	HF–SCF	4-fold
	[T72] Bauschlicher	Cu(1,4), Cu(9,4), Cu(9,4,5), Cu(21,12), Cu(21,12,5)	CO	MCPF	Atop
	[T73] Hermann	Li(4,5), Li(5,4), Cu(1,4)	O, CO pt charges	HF–SCF	1,4-fold
	[T74] Hermann and Meyer	Cu_1, Cu_2, Cu_3	OCH_3	HF–SCF	1-, 2-, 3-fold
	[T75] Pacchioni and Lambert	Pd_6, Pd_8, Pd_6, Au_6,	C_2H_2, C_4H_6, C_6H_6, C_8H_8	HF–SCF	Multiple
	[T76] Pacchioni and Koutecky	Pd, Pd_2, Pd_3, Pd_4	CO	HF–SCF MRD–CI	1-, 2-, 3-, 4-fold
	[T77] Pachioni and Koutecky	Pd, Pd_2, Pd_3, Pd_4	H and CO	HF–SCF MRD–CI	1-, 2-, 3-, 4-fold
	[T78] Fischer and Whitten	Cu_9	O_2	HF–SCF CISD	Atop site
	[T79] Chattopadhyay et al.	Ni(13,9,5) embedded, Ni_{62} total	NH_3	HF–SCF CSID	1-, 2-, 3-fold
	[T80] Yang and Whitten	Ni(13,9,5) embedded, Ni_{62} total	CH_2, CH, H	HF–SCF CSID	1-, 2-, 3-fold
	[T81] Yang et al.	Ni(19,14,8) embedded, Ni_{88} total cluster	CH_3 with Na, H, C and C	HF–SCF CSID	3-fold site
	[T82] Yang et al.	Ni(13,9,5) embedded, Ni_{62} total	CH_3O	HF–SCF CSID	1-, 2-, 3-fold HCP FCC
	[T83] Whitten	Fe(37,30,37) embedded, Fe_{18}, Fe_{19}, Fe(110)	H	HF–SCF ECP	

Continued

Geometry optimization		Electronic orbital analysis	Magnetic properties	Binding/ adsorption energy	Energy decomposition	Frequencies
Cluster	Adsorbate					
—	Yes	Dipole, orbital	Spin state	Yes	—	Yes
—	Yes	Population, charge transfer, PES	Complete PES for multiple spin states	Yes	CSOV	Yes
—	—	—	—	Interaction energy	CSOV	—
—	Yes	Dipole	Spin state	Yes	CSOV	—
—	Yes	Population	—	Yes	—	Yes
—	Yes	Dipole anal. charge electric field	—	Yes	—	—
—	Yes	IPs, orbitals	—	Yes	Yes	—
—	Yes	—	—	Estimates	—	Gas-phase organics only
—	Yes	Orbitals, IPs, population	—	—	—	—
—	Yes	Orbitals, IPs, population	—	Yes	—	—
—	Yes	Orbital	Spin state	Yes	—	—
—	Yes	—	—	Yes	—	Yes
—	Yes	Orbital population charge	—	Yes	—	Yes
—	Yes	—	—	Yes	—	—
—	Yes	Orbitals	—	Yes	—	Yes
—	Yes	—	—	Yes	—	—

(*continued*)

TABLE 1.

Method	Ref., author(s)[a]	Transition metal clusters	Adsorbates	CI	Adsorption sites
	[T84] Bonacic-Koutecky et al.	Ag_n and Ag_{n+} (n = 2–9), comprehensive cluster choices	—	CASSCF MRD-CI	—
	[T85] McKee	Ag_2, Ag_{2+}	O, O_2, C_2H_4	HF–SCF MP3	π, di-σ, perpendicular bridge
	[T86] Gropen et al.	Pt(4,1)	H, O	HF–SCF MCPF	4-fold
	[T87] Blyholder and Sellers	Pd_{15} model of Pd(110)	CO	HF–MBPT2 (ECPs)	Bridging
	[T88] Sellers et al.	Au(111) Au(100) model clusters	SH SCH_3	HF–SCF RECP MBPT2	2-, 3-, 4-fold
	[T89] Nakatsuji and Hada	Pd_2	Acetylene, ethylene, H_2, vinyl, H·	CASSCF MCSCF	π-bound H-2-fold
	[T90] Nakatsuji et al.	Pd atom "dipped," embedded into bulk	O_2	SCF, symm. adapted cluster CI	O_2 end on adsorption superoxo
	[T91] Cundari	$IR(PH_3)_2(X)$	CH_4, CH_3, H	HF–SCF, MP2	—
	[T92] Nakatsuji et al.	Pd and Pd_2	H2	CAS–MCSCF	Parallel to Pd_2 bond
	[T93] Balasubramanian	Cu, Ag, Au, Zn, Cd, Hg, Si, Ge, Sn, and Pb	H2	MCSCF/CI Relativistic CI	—
	[T94] Balasubramanian et al.	Pd and Pd^+	H and H-	MCSCF, FOCI	Pd–H, Pd–H^+
	[T95] Balasubramanian et al.	Pd and Pt	H2	MCSCF–MRSDCI	PdH^+, PdH_2, PtH_2
	[T96] Dai and Balasubramanian	PtAu and Pt_3Au	—	MCSCF, MRSDCI	—
	[T97] Langhoff and Bauschlicher	Comprehensive transition metal hydrides, halides, oxides, dimers, trimers	—	MCPF, MCSCF, CASSCF, full CI	—
DFT	[T98] Chesters et al.	Ni(12,6,7), Ni(16,9,4), Ni(8,9,4)	S	LCGTO, LDF	3-, 4-, and 5-fold

Continued

Geometry optimization		Electronic orbital analysis	Magnetic properties	Binding/ adsorption energy	Energy decomposition	Frequencies
Cluster	Adsorbate					
Yes	—	Orbitals	Ground state and spin states for each cluster, charged clusters, IPs	—	—	Ag_2 only
Yes	Yes	Orbitals, EAs IPs	Spin states for each cluster	Yes	—	Yes
—	Yes	—	—	Yes	—	—
—	Yes	—	—	Yes	—	Yes
—	Yes	—	—	Yes	—	Yes
Yes	Yes	Orbitals	—	Yes	—	—
—	Yes	Population	Spin states, PES	Yes	—	Yes
Yes	Yes	—	—	Yes	—	Yes, detailed anal. of coordinates
Yes	Yes	Ionization energy, state anal., orbitals	Spin states	Yes	—	Yes, force anal.
—	Yes	Comprehen. state anal., dipole orbitals	Comprehens. spin state	Yes	—	Comprehens. vibrational spectra for states
—	Yes	Comprehen. state anal.	Comprehens. spin state	Yes	—	Vibrational anal.
—	Yes	Comprehen. state anal., populations	Comprehens. spin state	Yes	—	—
—	—	Comprehen. state anal., orbital populations	Comprehens. spin state	—	—	Comprehens. spectro-scopic constants
Yes	Yes	Population orbitals states	Spin states	Yes	—	Yes
—	Yes	Charges	—	—	—	Yes

(*continued*)

TABLE 1.

Method	Ref., author(s)[a]	Transition metal clusters	Adsorbates	CI	Adsorption sites
	[T99] Neyman and Rösch	Ni(6,6), Ni(6,7), Ni(4,5), Ni(7,6)	NO	LCGTO, LDF	1-, 2-, 3-fold sites Ni(111)
	[T100] Pacchioni and Rösch	Ni(6,0), Ni(3,3), on Al_2O_3	CO	LCGTO, LDF	CO at 3-fold Ni_6 on $O_{12}H_6$ on Al_6
	[T101] Ackermann et al.	Ni_x (x = 3–44), $Ni_3(CO)_6$, $Ni_5(CO)_{12}$, $Ni_6(CO)_{12}$, $Ni_8(CO)_{16}$, $Ni_8(CO)_8(Pr)_6$, $Ni_9(CO)_{18}$, $Ni_{10}(CO)Ge(CO)_{20}$, $Ni_{32}C_6(CO)_{36}$, $Ni_{32}C_6(CO)_{36}$, $Ni_{44}(CO)_{48}$		LDF, FON	CO
	[T102] Rösch	Ni Ni_2, Ni_{14} Ni_{17}, Ni_{25} Al_{29}	CO and H_2 CO and K Na	LDF, FON	Na 4-fold K 4-, 3-fold
	[T103] Pacchioni et al.	Ni_{13}, Ni_{55}, Ni_{147}, $Ni_{147}He_{180}$	—	LDF fraction occup. no. (FON)	—
	[T104] Fan and Ziegler	No transition metals	—	NLDF, BP	—
	[T105] Versluis et al.	$RCo(CO)_4$, R = H, CH_3	CO, ethylene, RCOH	NLDF, BP	—
	[T106] Ziegler et al.	Cp2Sc–H and CpsSc–CH_3	H, CH_3	NLDF	—
	[T107] Ziegler et al.	Early and late transition metal Sc, Y, La, Mn, Tc, Re	Cp2MR, CPMR, R = H, CH_3	NLDF, BS	—
	[T108] Ziegler et al.	MX4, Cl_3MR, M = Th, U	X = F, Cl, Br, I, R = H, CH_3	NLDF	—
	[T109] Baerends and Ros	$Cr(CO)_6$, $Fe(CO)_5$, Ni_5CO RuO_4–	CO, O	LDF	—
	[T110] Baerends	Review transition metal surfaces	Various	LDF	—
	[T111] Ziegler	$Cl_3M–R$, 6(CO)M–R, M = Th, U, Mn, Tc, Re, Co, Rh, Ir $Fe(CO)_5$ $Fe(C_5H_5)_2$, $HCo(CO)_4$	R = H, CH_3	NLDF	—
	[T112] Janssens et al.	Rh_7, Rh_{15}, Rh_{12}, Rh(12,3), Rh(12,1)	K	LDF	1- and 3-fold

Continued

Geometry optimization		Electronic orbital analysis	Magnetic properties	Binding/ adsorption energy	Energy decomposition	Frequencies
Cluster	Adsorbate					
—	Yes	Charges, dipole Fermi level	—	Yes	—	Yes
Ni height, CO height	—	Charge, dipole population	—	Yes	—	Yes
Ni–Ni opt. symm. fixed	—	IP, DOS, eigenvalues	Unpaired spin anal.	Yes	—	—
—	Yes	Dipole, DOS, orbitals	—	Yes	—	Yes
—	—	IP, EA, DOS	Unpaired spin anal.	Yes	—	—
—	Yes	Orbital	—	—	—	Yes
—	Yes	Orbital	—	Yes	—	—
—	Yes	Orbital	—	Yes	—	Yes
—	Yes	Orbitals	—	Yes	—	—
—	Yes	Orbitals	—	Yes	—	—
—	Yes	UV vis, orbital density	—	Yes	—	IR, Raman
—	Yes	Orbital charge transfer	—	Yes	Yes	—
—	Yes	—	—	—	—	—
—	Yes	Charge, electrostatic potential, IP	—	—	—	—

(*continued*)

TABLE 1.

Method	Ref., author(s)[a]	Transition metal clusters	Adsorbates	CI	Adsorption sites
	[T113] Zonnevylle et al.	Co(6,3), Co(111) model	C Effect of O	LDF	3-fold, 3-fold subsurface
	[T114] Burghgraef et al.	Ni_7, Ni(7,3), Ni(3,7,3), Ni_{19}	CH_4, CD_4	NLDF, BS	Insertion geometry
	[T115] Ravenek et al.	Ir_4(td), Ir_{10}	—	LDF	—
	[T116] Biemolt et al.	Cu(8,3)	NH_x, O, OH	NLDF	1-, 2- and 3-fold
	[T117] van de Kerkhof et al.	Cu_6, Cu_9, Cu_{10}, Cu_{11}, Cu_{14}, Cu_{16}, Cu_{18}, R_{xn} on Cu(8,3)	NH_x, O, OH	NLDF	1-, 2-, 3-fold sites
	[T118] Biemolt et al.	Cu(1,4,1), Cu(5,4,1), Cu(5,4,5), Cu(9,4,5), Cu(7,3), Cu(8,3), Cu(8,6,2), Cu(12,6), Cu(4,5)	NH_3	NLDF	1-, 2-, 3-fold sites
	[T119] van Santen et al.	Co, Rh, Cu	CO, NH_3	NLDF, BP	1-, 2-, 3-fold
	[T120] Burghgraef et al.	Ni_1, Ni_7, Ni(13) Co_1, Co_7, Co_{13}	CH_4, CD_4	NLDF, BS	Insertion geometry
	[T121] Ellis et al.	Ni_4 Pt_2, Pt_4, Pt_9, Pt_{13}, Pt_{24}	H, H_2	LDF	1-, 2-, 4-fold
	[T122] Burns et al.	Pd(12,6)	NH_3	LDF	Complete PES surface
	[T123] Sosa et al.	1st and 2nd row transition metal atoms	Various ligands	LDF	—
	[T124] Nakao et al.	Pd_2	—	NLDF, BP	—
	[T125] Chen et al.	Many transition metal atoms	Various ligands	NLDF, BP	—
	[T126] Johnson et al.	—	—	NLDF, various NL corr.	—
	[T127] Russier and Mijoule	Pd_4, Pd(6,1)	H, O, C, CO	LDF	3-fold
	[T128] Müller	Cu(10,5), Pt(10,5)	H, H_2	LDF	1-, 2-, 3-fold
	[T129] Mijoule et al.	Ni_4, Ni(4,1), Ni(6,10), Ni(9,1)	C, N, O, CO, NO	LDF	3-fold

Continued

Geometry optimization		Electronic orbital analysis	Magnetic properties	Binding/ adsorption energy	Energy decomposition	Frequencies
Cluster	Adsorbate					
Local Surface relaxation	Yes	DOS, orbitals, charges	—	Yes	Yes	
—	Yes	Population	—	—	—	Yes (freq. at transition state)
—	—	Charges, LDOS	—	—	—	—
—	Yes	Population, orbital	—	Yes	—	—
—	Yes	Population, orbitals	—	Yes	—	—
—	Yes	Population, orbitals	—	Yes	Yes	Yes
—	Yes	Population, DOS, LDOS	—	Yes	—	—
—	Yes	—	—	—	—	Yes (freq. at transition state)
—	—	Population density, PDOS, orbitals	—	Yes	—	Yes
—	Yes	—	—	—	—	—
—	Yes	—	—	—	—	Yes
Yes	—	Orbitals, population	Spin state	Yes	—	Yes
—	Yes	All electron vs. pseudo-potentials	—	Yes	—	Yes
—	—	Self-interaction, corrections	Spin states	—	—	Yes
—	—	Charge	—	Yes	—	—
—	Yes	—	—	Yes	Yes	—
—	—	Charge	—	Yes	—	—

(*continued*)

TABLE 1.

Method	Ref., author(s)[a]	Transition metal clusters	Adsorbates	CI	Adsorption sites
	[T130] Santamaris	Ag(1–6) clusters	—	NLDF, BP (*in situ* SCF)	—
	[T131] Seminario et al.	Pd(1–22)	—	NLDF, PW	—
	[T132] Casarin et al.	Cu(22,16,22)	HCOO	LDF	Short bridge, cross bridge
	[T133] Mele et al.	Ni(5,4)	CO	LDF	Atop
	[T134] Salabub	Transition metal atoms and dimers	—	NLDF, BP	—
	[T135] Ushio et al.	Ni(2,2), Ni(3,4)	HCOO	LDF	η1-bident, η2-bridge
	[T136] Fournier et al.	Ni(5,4), 100 model	C	LDF	1-, 2-, 3-fold sites
	[T137] Mijoule et al.	Pd(3,1), Pd(3,3), Pd(6,3,1), NH_3 coadsorbate	CO, NH_3	LDF	3-fold NH_3 under Pd_x
	[T138] Malkin et al.	Simple organic molecules	—	NLDF, BP PW91	—
	[T139] Pápai et al.	Pd and Rh atom	Mono- and Di-CO	NLDF, PW	—
	[T140] Rochefort et al.	M_3MH, M_3XH, M_2MXMH, X_3XH, where M = Pd, Rh, X = Sn, Zn	H	LDF	3-fold, 4-fold, surface and bulk
	[T141] Pápai et al.	Rh_4, Rh_2Sn_2, RhSnRhSn	HCOO	LDF	η2-parallel to bridge
	[T142] Selmani et al.	Ag_2, Ag_4	O, O^-, O_2, O^{2-}	LDF	4-fold parallel and perpendicular
	[T143] Castro et al.	Fe, Fe^-, Fe^+	CO	NLDF, PW	—
	[T144] Pápai et al.	Pd_3	CCH_3	LDF	3-fold
	[T145] Goursot et al.	Rh_2, Pd_2, Rh_4, Pd_4	CO	NLDF, P-PW	1-, 2-, 3-fold
	[T146] Pápai et al.	Pd(2,2), Pd(3,4), Pd(2,4,6)	H_x	LDF	Bridge and pseudo 3-fold
	[T147] Fournier and Salahub	Ni_1, Ni_2, Ni_3, Ni_4, Ni(2,6,2)	O	NLDF, P-W	2-fold 4-fold
	[T148] Pápai et al.	Ni atom	C_2H_4	NLDF, P-PW, BP	C2V π-bound
	[T149] Fournier and Salahub	Ni(6,3,1), Ni(4,5,4), Ni(5,4,5)	H	LDF	Atop, 3-fold
	[T150] Mlynarski et al.	Ni_4 and Ni_5	H	NLDF, P-PW	3-fold, 4-fold

Continued

Geometry optimization		Electronic orbital analysis	Magnetic properties	Binding/ adsorption energy	Energy decomposition	Frequencies
Cluster	Adsorbate					
Yes	—	IPs	—	Yes	—	—
—	—	—	—	Yes	—	—
—	Yes	DOS, PDOS	—	Yes	—	—
—	Yes	Population	—	Yes	—	Yes
Yes	—	—	Spin states	Yes	—	Yes
—	Yes	Populations	—	—	—	Yes
—	Yes	Orbitals, population	Magnetism	Yes	—	Yes
—	Yes	Orbitals, population charge	—	Yes	—	Yes
—	—	Spin–spin coupling const.	—	—	—	—
—	Yes	Orbitals, population	Spin states	Yes	—	Yes
Cluster relaxation for Pd_4 and Pd_3Sn	Yes	Charges, population	—	Yes	—	Yes
—	Yes	Charges, population	—	—	—	Yes
—	Yes	Orbital	—	—	—	Yes
—	Yes	Orbital, population, PES	Spin state, PES	Yes	—	Yes
—	Yes	—	—	—	—	Yes
Only for dimers	Yes	Orbital, population	—	Yes	—	Yes
—	Yes	Orbitals, population, DOS	—	Yes	—	—
—	Yes	Orbitals, population, DOS	Magnetic properties, spin states	Yes	—	Yes
—	Yes	—	Spin states	Yes	—	Detailed freq.
—	Yes	Orbitals	Magnetic properties	Yes	—	—
Ni_4 with symmetry	Yes	Orbitals, population	Spin states	Yes	—	—

(*continued*)

TABLE 1.

Method	Ref., author(s)[a]	Transition metal clusters	Adsorbates	CI	Adsorption sites
	[T151] Raatz and Salahub	Ni(4,1), Ni(4,5,4), Ni(6,3), Ni(9,4,1), Ni(6)	CO	LDF/Xα	1-, 3-, 4-fold
	[T152] Baykara et al.	Pd_1, Pd(3,2,1,3)	H	LDF	1-, 3-fold
	[T153] Andzelm et al.	Pd_2, Pd_4, Pd_2Sn_2, Pd_3Sn	H	LDF	2-, 3-, 4-fold
	[T154] Baba et al.	Pd(6,2), Pd(10,4)	K^+, CO	LDF	2-fold, Co ads. effects
	[T155] Fournier et al.	Ni_9	H, O, C, N	LDF	4-fold
	[T156] Salahub et al.	Pd, Rh, Nb, Fe, Al, Ni and Co clusters	CO, HCOO, CO_2, C_2H_4	LDF and NLDF, P-PW	Various
	[T157] Castro et al.	$Fe_{1-5}(0,+,-)$	—	NLDF, P-PW	—
	[T158] Sirois et al.	Pd atom	CO_2	NLDF, P-PW	Various modes
	[T159] Pedocchi et al.	$Ni(CO)_4$ $Mo(CO)_6$	—	NLDF, P-PW	—
	[T160] Goodwin and Salahub	Nb_x clusters, $x = 1-7$	—	NLDF, P-PW	—
	[T161] Castro et al.	Fe_{1-5} clusters	—	NLDF, P-PW	—
	[T162] Goursot et al.	Ni_5, Ni_8, Ni_9, Ni_{25}, Ni_{41} models of (100)	O	LDF	1-, 2-, 4-fold
	[T163] Chubb et al.	5 layers of Mo, Mo(100)	Monolayer Cs	LDF	Different
	[T164] Wimmer et al.	5 layers of Ni, Ni(100)	Ordered 2×2 CO overlayer	LDF	—

[a]References for Tables 1 and 2 are listed separately after the text references.

simply indicates whether or not these energies are reported. In some instances, a breakdown of the specific energy terms comprising the adsorption is given. One example is that of the CSOV method employed by Bagus et al. [60]. We indicate which of these studies include this level of analysis in the *energy decomposition* column. The final column in Table 1 expresses whether or not a frequency analysis has been performed.

Table 2 is simply an extension of Table 1 which acts to summarize the chemistries studied in each system. The first three categories (transition metal clusters, adsorbates, and CI) are repeated from Table 1. The reactions studied are included under reaction pathways. Activation barrier estimations and more rigorous calculations are indicated in the column *activation*

Continued

Geometry optimization		Electronic orbital analysis	Magnetic properties	Binding/ adsorption energy	Energy decomposition	Frequencies
Cluster	Adsorbate					
—	Yes	Orbitals, population, LDOS	—	—	—	—
—	Yes	Orbitals, diffusion, PES	—	—	—	—
Pd_4 only	Yes	Orbital, charges	—	Yes	—	Yes
—	Yes	—	Spin states	—	—	Yes
—	Yes	Population	Spin state, magnetism	Yes	—	—
Al, Fe, Nb clusters	Yes	Charge	Spin states	Yes	—	Yes
Yes	—	Population	—	Yes	—	Yes
—	Yes	IP, XPS	Spin state	Yes	—	Yes
—	Yes	IP, BE	—	—	—	—
Yes	—	IP	Spin state	Yes	—	—
Yes	—	Orbitals	Spin states	Yes	—	Yes
—	Yes	—	—	Yes	—	Yes
Fixed	—	Orbital charge transfer, band structure	—	—	—	No
Fixed	—	Orbital charge transfer, band structure	—	—	—	—

energies. The final column, *miscellaneous*, covers other relevant information about the systems studied or the methods employed.

D. Outline of Concepts

We formulate a set of theoretical conclusions as statements or postulates useful for explaining the controlling surface chemistry for a significant number of catalytic reactions on different transition metal surfaces. The validity of the formulated statements is tied to the framework of the theoretical model from which they have been derived. In an actual experimental situation many different factors may result in the overall measured

TABLE 2

Summary of Empirical, Semiempirical, *Ab Initio*, and Density Functional Quantum-Chemical Analyses Applied to Chemisorption on Transition Metal Clusters: Reaction Pathways

Method	Ref., author(s)[a]	Transition metal clusters	Adsorbates	CI	Reaction pathways	Activation energies	Miscellaneous
BOC-MP	[T1] Bell	Cu, Pd	Formic acid	—	Formic acid decomposition	Estimate	—
		Cu, Pt, Ni, Fe/W,	CH_x, and CO species	—	Methanol synthesis from CO and CO_2	Estimate	—
		Fe/W, Ni, Pt	CH_x species	—	Hydrocarbon synthesis from H_2 and CO	Estimate	—
					Hydrocarbon decomposition paths	Estimate	—
	[T2] Benziger	Ni, Cu, Mo, Ru, Rh, Pd, Ag, W, Ir, Pt, Au	Various small molecules	—	Dehydrogenation of hydrocarbons	Estimate	—
	[T3] Paredes et al.	Pd, Pt, Ag, Au	H_2, O_2, OH, OOH, H_2O	—	H_2 and O_2 reaction paths	Estimate	—
	[T4] Patrito et al.	Pt, Pd, Rh, Ni	OH	—	Activation of OH desorption	—	Coadsorption effects
	[T5] Sellers	Au	CH_3SH, SH, H	—	Chemisorption and dissociation of CH_3SH	Estimate	—
	[T6] Sellers	Au, Ni	CH_3SH and SH, H_2	—	Decomposition of CH_3SH and H_2	Estimate	—
	[T7] Shustorovich and Bell	Pd, Cu	CO, CO_2, HCO, H_2CO, H_3CO, MeOH, HCOO, H_2O, H_2, H	—	Methanol synthesis from CO and CO_2 on Cu and Pd	Estimate	—
	[T8] Shustorovich and Bell	Ni, Pd, Pt	C, O, H, CO, HCO, CH_x	—	CO hydrogenation pathways	Estimate	—

	[T9] Shustorovich and Bell	Ag, Cu, Ni, W	O, N, H, OH, NH, H_2O, NH_2, NH_3, CH_3O, MeOH, $HCOO_x$, CH_x	—	OH, NH, and CH bond dissociation and the effect of coadsorbed oxygen	Estimate	—
	[T10] Shustorovich	Fe, Ni, Cu, W, Rh, Pt, Re, Ag, Pd	H, N, C, O, NO, CH_x, CH_xO, CH_3OH	—	Hydrogenation of CO and decomposition of HCOOH	Estimate	—
EHT	[T11] Sautet and Paul	Pd(44), Pt(44), Pd(49), Pt(49)	Ethylene, butadiene	—	—	—	—
	[T12] Minot et al.	Pt(7,3), Pt(10,5), Pt(12,7), embedded	CH_x fragments	—	—	—	—
	[T13] Zheng et al.	Ti(0001), Cr(100), Co(0001), slab calcs.	CH_3, CH_2, CH	—	CH_x coupling reactions ($CH_3 + CH_3 \rightarrow CH_3-CH_3$)	Estimate	Surface migration
	[T14] Saillard and Hoffmann	Ni and Ti, ML_x complexes, (111) surfaces	H_2 and CH_4	—	C–H and H–H activation on transition metal complexes and surfaces	—	Effects of slab thickness
	[T15] Sung and Hoffmann	Ni(100), Ni(111), Co(0001), Fe(110), Cr(110)	CO	—	—	—	—
	[T16] Sung et al.	Ni(111) slabs	NO	—	—	—	—
	[T17] Anderson and Choe	Pt_{15}	Ethylidine, ethylene	—	Ethylene hydrogenation by ethylidene, ethylene hydrogenation by surface hydrogen	Estimate	—
	[T18] Simon and Bigot	Ni(111), 605 atoms	K	—	—	—	Surface coverages
DIM	[T19] Richtsmeier et al.	Cu_3, Ag_3, and Au_3	—	—	—	—	Diatomics in molecules (DIM)

(*continued*)

TABLE 2. Continued

Method	Ref., author(s)[a]	Transition metal clusters	Adsorbates	CI	Reaction pathways	Activation energies	Miscellaneous
	[T20] Richtsmeier et al.	Cu_n, Ag_n, and Au_n, $n = 4-6$	—	—	—	—	DIM method
	[T21] Richtsmeier et al.	Li_3, Na_3, K_3, Rb_3, Cs_3, Cu_3, Ag_3, Au_3	—	—	—	—	DIM method
ZINDO	[T22] Estiu and Zerner	Rh_{13} and Rh_{19}	—	CI	—	—	—
	[T23] Estiu and Zerner	Rh_2-Rh_{14}	—	CI	—	—	—
	[T24] Estiu and Zerner	Ni_2, Ni_4, Ni_{13}	—	INDO/S CAHF CI	—	—	—
GVB	[T25] Upton and Goddard	Ni_{20} and Ni_{28}, (100), (111), (110)	H, Cl, Na, O, S	MCSCF	—	—	—
	[T26] Upton et al.	Ag_{24}, (110)	O_2	Double–single	—	—	—
	[T27] Low and Goddard	Pd atom	H, CH_3, H_2, C_2H_6	MCSCF	H–H and CH_3-CH_3 activation and dissociation	Yes	—
	[T28] Zakharov et al.	Ni(7,3)	H_2O	HF–SCF	—	—	—
	[T29] Ohanessian and Goddard	Sc^+-Cu^+, Y^+-Ag^+, La^+, Hf^+-Au^+	H, H^+		—	—	—
	[T30] Anslyn and Goddard	Mo, $MoCl_3$, $MoCl_4$	Alkylidene, ethylene	GVB with perfect pairing wave function	Mo–alkylidene complexes with ethylene, metathesis	—	—

	[T31] Carter and Goddard	Ag clusters	O, O_2, OH, C_2H_x, C_3H_x, OCH_2CH_2, OCH_2CHCH_3, $OCHCH_2$, $OCHCHCH_3$, OCH_2CHCH_2, C_2H_4O cycle, C_3H_6O cycle, OCH_2CH	GVB–PP GVB–CCCI	Extensive set of paths for olefin epoxidation cycle	Yes	Role of Cl^- and Cs^+ as electro-negative and -positive promoters
	[T32] Carter and Goddard	Ag_3X	X=O, O_2, Cl, OH, C_2H^{4+}	GVB–PP, CCCI	Pathways for ethylene epoxidation	Yes	Role of Cl^- and Cs^+
	[T33] Carter and Goddard	VO^+ and RuO^+, ScO^+ vs. NiO^+	—	GVBCI GVBPP GVB–RCI	—	—	—
	[T34] McAdon and Goddard	Li_n and Li_{n+}, n = 3–13, clusters	—	GVB–PP GVB–CCI	—	—	—
	[T35] McAdon and Goddard	Cu, Ag, Au, Li, and Na	—	GVB–PP GVB–CI	—	—	—
HF–SCF	[T36] Blomberg and Siegbahn	Ni atom	H and H_2	CASSCF CCI	Detailed PES for H_2 dissociation	Yes	—
	[T37] Seigbahn et al.	Ni_{13}, Ni_{14}, Ni_{34}, [100]	H_2 and H	MCSCF SDCI	H_2 dissociation	Yes	
	[T38] Jensen and Siegbahn	Zr^+, Ti^+, Be^+, Mg^+, Al^+, Si^+	CH_3, ethylene	MCPF	Insertion of olefin into $M–CH^{3+}$	Yes	Relativistic calculations
	[T39] Mitchell et al.	Ni atom	H, OH, H_2O	MCPF, CCSD(T)	Oxidative addition, insertion into H_2O	Yes	—
	[T40] Siegbahn and Wahlgren	Ni_x(5,9,17,33,37,41)	O	MCPF, CPP	3-, 4-fold sites	—	—
	[T41] Blomberg et al.	Pd_2	CH_4, CH_3, H	MCPF	Pd insertion into C–H of CH_4	Yes	Relativistic

(*continued*)

TABLE 2. Continued

Method	Ref., author(s)[a]	Transition metal clusters	Adsorbates	CI	Reaction pathways	Activation energies	Miscellaneous
	[T42] Backvall et al.	Pd atom	Cyclopropane	CASSCF, CCI	Cyclopropane ring opening routes	Yes	PES for Rxn
	[T43] Panas et al.	Ni_{13}, Ni_{20}, Ni_{25}	O, O_2	CASSCF, CCI	Oxygen dissociation	Yes	PES
	[T44] Blomberg et al.	Pd, Rh, Ni, Fe, Co atoms	C_2H_6, CH_3	CASSCF, CCI	C–C and C–H bond activation Addition and elimination Rxns.	Yes	Relativistic
	[T45] Siegbahn and Panas	Ni_3, Ni(4,1), Ni(12,9,4)	CH_x (x = 1, 3)	CASSCF, CCI	—	—	No 3d correlation
	[T46] Siegbahn et al.	2nd row trans. metal atoms	C_2H_4	MCPF, CCSD(T)	C–H bond activation to form vinyl hydride	Yes	Relativistic
	[T47] Blomberg et al.	2nd row trans. metal atoms	C_2H_4	MCPF, CCSD(T)	—	—	Relativistic
	[T48] Siegbahn	2nd row trans metal atoms	C_2H_2	MCPF, CCSD(T)	C–H bond activation of acetylene	Yes	Relativistic
	[T49] Siegbahn and Blomberg	2nd row trans. metal atoms	CH_4 and H_2	MCPF, QCISD	Oxidative addition of CH_4 and H_2 to trans. metal halide and hydride complexes	Yes	Relativistic
	[T50] Siegbahn	2nd row trans. metal atoms	CH_4, H	MCPF, MP2-, QSID	Olefin insertion into metal hydrogen bond, effects of covalent ligands	Yes	Relativistic
	[T51] Blomberg et al.	Pd(2+) complexes	Cyclopropane	CASSCF, CCI	Cyclopropane ring opening routes, corner vs. edge activation	Yes	—
	[T52] Siegbahn et al.	2nd row trans. metal hydrides (MH_x)	CH_4	MCPF	Oxidative addition of 2nd row trans. metal atoms and CH_4	Yes	Relativistic

[T53] Siegbahn and Svensson	2nd row trans. metal atom hydrides	CH_x	MCPF, QCISD, MP2	—	—	Relativistic
[T54] Siegbahn et al.	Ni_n (n = 4–40) Ni(100) models Cu_{n+} clusters	H, O, CH_2	MCPF, ECP	—	—	Bond preparation
[T55] Blomberg et al.	2nd row trans. metal atoms	CO, H, CH_3	MCPF, QCISD	Carbonyl insertion into M–H and M–CH_3 bonds	Yes	Relativistic
[T56] Blomberg et al.	2nd row trans. metal cations	CH_4	MCPF	Transition metal cation insertion into C–H bond of methane	Yes	Relativistic
[T57] Blomberg et al.	Pd and Pd_2	CO	CASSCF, MCCI, CPF	—	—	Relativistic
[T58] Blomberg et al.	Ni and Pd atom	H_2, CH_3, CH_3–CH_3	CASSCF, CCI	H_2 and ethylene dissociation	Yes	—
[T59] Siegbahn and Blomberg	1st row trans. metal atoms	Ethane, cyclopropane, cyclobutane	CASSCF, CCSD(T)	C–C scission, ring opening	Yes	Relativistic
[T60] Blomberg et al.	2nd row trans. metal atoms	NH_3	MCPF, CCSD(T)	N–H bond activation	Yes	Relativistic
[T61] Blomberg and Siegbahn	Ti, Y, Zr, Nb	N_2	CASSCF, MCPF	—	—	—
[T62] Hermann et al.	Cu_x (x = 1–25)	OH	HF–SCF, CI	—	—	—
[T63] Bagus and Illas	Ag_4	NO	MCSCF	—	—	—
[T64] Bagus and Illas	Cu_5	O	HF–SCF	—	—	—
[T65] Bagus et al.	Cu_4 and Cu_5	NO	MCSCF	—	—	—
[T66] Bagus and Pacchioni	Cu(16,9), Cu_5, Ag_5	K, NO SCN	SCF, limited MCSCF	4-fold	—	—
[T67] Ricart et al.	Cu(1,4)	CO	HF–SCF, CCI	—	—	—
[T68] Fernández-García et al.	Cu(1,4)	NO	HF–SCF	—	—	—

(*continued*)

TABLE 2. Continued

Method	Ref., author(s)[a]	Transition metal clusters	Adsorbates	CI	Reaction pathways	Activation energies	Miscellaneous
	[T69] Illas et al.	Cu(4,1), Ag(4,1)	O	SCF, CASCI, MP2, CIPSI	—	—	—
	[T70] Bagus and Hermann	Cu(1,4)	CO and NH_3	HF–SCF	—	—	—
	[T71] Ricart et al.	Cu(4,1), Ag(4,1), Cu(16,9), Ag(16,9), Cu(169,16), Ag(16,9,16)	O	HF–SCF	—	—	—
	[T72] Bauschlicher	Cu(1,4), Cu(9,4), Cu(9,4,5), Cu(21,12), Cu(21,12,5)	CO	MCPF	—	—	—
	[T73] Hermann	Li(4,5), Li(5,4), Cu(1,4)	O, CO pt. charges	HF–SCF	—	—	External field effects
	[T74] Hermann and Meyer	Cu_1, Cu_2, Cu_3	OCH_3	HF–SCF	—	—	—
	[T75] Pacchioni and Lambert	Pd_6, Pd_8, Pd_6, Au_6	C_2H_2, C_4H_6, C_6H_6, C_8H_8	HF–SCF	Cyclization of acetylene to benzene	—	Reaction paths
	[T76] Pacchioni and Koutecky	Pd, Pd_2, Pd_3, Pd_4	CO	HF–SCF, MRD–CI	—	—	—
	[T77] Pacchioni and Koutecky	Pd, Pd_2, Pd_3, Pd_4	H and CO	HF–SCF, MRD–CI	—	—	—
	[T78] Fischer and Whitten	Cu_9	O_2	HF–SCF, CISD	Oxygen dissociation	—	—
	[T79] Chattopadhyay et al.	Ni_{28} embedded, Ni_{62} total	NH_3	HF–SCF, CSID	—	—	—
	[T80] Yang and Whitten	Ni_{28} embedded, Ni_{62} total	CH_2, CH, H	HF–SCF, CSID	Association: CH + H → CH_2	—	Reaction path anal.

[T81] Yang et al.	Ni(19,14,8) embedded, Ni_{88} total cluster	CH_3 with Na, H, and C	HF–SCF, CSID	—	—	—
[T82] Yang et al.	Ni(13,9,5) embedded, Ni_{62} total	CH_3O	HF–SCF, CSID	—	—	Geometry PES
[T83] Whitten	Fe(37,30,37) embedded, Fe_{18}, Fe_{19}, Fe(110)	H	HF–SCF, ECP	—	—	—
[T84] Bonacic-Koutecky et al.	Ag_n and Ag_{n+}, $n = 2–9$	—	CASSCF	—	—	Relativistic
[T85] McKee	Ag_2, Ag_{2+}	O, O_2, C_2H_4	HF–SCF, MP3	Oxygen interactions with ethylene, O_2 dissociation	Yes	Relativistic
[T86] Gropen et al.	Pt(4,1)	H, O	HF–SCF, MCPF			
[T87] Blyholder and Sellers	Pd_{15} model of Pd(110)	CO	HF–MBPT2 (ECPs)	—	—	—
[T88] Sellers et al.	Au(111), Au(100) model clusters	SH, SCH_3	HF–SCF, RECP, MBPT2	—	—	Relativistic
[T89] Nakatsuji and Hada	Pd_2	Acetylene, ethylene, H_2	CASSCF, MCSCF	Hydrogenation of acetylene to ethylene, LHHW overall path	Yes	Relativistic
[T90] Nakatsuji et al.	Pd atom "dipped"	O_2	SCF, SAC–CI	—	—	Relativistic
[T91] Cundari	$Ir(PH_3)_2(X)$	CH_4, CH_3, H	HF–SCF, MP2	Oxidative addition of methane to Ir complex	Yes	—
[T92] Nakatsuji et al.	Pd and Pd_2	H_2	CAS–MCSCF	H_2 dissociation	Yes	Relativistic
[T93] Balasubramanian	Cu, Ag, Au, Zn, Cd, Hg, Si, Ge, Sn, and Pb	H_2	MCSCF, MRSDCI	H_2 dissociation	Yes	Relativistic
[T94] Balasubramanian et al.	Pd and Pd^+	H and H^-	MCSCF, FOCI	—	—	Relativistic
[T95] Balasubramanian et al.	Pd and Pt	H_2	MCSCF–MRSDCI	H_2 dissociation, PES	Yes	Relativistic

(*continued*)

TABLE 2. Continued

Method	Ref., author(s)[a]	Transition metal clusters	Adsorbates	CI	Reaction pathways	Activation energies	Miscellaneous
	[T96] Dai and Balasubramanian	PtAu and Pt_3Au	—	MCSCF, MRSDCI	—	—	Relativistic
	[T97] Langhoff and Bauschlicher	Comprehensive trans. metal hydrides, halides, oxides, dimers, trimers	—	MCPF, MCSCF, CASSCF, full CI	—	—	Review
	[T98] Chesters et al.	Ni(12,6,7), Ni(16,9,4), Ni(8,9,4)	S	LCGTO, LDF	—	—	—
	[T99] Neyman and Rösch	Ni(6,6), Ni(6,7), Ni(4,5), Ni(7,6)	NO	LCGTO, LDF	—	—	—
	[T100] Pacchioni and Rösch	Ni(6,0), Ni(3,3) on Al_2O_3	—	LCGTO, LDF	—	—	—
	[T101] Ackermann et al.	Ni_x (x = 3–44), $Ni_3(CO)_6$, $Ni_5(CO)_{12}$, $Ni_6(CO)_{12}$, $Ni_8(CO)_{16}$, $Ni_8(CO)_8(Pr)_6$, $Ni_9(CO)_{18}$, $Ni_{10}(CO)$, $Ge(CO)_{20}$, $Ni_{32}C_6(CO)_{36}$, $Ni_{32}C_6(CO)_{36}$, $Ni_{44}(CO)_{48}$	—	LDF	—	—	—
	[T102] Rösch	Ni Ni_2, Ni_{14}, Ni_{17}, Ni_{25}, Al_{29}	CO and H_2 CO and K Na	LDF FON	—	—	—

[T103] Pacchioni et al.	Ni_{13}, Ni_{55}, Ni_{147}, $Ni_{147}He_{180}$	—	LDF	—	—	—
[T104] Fan and Ziegler	No trans. metals	—	NLDF, BP	Reaction coordinate and transition state calculations for dissociation and isomerization	Yes	—
[T105] Verluis et al.	$RCo(CO)_4$, R = H, CH_3	CO, ethylene, RCOH	NLDF, BP	Hydroformulation reaction cycle, migratory insertion	Yes	—
[T106] Ziegler et al.	Cp_2Sc-H and $CpsSc-CH_3$	H, CH_3	NLDF	H–H and C–H activation	Yes	—
[T107] Ziegler et al.	Early and late trans. metal, Sc, Y, La, Mn, Tc, Re	Cp_2MR, CPMR, R = H, CH_3	NLDF, BS	—	—	—
[T108] Ziegler et al.	MX_4, Cl_3MR, M = Th, U	X = F, Cl, Br, I, R = H, CH_3	NLDF	—	—	Relativistic
[T109] Baerends and Ros	$Cr(CO)_6$, $Fe(CO)_5$, Ni_5CO RuO_4–	CO, O	LDF	—	—	—
[T110] Baerends	Review diff. trans. metal surfaces	—	LDF	—	—	—
[T111] Ziegler	M–R	R = H, CH_3	NLDF	Hydride migration, CO insertion into $Co-CH_3$	Yes	—
[T112] Janssens et al.	Rh_7, Rh_{15}, Rh_{12}, Rh(12,3), Rh(12,1)	K	LDF	—	—	—
[T113] Zonnevylle et al.	Co(6,3) Co(111) model	C, effect of O	LDF	—	—	—
[T114] Burghgraef et al.	Ni_7, Ni(7,3), Ni(3,7,3), Ni_{19}	CH_4, CD_4	NLDF, BS	C–H bond activation	Yes	Rate constants
[T115] Ravenek et al.	Ir_4, Ir_{10}	—	LDF	—	—	—

(*continued*)

TABLE 2. Continued

Method	Ref., author(s)[a]	Transition metal clusters	Adsorbates	CI	Reaction pathways	Activation energies	Miscellaneous
	[T116] Biemolt et al.	Cu(8,3)	NH_x, O, OH	NLDF	NH_3 dissociation, effect of atomic oxygen on overall cycle	—	Overall cycle energetics
	[T117] van de Kerkhof et al.	Cu_6, Cu_9, Cu_{10}, Cu_{11}, Cu_{14}, Cu_{16}, Cu_{18}, reaction Cu(8,3)	NH_x, O, OH	NLDF	NH_3 dissociation, effect of O on overall path and barrier	Yes	Overall energetics and activation barriers
	[T118] Biemolt et al.	Cu_6, Cu_{18}	NH_3	NLDF	—	—	—
	[T119] van Santen et al.	Co, Rh, Cu	CO, NH_3	NLDF, BP	NH_3 dissociation	—	Concepts, review
	[T120] Burghgraef et al.	Ni_1, Ni_7, Ni(13), Co_1, Co_7, Co_{13}	CH_4, CD_4	NLDF	C–H activation on Ni and Co	Yes	Rate constants
	[T121] Ellis et al.	Ni_4, Pt_2, Pt_4, Pt_9, Pt_{13}, Pt_{24}	H, H_2	LDF	—	—	—
	[T122] Burns et al.	Pd(12,6)	NH_3	LDF	—	—	—
	[T123] Sosa and Lee	1st and 2nd row trans. metal atoms	Various ligands	LDF	—	—	s.
	[T124] Nakao et al.	Pd_2	—	NLDF	—	—	Relativistic
	[T125] Chen et al.	Many trans. metal atoms	Various ligands	NLDF	—	—	Relativistic corrections
	[T126] Johnson et al.	—	—	NLDF, various NL corr.	Hydrogen abstraction	Yes	—
	[T127] Russier and Mijoule	Pd_4, Pd(6,1)	O, C, CO	LDF	—	—	—
	[T128] Müller	Cu(10,5), Pt(10,5)	H, H_2	LDF	H_2 dissociation	Yes	—
	[T129] Mijoule et al.	Ni4, Ni(4,1), Ni(6,10), Ni(9,1)	C, N, O, CO, NO	LDF	—	—	—

[T130]	Santamaris	Ag(1–6) clusters	—	NLDF, BP (*in situ* SCF)	—	—	—
[T131]	Seminario et al.	Pd(1–22)	—	NLDF, PW	—	—	—
[T132]	Casarin et al.	Cu(22,16,22)	$HCOO^-$	LDF	—	—	—
[T133]	Mele et al.	Ni(5,4)	CO	LDF	—	—	—
[T134]	Salabub	Trans. metal atoms and dimers	—	NLDF, BP	—	—	Review
[T135]	Ushio et al.	Ni(2,2), Ni(3,4)	HCOO	LDF	—	—	—
[T136]	Fournier et al.	Ni(5,4), 100 model	C	LDF	—	—	—
[T137]	Mijoule et al.	Pd(3,1), Pd(3,3), Pd(6,3,1), NH_3 coadsorbate	$CONH_3$	LDF	—	—	—
[T138]	Malkin et al.	Simple organic molecules	—	NLDF, BP, PW91	—	—	—
[T139]	Pápai et al.	Pd and Rh atom	Mono- and di-CO	NLDF, PW	—	—	Relativistic
[T140]	Rochefort et al.	M_3MH, M_3XH, M_2MXMH, X_3XH, where M = Pd, Rh, X = Sn, Zn	H	LDF	Hydrogen diffusion across surface and into bulk	—	—
[T141]	Pápai et al.	Rh_4, Rh_2Sn_2, RhSnRhSn	HCOO	LDF	—	—	—
[T142]	Selmani et al.	Ag_2, Ag_4	O, O^-, O_2, O_{2-}	LDF	—	—	—
[T143]	Castro et al.	Fe, Fe^-, Fe^+	CO	NLDF, PW	—	—	—
[T144]	Pápai et al.	Pd_3	CCH_3	LDF	—	—	—
[T145]	Goursot et al.	Rh_2, Pd_2, Rh_4, Pd_4	CO	NLDF, P-PW	C–O dissociation	—	Relativistic
[T146]	Pápai et al.	Pd(2,2), Pd(3,4), Pd(2,4,6)	H_x	LDF	—	—	Surface coverages
[T147]	Fournier and Salahub	Ni_1, Ni_2, Ni_3, Ni_4, Ni(2,6,2)	O	NLDF, P-W	—	—	—
[T148]	Pápai et al.	Ni atom	C_2H_4	NLDF, P-PW, BP	—	—	—

(*continued*)

TABLE 2. Continued

Method	Ref., author(s)[a]	Transition metal clusters	Adsorbates	CI	Reaction pathways	Activation energies	Miscellaneous
	[T149] Fournier and Salahub	Ni(6,3,1), Ni(4,5,4), Ni(5,4,5)	H	LDF	—	—	—
	[T150] Mlynarski et al.	Ni_4 and Ni_5	H	NLDF, P-PW	—	—	—
	[T151] Raatz and Salahub	Ni(4,1), Ni(4,5,4), Ni(6,3), Ni(9,4,1), Ni(6)	CO	LDF/Xα	—	—	—
	[T152] Baykara et al.	Pd_1, Pd(3,2,1,3)	H	LDF	—	—	—
	[T153] Andzelm et al.	Pd_2, Pd_4, Pd_2Sn_2, Pd_3Sn	H	LDF	—	—	—
	[T154] Baba et al.	Pd(6,2), Pd(10,4)	K^+, CO	LDF	—	—	K^- coadsorption
	[T155] Fournier et al.	Ni_9	H, O, C, N	LDF	—	—	—
	[T156] Salahub et al.	Pd, Rh, Nb, Fe, Al, Ni, and Co clusters	CO, HCOO, CO_2, C_2H_4	LDF, NLDF, P-PW	—	—	Review
	[T157] Castro et al.	$Fe_{1-5}(0,+,-)$	—	NLDF, P-PW	—	—	Cluster analysis
	[T158] Sirois et al.	Pd atom	CO_2	NLDF, P-PW	—	—	—
	[T159] Pedocchi et al.	$Ni(CO)_4$, $Mo(CO)_6$	—	NLDF, P-PW	—	—	—
	[T160] Goodwin and Salahub	Nb_x clusters, $x = 1-7$	NLDF, P-PW	—	—	—	—
	[T161] Castro et al.	Fe_{1-5} clusters	—	NLDF, P-PW	—	—	—
	[T162] Goursot et al.	Ni_5, Ni_8, Ni_9, Ni_{25}, Ni_{41} models of (100)	O	LDF	—	—	—
	[T163] Chubb et al.	5 layers of Mo, Mo(100)	Monolayer Cs	LDF	—	—	—
	[T164] Wimmer et al.	5 layers of Ni, Ni(100)	Ordered 2 × 2 CO overlayer	LDF	—	—	—

[a]References for Tables 1 and 2 are listed separately after the text references.

interactions. In the theoretical models explored here, however, the system is isolated. This decouples competing phenomena. We attempt to elucidate the relation between the formal theory based statements and the actual experiment. As was discussed above, first-principle computational quantum-chemical calculations have reached the point where reliable predictions for transition metal–adsorbate interactions are now possible. Our view is that the current limitations are primarily due to the cluster size effects discussed earlier. We emphasize the consequences of such model choices in a number of relevant examples in this review. It should also be pointed out that the inherent cluster size deviations can be minimized (at least at the DFT level) provided that: (1) the exchange and correlation effects are treated *in situ* of the SCF, (2) adsorbate as well as cluster geometries are completely optimized, and (3) a proper description of the ground spin state is given.

We start with adsorption theory, that is, the nature of surface–adsorbate chemical bond. We formulate general concepts through the results of EHT and DFT calculations to explain the binding nature of small molecules, radical fragments, and atomic adsorbates to surfaces. Many of the concepts discussed derive from a frontier molecular orbital theory treatment of calculation results. The focus is an understanding of bonding and antibonding orbital overlap.

The natural extension of surface adsorption is the activation of an adsorbate bond which ultimately leads to dissociation of the adsorbate–surface complex, that is, chemisorption. An important part of this paper is devoted to analysis of surface dissociation and its analogous counterpart, surface association. The transition states for dissociation of diatomic molecules such as NO and CO are analyzed. We also explore the activation of C–H and N–H bonds for different CH_x and NH_x species. The preexponential factor of the surface dissociation reaction depends on the mobility of the transition state complex. The paths of minimum activation energy are largely determined by backdonation of surface electrons into antibonding adsorbate orbitals. This leads to orbital symmetry matching requirements between occupied metal surface orbitals and unoccupied adsorbate orbitals. Many features of the dissociation path are found to be described quite well by the principle of minimum surface atom sharing [61].

Reactivity differences on metal surfaces can be estimated from thermodynamic information about the energy difference between the initial molecularly adsorbed state and the final fragment–adsorbate final state. When a diatomic molecule dissociates, adatoms are generated. According to Polanyi, the activation energy for dissociation scales with the overall energy of energy, as long as the reaction path is unaltered. It is found that this leads to a detailed understanding of the differences in reactivity between various metal surfaces or metal clusters.

The interaction of coadsorbates with one another on the surface may lead to associative recombination reactions. One example which has im-

portant consequences is the coadsorption of organics with oxygen. It is well known that precursor oxygen surface species can interact with adsorbates such as H_2O, NH_3, CH_4 to help facilitate the X–H bond activation [22, 62]. We examine in detail two specific examples: ammonia activation by atomic and molecular oxygen and the activation of epoxidation of ethylene by coadsorbed oxygen. We discuss how inspection of the reaction energy changes that occur in each of the elementary steps of the reaction cycle helps to identify potential rate-limiting paths and speculate as to the governing reaction intermediates in the complete catalytic cycle.

In a final section we probe the question whether catalysis is controlled by specific electronic requirements. The key is a proper understanding of the competing mechanistic steps of the catalytic reaction cycle occurring at specific reaction conditions. These changes in reaction conditions can often lead to changes in the optimum for a single specific reaction step. For example, while facile surface dissociation reactions often require strong interactions with the metal surface, pathways for desorption and association reactions favor much weaker metal–adsorbate interactions. This leads to Sabatier's principle that prescribes that the maximum rate of a catalytic reaction is usually found at an optimum catalyst–reactant interaction strength. The optimum depends on the reaction to be catalyzed. Clearly the optimum interaction will also control selectivity, for example, the suppression (or acceleration) of fragmentation reactions over association reactions. A well-known illustration of this principle has been provided by Norskov [63] for the ammonia synthesis reaction. In the final example, we analyze selectivity based on a theoretical analysis of the Fischer–Tropsch reactions.

II. THE SURFACE CHEMICAL BOND

A. Donation and Backdonation

As introduction to the quantum chemistry of the surface chemical bond, we summarize conclusions deduced by both conventional MO theory [6] and formal chemisorption theory [2, 4]. Isolated clusters, embedded clusters, and slab calculations on surfaces are the basis for most of this work and discussed in this section. The use of extended lattices [64] and cluster analysis (bare as well as embedded) have both been instrumental in elucidating the electronic surface structure and how it controls chemisorption. Cluster results were derived from conventional quantum-chemical methods; the surface and slab results discussed were primarily deduced from theoretical physics approaches, such as the Bethe lattice approach [57]. Based on the chemist's familiarity with orbitals, we start with the former approach and attempt to describe the results in terms of simple frontier molecular orbital theory [6c, 6d]. A simplification in FMO theory is to treat only the orbitals with the most substantial overlap, that is, the highest occupied

(HOMO) and lowest unoccupied orbitals (LUMO). Within the HOMO–LUMO description of chemical bonding, the interaction of two fragments is described in terms of virtual excitations between occupied and unoccupied fragment orbitals. Figure 1 illustrates some of the charge transfer mechanisms between adsorbate and metal surface fragments.

The donative interaction populates unoccupied metal surface orbitals by excitation of an electron from the occupied adsorbate orbitals, whereas the backdonative interaction populates unoccupied ad-molecule orbitals with electrons from the occupied metal surface orbitals. This is the well-known *donation/backdonation* mechanism attributed to Blyholder [65] for the description of CO on transition metal systems.

On a metal surface, electrons are distributed over many narrowly spaced metal orbitals that form a continuous energy distribution. In the molecule, however, the electrons are distributed over a few molecular orbitals that have relatively large energy differences.

The donative and backdonative interactions between occupied and unoccupied orbitals on the respective fragments result in attractive interactions. Repulsion arises from the interaction between two occupied fragment orbitals. This is due to Pauli repulsion and is directly tied to the exclusion principle that forbids electrons of equal spin to occupy the same orbital. Such a situation arises when occupied orbitals overlap. The repulsion is approximately proportional to the square of the overlap of the occupied fragment orbitals ψ_i.

$$E_{\text{rep}} \approx \sum_{i,j}^{\text{occ}} |\langle \psi_i^{\text{metal}} | \psi_j^{\text{ads}} \rangle|^2 \tag{8}$$

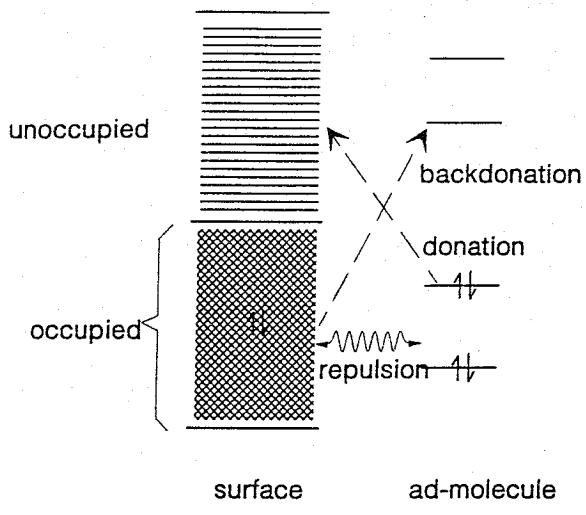

FIG. 1. Schematic illustration of HOMO–LUMO orbital scheme of ad-molecule and surface.

We first analyze the attractive and repulsive interactions that arise from the donative interaction. We start with general results derived from formal chemisorption theory and illustrate the concepts by presenting computed results for NH_3 interacting with a Cu cluster and for the methyl fragment interacting with a Rh cluster. Both cases are considered prototypes for donative interactions.

The highest occupied molecular orbital of NH_3 is the occupied lone pair orbital [Fig. 2(a)]. The lowest unoccupied molecular orbital, while antibonding with respect to the nitrogen–hydrogen bond, is significantly higher in energy. The chemisorptive bond is, therefore, dominated by the interaction with the ammonia lone pair orbital with little activation of the N–H bond.

A similar situation exists for the adsorption of a methyl fragment to the metal surface. The doubly occupied lone pair orbital [Fig. 2(b)] is directed toward the metal. The unoccupied antibonding C–H orbitals are much higher in energy, and therefore, only weakly interact with the metal surface. Within the HOMO–LUMO treatment, the CH_3 is adsorbed as a negative species to the metal surface.

Both the lone pair orbital energies for ammonia and methyl are lower in energy than the highest occupied metal surface orbitals and thus contribute to binding. The ammonia orbital energy, however, is significantly lower than that of a methyl. The relative energy difference between the metal surface orbitals and ad-molecule orbitals is explicitly dependent on the energy level of the highest occupied metal orbital (Fermi level) and the metal valence electron bandwidth. Ionic surface species, such as CH_3, typically have additional binding contributions due to the development of the surface dipole layer (Fig. 3) and induced image potential (Fig. 4) [66].

There are a number of factors which act to generate a surface dipole layer. In the absence of coadsorbate molecules, the dipole layer is due to spillover of electrons to the vacuum or smearing out of charge on atomically corrugated surfaces. On an atomically dense surface the dipole is directed

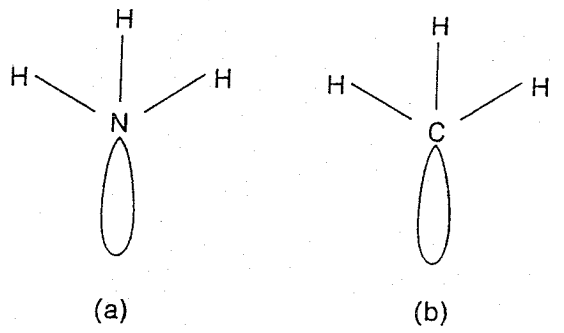

FIG. 2. The lone pair orbitals of NH_3 (a) and CH_3 (b) (schematic).

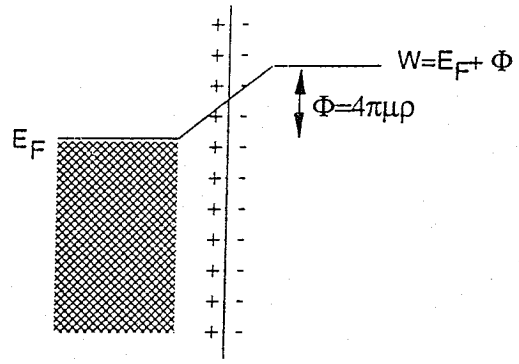

FIG. 3. Electrostatics of the surface-dipole layer. W is the work function, E_F the Fermi level, and Φ is the surface dipole potential. μ is the surface dipole moment and ρ its density.

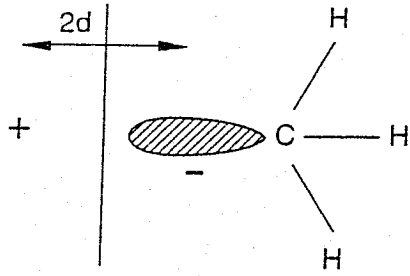

FIG. 4. The induced image potential energy: $-q^2e^2/4d$; q is the formal charge.

with its negative charge towards the vacuum, whereas on the more open surfaces the dipole magnitude decreases significantly and may even invert [8, 67]. The charge distribution of coadsorbed molecules and atoms, will also contribute to the surface dipole moment and cause the work function, Φ, to be coverage dependent. When the negative charge of the dipole layer is directed outward, it decreases the energy of electron donation from the adsorbate towards the metal surface orbitals. The conductive metal electrons will screen charges on an adsorbed molecule by developing an image charge. This acts to lower the energy changes required for electron donation or backdonation, when the separated fragments are considered to be neutral [66], as is the case for NH_3. The methyl fragment, however, behaves differently due to its negative charge.

It is useful to consider the changes in chemical bonding that occur when one compares the interaction of an adsorbate with a single atom versus that with a small cluster of atoms embedded (or nonembedded) in the infinite lattice of a metal. We analyze this within the Hückel or tight-binding

approximation. The molecular orbitals are considered as linear combinations of orthogonal atomic orbitals:

$$\psi_j = \sum_i c_i^k \phi_i \tag{9}$$

The orbital energy is computed by solving the secular equations deduced from Schrödinger's equation that contain the diagonal matrix elements $\langle i \mid H \mid i \rangle = \alpha_i$, which correspond to the energy of an electron in an atomic orbital i, and the interaction matrix elements

$$\langle i|H|j\rangle = \beta_{ij}\delta_{j,i\pm 1}$$

between atomic orbitals on atoms i and j.

As an illustration, Fig. 5 shows the orbital energies for two model nonembedded clusters. Figure 6 depicts the orbital energies of the corresponding embedded clusters. In Fig. 5(a) we consider the situation of an adatom, represented by orbital energy α_1 and atomic orbital ϕ_1, interacting

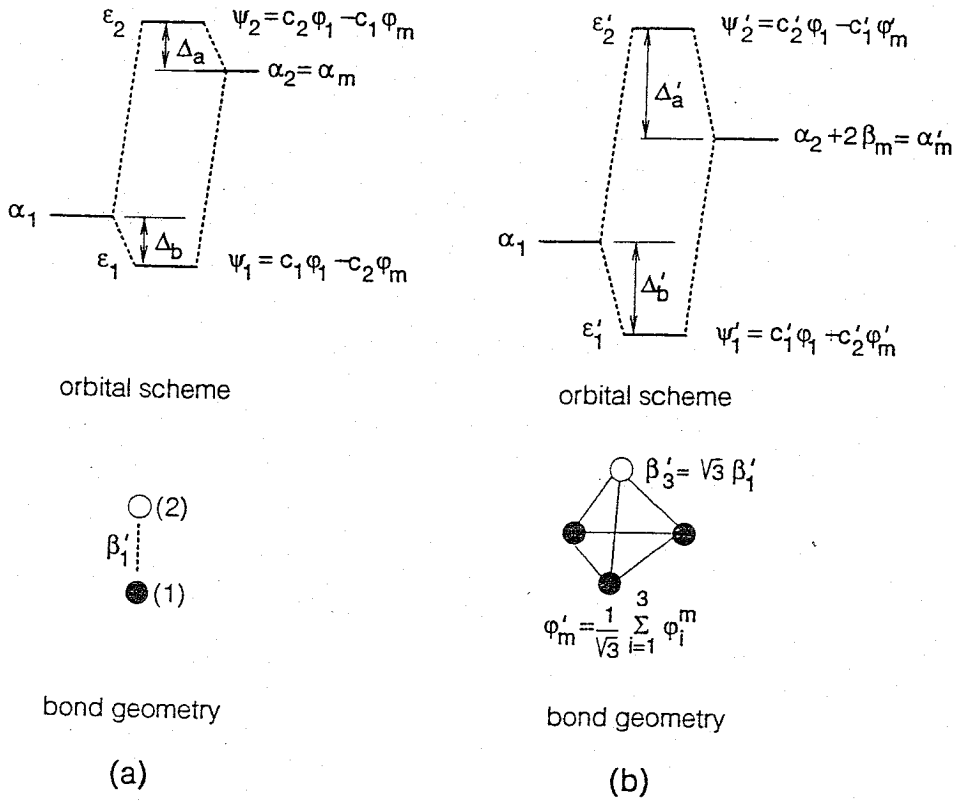

FIG. 5. Interaction energy schemes for clusters: (a) onefold coordination; (b) threefold coordination. $\beta_3' \leqq \phi_1|H|\phi_m' \geqq \sqrt{3}\,\beta_1'$. ○, adatom; ●, cluster atom; . . . overlap energy integral.

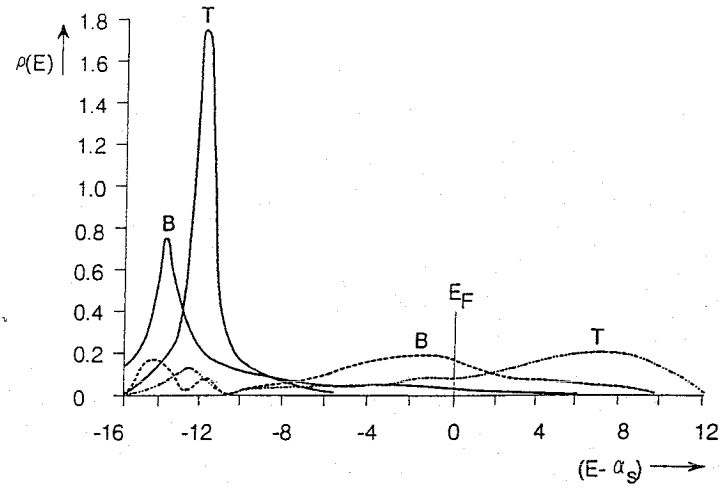

FIG. 6. CO 5σ-orbital interaction with s-valence electron band (Ref. 2, p. 147). LDOS $\rho_0(E)$ of interacting CO 5σ-orbital; T = atop; B = threefold. GO–LDOS of surface s-atomic orbital with CO chemisorbed atop (T). GO–LDOS of surface s-atomic group orbital with CO chemisorption threefold (B).

with a single metal atom, represented by orbital energy $\alpha_m(\alpha_2)$ and s-atomic orbital ϕ_2. In Fig. 5(b) the interaction of ϕ_1 is with a cluster of three such metal atoms, respectively. We are interested in the relative interaction energies as a function of the number of metal atom electrons. In this way we simulate the changes in bond energy as a function of the number of metal atom electrons for a given transition metal. This is especially relevant for examining the changes in bond energy with changes in occupation of the metal valence electron band. Such changes occur for the metal d-valence electron band if one compares transition metals along a given row in the periodic table. For the catalytically active transition metal systems, the number of d-valence electrons varies between 5 and 10. We simulate this in the model clusters by varying the fractional occupation of their s-atomic orbitals. The difference between s-atomic orbitals and d-orbitals is, of course, their spatial geometry, which results in a directional bonding effect for the latter.

When the adatom sits in the threefold symmetric position of the three metal atom cluster, its s-atomic orbital interacts only with the totally symmetric metal cluster orbital

$$\phi'_m = \frac{1}{\sqrt{3}} \sum_i \phi_i^m$$

with a corresponding Hückel molecular orbital energy $\alpha'_m = \alpha_m + 2\beta_m$. For the embedded cluster, the adatom orbital will interact with the same symmetry orbital, which is now delocalized by combining with additional

lattice orbitals. The fragment orbital ϕ'_m is then called the group orbital [2, 64]. The group orbital is the surface fragment orbital that is formed from the linear combination of surface atomic orbitals. It has the same symmetry as the adsorbate orbital it overlaps with. In the event that the adsorbate orbital has p-symmetry with respect to the surface normal, the corresponding surface group orbital becomes

$$\phi'_m = \frac{1}{\sqrt{2}}(\phi_1^m - \phi_2^m)$$

with a corresponding energy $\alpha''_m = \alpha_m - \beta_m$.

As illustrated in Fig. 5, the interaction of the adatom with cluster symmetry orbitals leads to bonding and antibonding combination orbitals. The bonding orbital energy shift, Δ, is larger for the threefold coordination situation due to the larger effective overlap energy integral $\beta'_3 = \sqrt{3}\,\beta'_1$ and the smaller energy difference between α'_m and α_1 compared to difference between α_m and α_1. Hence, when the interacting metal orbital is unoccupied by electrons and the adsorbate orbital contributes two electrons, threefold coordination will have the largest interaction energy. This changes, however, when the interacting metal orbital is occupied and already contains two electrons. Now the antibonding orbitals ψ_2 or ψ'_2 become occupied. This weakens the bond energy. When the overlap S_{1m} between adsorbate orbital ϕ_1 and the metal cluster atomic orbital is not neglected, the destabilization Δ_a of the antibonding orbital is always found to be larger than the stabilization Δ_b of the corresponding bonding orbitals. Hence, population of the antibonding orbitals leads to a repulsive interaction between the two fragments. This Pauli repulsion is larger for threefold coordination than for onefold coordination and can be shown [68] to be proportional to the adsorbate coordination number n_c:

$$E_{\text{Pauli}} \approx n_c S_{1m}^2 \tag{10}$$

This example illustrates three important features:

1. The bond energy decreases when antibonding orbital fragments become occupied by electrons.
2. High coordination sites are favored when electrons populate bonding orbital fragments.
3. Electron occupation of antibonding orbital fragments favors low coordination sites.

Statements 2 and 3 hold so long as bonding is nondirectional and overlap with coordinating atomic orbitals remains the same. Statements 1 through 3 are valid conclusions for both model clusters and the embedded model systems (discussed next). Direct comparison of these points with experiment, however, may or may not lead to the same conclusions. The reason, of course, is that in the experiment there are many additional factors which

can also contribute. For example, the number of d-valence electrons increases as one moves from right to left across a given row in the periodic system. In addition, the spatial extension as well as the energy of the d-valence electrons also change. Nonetheless, the interaction energy for many adsorbates with a transition metal surface will tend to decrease as one moves from left to right along a given row in accordance with the increase in the d-valence electron occupation. This relates to an increasing occupation of antibonding orbital fragments between surface atoms and adsorbate atoms. This holds experimentally, provided that one compares the same adsorbate at identical surface sites, surfaces with similar structures, and surfaces which do not undergo reconstruction [3d–3f]. A classic experimental example of this feature is the linear correlation for the heat of oxide formation with position along a constant row in the period which was developed by Tanaka and Tamaru [69].

The details of the adsorbate–metal fragment interactions control the adsorption geometry. Both donation and backdonation contribute to the total bond energy of the adsorbate–surface complex. In real systems, molecules will interact with d- as well as s- and p-valence electrons of the transition metal surface. Nevertheless, when the total d-valence electron count changes the donative interaction will follow rule 3, whereas the backdonative interaction will follow rule 2. The NH_3 adsorption case serves to nicely illustrate this point in terms of the donative interaction. We extend this point further in Sec. II.C.1 for chemisorption of CO.

The NH_3 adsorbate bond energy is dominated by the donative interaction of its lone pair orbital to the surface. The bond energy increases with a decrease in the energy differences between the empty metal surface orbitals and the occupied ammonia orbitals, as well as with increased overlap with surface orbitals. For transition metals, the ionization potential (work function) tends to increase with increasing d-valence electron occupation, until the d^{10} configuration is reached. At this point the work function decreases due to the dominance of the surface Fermi level by s,p-valence electron orbitals (Ni versus Cu). The increase in the interaction energy for NH_3 adsorbed to Ni [70] compared with Cu [71] then stems from three factors. First, compared to Cu, the antibonding orbital fragments between Ni d-valence orbitals and the NH_3 lone pair orbital have a lower occupation (rule 1 in reverse direction). Second, the work function for structurally similar surfaces is higher for Ni than Cu. Lastly, the larger spatial extension of the d-valence orbitals favors increased interactions further. When the adsorption of ammonia to Co is considered, however, the change in the ammonia interaction energy is less due to the decrease in the work function for Co. This counteracts the increase in the interaction energy due to the decreased d-valence electron occupation. It is indeed the case experimentally that NH_3 adsorbs more strongly on Ni(111) than on Cu(111) surface. Roberts reported a value of 50–60 kJ/mol for NH_3 on Cu(111) at low

coverages [71], whereas TPD results for NH_3 on Ni(111) at low coverages indicates a value of 80 kJ/mol [70].

Additional bonding features can also exist due to the differences in the nature of the dominant valence electron types near the top of the valence band. The contribution of metal s- and p-valence electrons to the total interaction energy varies anywhere between up to 80% for a metal such as Ni to approximately 30% for Pt [70]. Therefore the changes in this interaction (once again dependent upon the spatial extension and the relative energy with respect to adsorbate) will also affect comparison between different systems. We consider this interaction explicitly in Sec. II.B.

We now demonstrate how the same results follow for the interaction of ammonia with the embedded clusters. As was found for the small cluster, the analysis of embedded clusters enables us to estimate differences in reactivity on surfaces [64]. The metal atoms in the following model are again represented by one atomic orbital per atom.

The orbitals in the metal now form a band of closely spaced orbitals with a set of cluster orbitals distribute over it. This gives rise to a broadening of the originally discrete cluster orbitals. Figure 7 illustrates this embedding for two surfaces of a face-centered-cubic (fcc) lattice [64]. In delocalized electronic systems, a useful property for describing the electron energy distribution is the group orbital local density of states:

$$\rho_g(E) = \sum_i |\langle \phi'_m | \psi_i^m \rangle|^2 \delta(E - E_i) \tag{11}$$

ψ_i^m and E_i are the metal surface orbitals and their corresponding energies. The behavior of $\rho_g(E)$ is shown as computed for embedded systems with the Bethe lattice approximation [64] in Fig. 7. This approximation enables one to compute $\rho_g(E)$ correctly up to its second moment. Normalization requires:

$$\int dE \rho_g(E) = 1 \tag{12}$$

The dashed curves in Fig. 7 correspond to embedding into an open surface (where the surface atoms have a low coordination number); the solid lines correspond to embedding into a denser surface (where the surface atoms have a high coordination number).

The width of density of states relates to the number of nearest-neighbor atoms (Z_s) at the surface and the metal atomic orbital overlap energy integral β [68].

$$W \approx Z_s|\beta| \tag{13}$$

Delocalization of electrons increases with the increased interaction between neighboring atoms. Because of the increased width, W, and the normali-

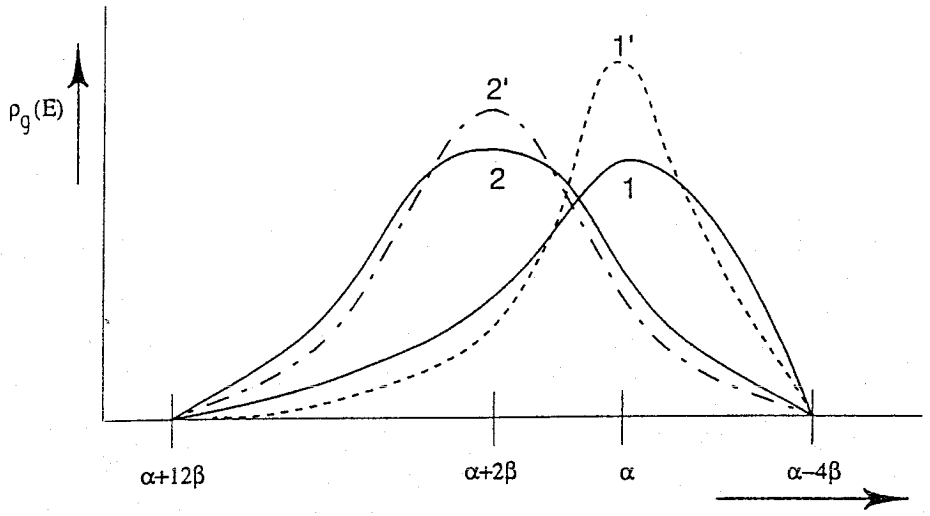

FIG. 7. Group orbital local density of states on face centered cubic lattice (schematic). Curves 1 and 1′ correspond to the local density of states of surface atomic orbital ϕ_m (onefold site). Curve 1 represents embedding in a dense surface, as the (111) surface, curve 1′ represents embedding in a more open surface as the (110) surface. Curves 2 and 2′ are the corresponding group orbital local density of states of:

$$\phi'_m = \frac{1}{\sqrt{3}}(\phi_1^n + \phi_2^m + \phi_3^n).$$

zation condition (5), the maximum of $\rho_g(E)$ decreases for densities with larger bandwidths W [68]:

$$\rho_g(E_{max}) \approx \frac{\sqrt{Z-1}}{Z_s|\beta|} \tag{14}$$

where Z_s is the metal atom coordination number of the surface atoms and Z the coordination number of a bulk atom. Note that the group orbital local density of states corresponding to threefold coordination, $\rho_{m'}(E)$, has its maximum value at $\alpha + 2\beta$ the energy of orbital $\phi_{m'}$ in the cluster.

Figure 8 illustrates the bonding and antibonding interactions that arise when the adsorbate orbital interacts with a surface atom or cluster that is embedded in the lattice. Now the bonding interaction results in a downward shift of the adsorbate orbital (Δ) that is less than that in the corresponding nonembedded cluster, due to the delocalization of electrons.

$$\Delta = \frac{n_c\beta'^2}{E_{max} - E_1 + \dfrac{Z_s\beta^2}{\alpha_m - \alpha_1}} \tag{15}$$

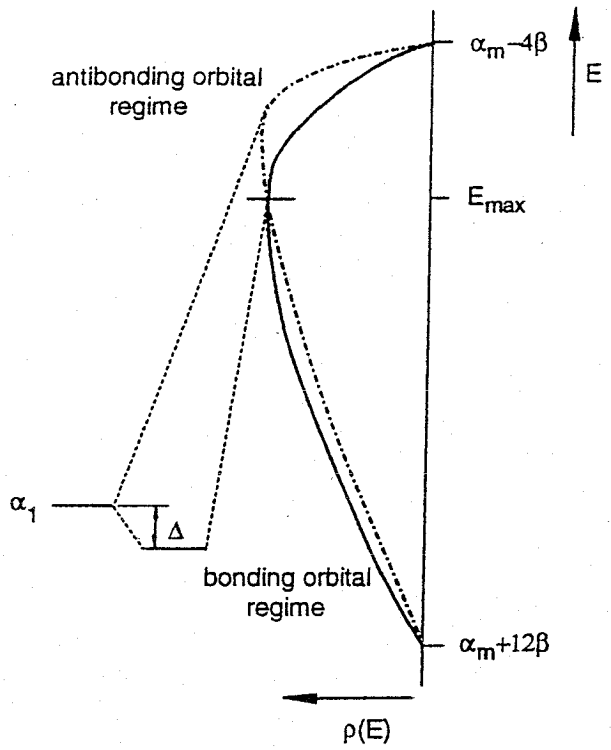

FIG. 8. The orbital interaction scheme of a donating adsorbate orbital interacting with a delocalized electron band (schematic):

$$\Delta \approx \frac{n_s \beta'^2}{E_{max} - \alpha_1 + \dfrac{Z_s \beta^2}{\alpha_m - \alpha_1}}.$$

One notes the decrease in stabilization Δ when the metal–metal interaction energy β or the number of surface metal atom neighbors increases [68].

The antibonding interaction gives rise to an upward shift of the metal cluster density of states. This results in a change of the surface metal–metal atom interactions, that usually decrease. This is seen experimentally in the form of surface reconstruction. van Hove and Somorjai [3c, 3d, 3f] have demonstrated surface reconstruction phenomena for a number of different systems. On Pt(111), for example, ethylidine pulls the three Pt atoms involved in adsorbate–surface bond up out of the surface. Their nearest-neighbor metal surface atoms are subsequently pushed down into the surface. This is due to the significant weakening of the metal atoms involved in adsorbate bonding, and their nearest metal atom neighbors. The overall interaction energy is found from the distribution of electrons over both bonding and antibonding fragment orbitals.

These results can be summarized by the following statements:

4. The attractive interaction of an adsorbate with a particular surface atom usually decreases when the number of metal atom neighbors of the surface atom involved in the chemisorptive bond increases.
5. The adsorbate–surface atom interaction alters the bonding between neighboring surface metal–metal atoms. It typically weakens the bonds between the corresponding surface atom and its nearest neighbors.

The validity of rules 4 and 5 is implicitly dependent on the electron occupation of the valence orbitals which contribute to the surface chemical bonds. Figure 9 illustrates a model system of a hydrogen atom interacting with an embedded cluster over a wide interval of different fractional surface orbital occupations. For low to intermediate surface valence electron band occupation, the surface atom with nine neighbors binds more strongly than surface atom with fewer neighbors. This difference increases when the surface orbitals are half filled, decreases when the surface electron occupancy increases further, and inverts at the valence electron band surface edges. We have extensively discussed the origins of this feature elsewhere [64, 68].

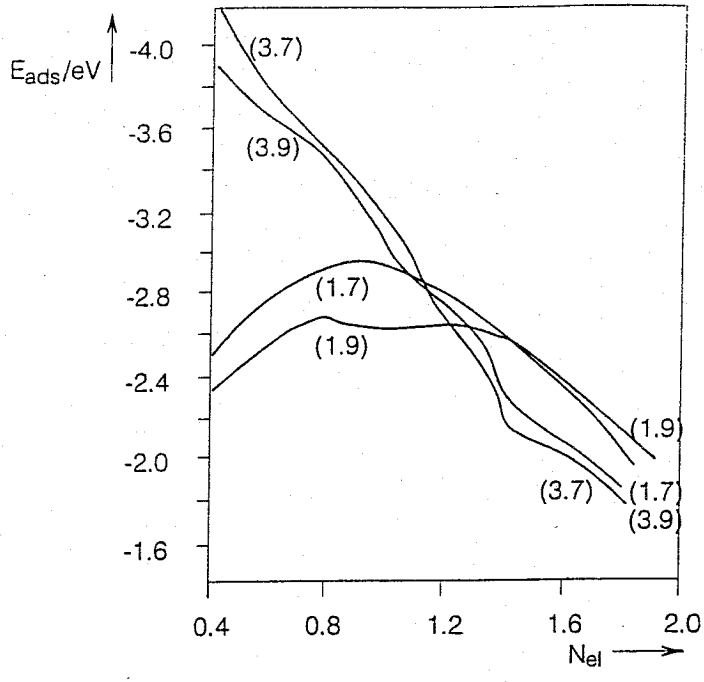

FIG. 9. Interaction of H atom with Bethe lattice as a function of (n_c, Z_s). Calculation for $\beta' = \beta$ (see Ref. 64).

It relates to the narrowing of the surface electron local density of states when the number of surface atom neighbors decreases. Due to the electron density conservation, the local density of states at the center of the valence electron band will increase, while that at the edges of the valence electron band decreases.

Since the electron occupation of the s,p-valence electron band is approximately one electron per atom, it behaves as expected with respect to rules 4 and 5 in that the interactions are governed by a partially filled valence band. Especially for elements with highly filled d-valence electron bands, the interaction with the s,p-valence electron band tends to dominate the interaction with adsorbates. This is probably the reason that rarely are experimental exceptions to rules 4 and 5 found.

Figure 6 shows the computed local density of states for onefold (T) and threefold adatom coordination (B) for interaction with a model cluster into a lattice modeling the (111) surface, where each surface metal atom has nine neighbors. Figure 9 depicts the bond energies as a function of metal atom electron occupation for two different surface atom coordination numbers. In Fig. 6 one observes the lower shift of the adatom local density of densities when adsorbed threefold rather than onefold. This follows from the larger difference in energy between $E_{\max}$ and α_1.

The bandwidth of the local electron density of states of the adsorbate atomic orbital for threefold coordination is larger than onefold, due to its higher coordination number [Eq. (6)]. The maximum surface electron group orbital density of states is higher for onefold than threefold coordination. This is of importance for the dependence of the relative energies of onefold or threefold coordinated adatom as a function of surface orbital electron occupation. When the valence electron occupancy is such that only bonded orbitals are occupied, the larger value of Δ results in higher coordination being favored. When the electron density, however, is greater, the antibonding orbitals also become occupied. The antibonding orbital fragments that correspond to the threefold coordination site become occupied at lower electron occupation than those corresponding to onefold coordination. At higher surface metal atom electron occupations, the onefold site may become more favorable. This behavior is confirmed by the calculational results shown in Fig. 9. When all orbitals are occupied, the repulsive interaction dominates. This is nicely illustrated by comparing the interactions and bonding of ammonia to Cu(111) and Ni(111). On Ni(111), the valence electron band is much more filled than the band for elements to the left on the periodic table. We again return to the results of ammonia on Ni versus Cu discussed earlier. Ammonia binds to Ni(111) at one-, two-, and threefold adsorption sites with nearly same adsorption energy, 80 kJ/mol [70]. On Cu(111), however, the additional valence electrons act to further weaken the N–Cu interaction and essentially drive ammonia to the onefold coordination site. This acts to minimize the Pauli repulsion associated with the

higherfold coordination sites. The adsorption energy on Cu is 60 kJ/mol [71], some 20 kJ/mol less than that on Ni.

These results support the earlier statements 2 and 3 by showing that increasing occupancy of antibonding adatom surface orbitals favors low adatom surface site coordination. We elaborate on the electronic changes that accompany ammonia and methyl adsorption in the next two sections.

B. *Donative Interactions of NH_3 and CH_3*

1. *Adsorption of Ammonia to Cu Clusters*

Ammonia is thought to interact with Cu through electrostatic (induced image charge potential) and weak covalent binding interactions. Ammonia binds to the surface through the nitrogen atom with the hydrogens directed away from the surface. The results of first-principle density functional theory calculations are used here to analyze the binding of ammonia to Cu. The calculations were performed on a series of clusters chosen to mimic Cu(111) and Cu(100) surfaces. The method used was the Amsterdam density functional (ADF) program suite developed by Baerends et al. [48a]. This method involves the self-consistent solution of the Kohn–Sham equations using an atomic basis set of Slater-type functions of double-zeta quality with polarization. The Vosko–Wilk–Nusair exchange-correlation potential [73] was used along with Becke [74] and Perdew [75] nonlocal gradient corrections for the exchange and correlation terms, respectively. While the clusters were fixed at bulk Cu–Cu distance [2.556 Å for Cu(111)], the adsorbate geometry was optimized on the cluster.

The results indicate that atop coordination is the favorable adsorption site. The predicted bond lengths, adsorption energies and frequencies were sensitive to the smaller cluster sizes. We carefully analyzed these cluster size effects and concluded that the minimum cluster required was one in which the adsorption site and complete set of nearest neighbors are required to mimic the electronic properties of the adsorbate–surface bond. For a onefold adsorption site on the (111) surface, this requires at least 10 atoms: the adsorption site and its nine nearest neighbors. The Cu(8,3) cluster which has 8 atoms in the surface layer and 3 that sit beneath coordinated to the central surface site was found to be an appropriate electronic model of the (111) surface. The results for DFT-computed and experimental adsorption energies are presented in Fig. 10. While the absolute predictions are good to within 25 kJ/mol due to the limited Cu(8,3) cluster size, the noted systematic underprediction can be used to provide far better estimates of adsorption energies.

The interaction between ammonia and Cu is weak; therefore it is a reasonable approximation to fix the Cu–Cu distances in the cluster to their bulk value, while allowing the geometry of ammonia on the surface to be

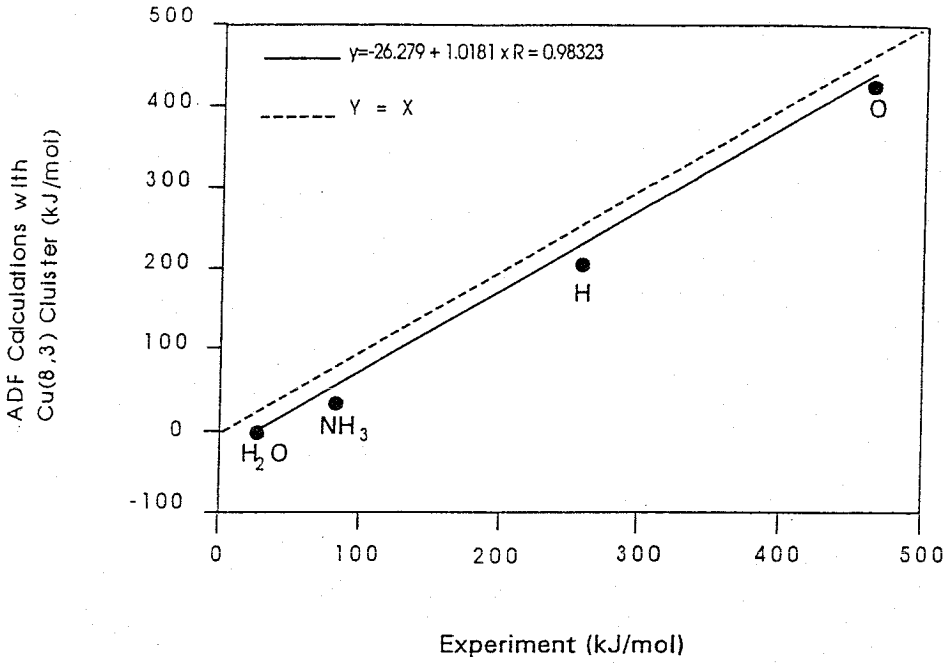

FIG. 10. Comparison of ADF computed adsorption energies on the model Cu(8,3) cluster and experimental adsorption values on the Cu(111) surface. The experimental values for NH_3, H_2O, H and O were taken from Refs. 141, 142, 143, 144, and 155, respectively.

TABLE 3

Computed Adsorption Properties of NH_3 on Cu [76]

	ΔE (kJ/mol)		$\tau_{N\text{-}Cu}$ (Å)		$\omega_{N\text{-}Cu}$ (cm^{-1})	
	111 surface	100 surface	111 surface	100 surface	111 surface	100 surface
Onefold	10	50	2.15	2.07	274	344
Twofold	—	10	—	2.48	—	180

optimized. The results presented in Table 3 are a comparison for onefold and twofold coordination of ammonia to Cu.

As was already stated, the onefold coordination of NH_3 is favored over twofold or higher coordination [76]. In addition, bonding to the more open (100) surface is stronger than to the denser (111) surface. The increased stability for ammonia binding to surface atom with 8 neighbor atoms, Cu(100), over one with 9, Cu(111), is attributed to the smaller delocalization of the Cu 4s and Cu 4p orbitals. This is in agreement with Eq. (15).

To understand the preferred atom coordination of NH_3, it is useful to

analyze the bonding and antibonding character of the copper–ammonia surface bond. The bond order overlap population density, π_{ij}^k, between atomic orbitals i and j at energy E_k:

$$\pi_{ij}^k = c_i^k c_j^k S_{ij} \tag{16a}$$

and its absolute sign can be used to analyze the bonding or antibonding character of a particular fragment orbital. When π_{ij}^k is positive, it is bonding; when it is negative, it is antibonding. The magnitude of the bond order overlap population P_{ij} is a measure for the strength of the corresponding contribution to the chemical bond.

$$P_{ij} = \sum_k^{\text{occ}} \pi_{ij}^k \tag{16b}$$

Figure 11.i presents the π_{ij}^k values of the lone pair orbital of NH_3 with the group orbitals of Cu, separated by contributions due to the 3d, 4s, and 4p Cu atomic orbitals. Two different surfaces are examined. The clusters used —Cu(9,4,5), a model for Cu(100); and Cu(8,6,2), a model for Cu(111)— are depicted in Fig. 11.ii. The results for Cu(9,4,5) are shown on the left-hand side, while those for Cu(8,6,2) are shown on the right. The results on both surfaces demonstrate the similar qualitative features.

Both bonding and antibonding fragment orbitals involving Cu- 3d atomic orbital interactions are occupied by electrons. The same holds true for the Cu-4s orbital interactions. In looking at the Cu-4p atomic orbital interactions, however, all appear to be bonding. The respective contribution of each interaction to the overall bond strength is estimated in Table 4. The overall interaction with the Cu-3d atomic orbitals is found to be repulsive, while that for the Cu-4s and Cu-4p atomic orbitals is attractive.

The repulsive nature of the ammonia lone pair and Cu-3d orbital interaction derives from the electron orbital occupancy of the Cu-3d valence electron band. The valence electron band is completely occupied with 10 electrons per metal atom and leads to considerable repulsive interactions. All corresponding bonding and antibonding orbital fragments become occupied. Twofold coordination results in a higher repulsion than onefold coordination, as can be deduced from the approximate expression shown in Eq. (10). The attractive interaction with the 4s-valence electrons is larger for onefold rather than twofold coordination, because of the significant contribution of antibonding fragment orbitals to this bond. As explained in the previous section, electron occupancy of antibonding orbitals favors low coordination.

For weakly interacting systems such as NH_3 on Cu(111), the electrostatic response of the surface electrons to the dipole and higher moments of NH_3 significantly contributes to the attractive part of the binding energy. In this example, the repulsive interaction between the NH_3 lone pair orbital

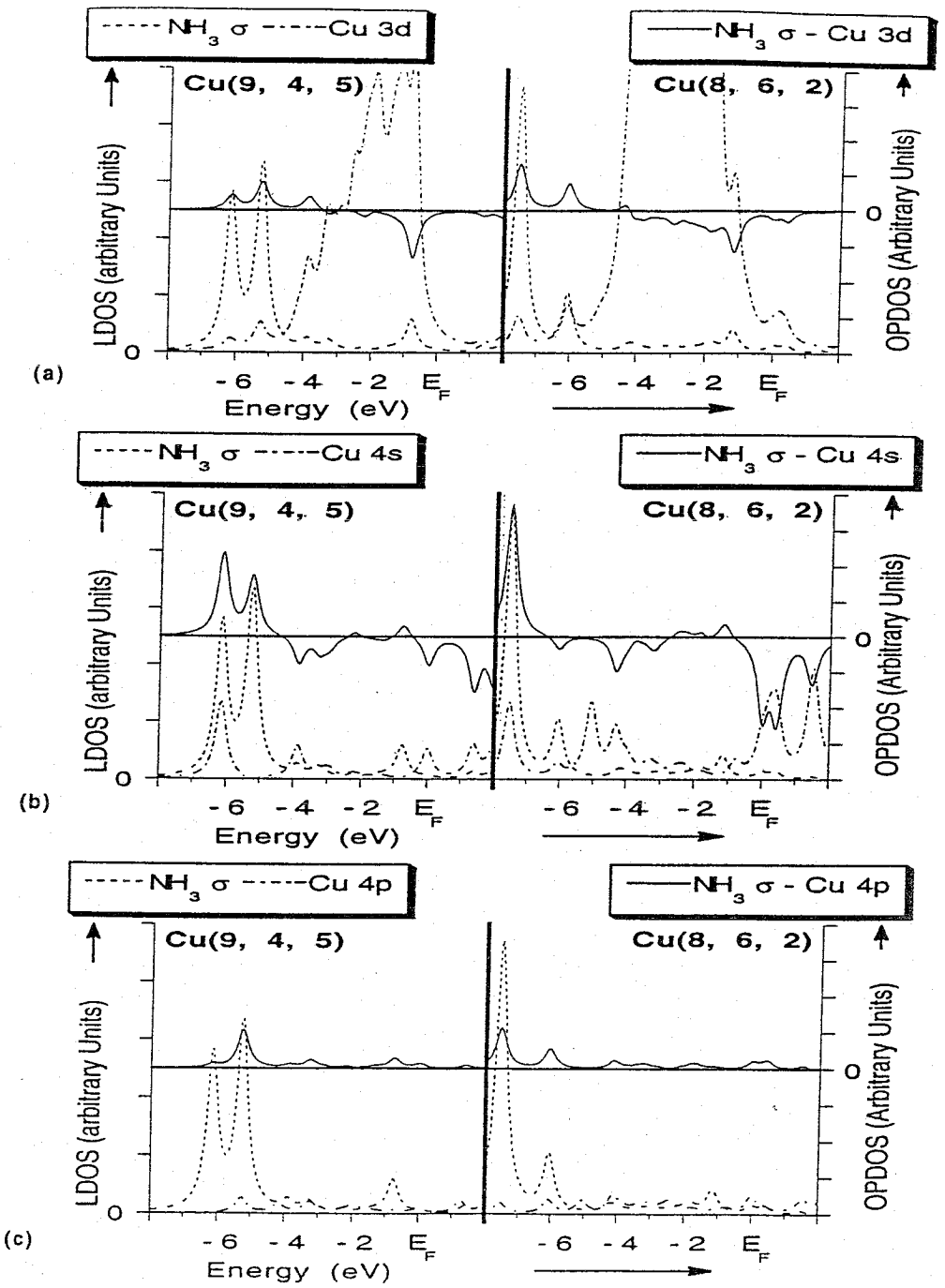

FIG. 11.i. Local density of states (LDOS) of the NH_3 σ-orbital, and the central copper 3d (a), 4s (b) and 4p (c) orbitals after adsorption together with the group orbital overlap population density of states (GOPDOS) between both: on the left for the (100) surface cluster Cu(9,4,5), and on the right for the (111) surface cluster Cu(8,6,2). Zero energy in these figures corresponds to the Fermi level E_F [76].

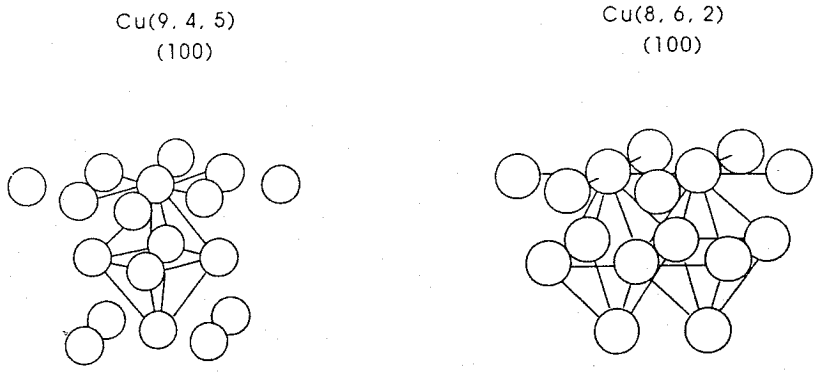

FIG. 11.ii. The clusters used by atop adsorption of NH_3(9,4,5) and twofold adsorption of NH_3(8,6,2).

TABLE 4

Bond Order Overlap Population of the NH_3 σ-Orbital with Selected Copper Orbitals (arbitrary units) [76]

Copper orbital	Cu(9,4,5)	Cu(8,6,2)
3d	−0.005	−0.157
4s	0.693	0.372
4p	0.572	0.737
Total	1.260	0.942

and the Cu-d electrons, however, counteract the attractive contributions of the image potential and drive NH_3 to the more preferred atop position.

2. *Adsorption of the Methyl Fragment*

Structurally, the nature of methyl binding to transition metal surfaces is quite similar to that of ammonia. The methyl group binds to the surface through the carbon, thus forming a near ideal sp3-hybridized center, where the three hydrogens are directed away from the transition metal surface. The unoccupied antibonding molecular orbitals of both gas-phase NH_3 and CH_3 are significantly higher in energy than respective atomic orbitals. For the chemisorbed molecular fragments, the high energy of the unoccupied adsorbate orbitals implies that backdonative interactions from the surface to the unoccupied N–H antibonding orbitals of ammonia are quite small.

The CH_3 antibonding orbital is, however, substantially higher in energy than the NH_3 lone pair orbital, and thus places it closer to the Fermi level. This allows for a greater mixing with both s and p surface orbitals. As a consequence, the lone pair orbital on CH_3 is more important than that on NH_3. This tends to favor more direct interactions with the s and p contri-

butions of the higherfold coordination sites. The adsorption of CH_3 on Ni (E_{ads} = 160 kJ/mol) is, therefore, found to adsorb 80 kJ/mol more strongly than ammonia on Ni (80 kJ/mol) and is indiscriminate to high or low coordination sites [79].

Recent first-principle calculations aimed at elucidating the adsorption energies and favored sites on Ni were carried out by Siegbahn [77, 78], Whitten [79] and Burghgraef et al. [80]. While the relative ordering of the favored adsorption site is slightly different, the adsorption energies are within reasonable agreement. Our DFT results [80] indicate that the onefold site is favored while Siegbahn and Whitten indicate that the higher threefold coordination site is favored. The energetic differences between different sites in all three studies, however, are really quite small. This is a strong indication of a *balance* between the attractive interactions which favor higherfold coordination sites and Pauli repulsion effects which favor atop adsorption. The governing features which control the balance are outlined later in this section.

The predicted values for favored sites by Siegbahn, Burghgraef, and Whitten are 39 kcal/mol, and 43 kcal/mol, and 48 kcal/mol (see Table 5). These trends for predicted adsorption energies follow the surface atom coordination number for the adsorption site in each study. Whitten [79] used an *ab initio* method and treated an extended cluster via embedding techniques. The coordination of the surface site/(sites) involved in the chemisorption bond is equivalent to that of a real (111) surface. Burghgraef et al. [80] used DFT calculations with both nonlocal corrections for the exchange and correlation corrections, and analyzed a 13-atom Ni cluster. The coordination of each surface atom involved in the bonding of CH_3 was 5. Siegbahn's analysis used an *ab initio* approach with correlation [78]. The Ni atoms in his Ni_3 cluster had a coordination number of 3. This appears to be reflected in the decreasing trend in binding energies found for the clusters with increasing delocalization of the metal cluster atoms involved in the metal–carbon bond.

The conceptual picture of CH_3 binding to transition metal surfaces was

TABLE 5

Theoretical Predictions for the Adsorption of CH_3 to Ni: The Effect of Surface Atom Coordination Number on Adsorption Energies

Author	Cluster	Method	E_a (kcal/mol)	Coordination number
Siegbahn [77–78]	Ni(3)	*Ab initio*	48	3
Burghgraef [80]	Ni(3,7,3)	DFT	43	5
Whitten [79]	Ni(28) embedded, Ni(62) total	*Ab initio*, embedded	39	9

well established by a series of early and informative semiempirical results by Zheng, Apeloig, and Hoffmann [81]; de Koster and van Santen [82]; and Minot, van Hove and Somorjai [83]. Bonding appears to be dominated by the local interaction of the d_z^2 surface orbital, and the singly occupied nonbonding CH_3 orbital, n, directed toward the surface. The d_{xz} and d_{yz} orbitals on the metal and the π^* CH_3 orbital can also contribute through backbonding, as is discussed in the next section. The partially occupied methyl orbital interacts strongly with the metal surface with a significant charge transfer from the d_z^2 surface orbital to the partially occupied orbital. Another way to look at binding is to consider the interaction of the CH_3^- with a positively charged metal surface orbital. The nonbonding, singly occupied, methyl orbital readily picks up an electron from the metal surface through charge transfer from the perpendicular d orbitals d_z^2, d_{xz}, and d_{yz}. The d orbitals in the surface plane $d_x^2-d_y^2$ and d_{xy} act to stabilize this transfer of electrons.

Zheng, Apeloig, and Hoffmann [81] looked at the differences in bonding as one moves across the periodic table from right to left and examined three cases, Ti(111), Cr(111), and Co(111). As was discussed earlier, the general trend in moving across the periodic table from left to right is an increase in work function. The balance is governed by a tradeoff between the increasing d-electron count and the increased Coulomb attraction due to a screening of nuclear charge as you move from left to right across a given row. The enhanced Coulomb interaction prevails and the work function increases. The three transition metal systems studied by Zheng et al., Ti, Cr, and Co, have corresponding work functions of 4.33, 4.5, and 5.0 eV, respectively. In addition, there is a change in surface dipole as one moves from left to right across the periodic table. This is attributed to the change in the valence band filling as one moves across a given row. As was discussed earlier, surface atoms have lower coordination numbers and, therefore, give rise to a much narrower band at the top of the valence band. The bottom of the band, which is attributed to the bulk atoms being filled first, takes on a negative charge. This leads to a positive surface charge. The increased filling of the band will subsequently populate the surface states. At some point there is great enough population of the surface states that the surface atoms become negatively charged while the bulk takes on a positive charge. Bonding of CH_3 is dominated by the methyl lone pair interaction with these surface metal states and is, therefore, a strong function of the relative position along a given row in the periodic table.

To help probe the methyl–surface interaction we compare it with the ammonia–surface interaction already discussed. The methyl group is considerably higher in energy than NH_3 and is therefore closer to the Fermi level. This enables the methyl group to overlap more strongly with s- and p-orbitals. As a consequence, the lone pair orbital on CH_3 mixes more substantially with s- and p-orbitals than the lone pair orbital on ammonia.

In the absence of Pauli repulsion, this would drive the methyl fragment to the higherfold coordination sites. Transition metals at the left of a given row will more likely favor higher coordination sites (minimal Pauli repulsion), while transition metals at the right may favor both low- and highfold coordination sites. The balance is governed by attractive overlap interaction and Pauli repulsion. As an example, we examine methyl adsorption on Rh(111) using an EHT (ASED) treatment on a large 50-atom model cluster [82]. The results indicate a preference for the onefold adsorption site over the higher threefold coordination site by 13 kcal/mol.

In an effort to understand the effects of the d-valence bandwidth on adsorption, we examined the changes in adsorption complex stability with the systematic change in the d-orbital spatial extent exponent, ζ_2. The results are depicted in Table 6. The differences in energy between the different adsorption sites strongly depend on the spatial extension of the 4d-atomic orbitals (the larger the d-orbital exponent ζ_2, the smaller its spatial extent).

As expected, onefold coordination is favored for the interaction with a nearly completely filled valence electron band when the spatial extension of the d-atomic orbital is large. The chemical bond then contains a strong contribution from the antibonding orbital fragments between the CH_3 lone

TABLE 6

Influence of Ni d-Orbital Exponent ζ_2 on Adsorption of CH_3: Extended Hückel Adsorption Energies as a Function of CH_3 Coordination [82]

ζ_2	Site	E_{att}[a] (eV)	h_X[b] (Å)
1.9	1-fold	−4.88	2.0
	2-fold	−4.67	1.7
	3-fold fcc[c]	−4.44	1.7
	3-fold hcp	−4.43	1.7
2.0	1-fold	−5.27	1.9
	2-fold	−4.90	1.7
	3-fold fcc[c]	−4.94	1.6
	3-fold hcp	−4.95	1.6
2.1	1-fold	−5.29	1.9
	2-fold	−5.06	1.7
	3-fold fcc[c]	−5.14	1.6
	3-fold hcp	−5.19	1.6
2.2	1-fold	−5.29	1.9
	2-fold	−5.18	1.7
	3-fold fcc[c]	−5.30	1.6
	3-fold hcp	−5.36	1.6

[a]Height of adsorbing species (C═X, H or C_x) above the surface.
[b]No Ni present in second layer.
[c]Ni present in second layer.

pair orbital and metal d-valence electron atomic orbitals. This is illustrated in Fig. 12 for the interaction of the CH_3 lone pair orbitals with the d-orbitals on the Rh surface atom coordination site. Figure 12(a), part (1), compares the LDOS of the d_z^2 atomic orbital on this Rh atom before and after adsorption. The d_z^2 orbital primarily contributes to the antibonding part of the surface–chemical bond and is, therefore, pushed upwards and partially depleted. This reduces its repulsive interaction and may even cause the interaction with the orbital d_z^2 to become attractive. As can be seen from Fig. 12(a), part (2), the methyl fragment does not interact with the surface Rh-d_{xz}-atomic orbital. Figure 12(b) depicts the bond order overlap population densities for the CH_3 lone pair orbitals with the surface $4d_z^2$-, 5s-, and $5p_z$-valence atomic orbitals. Bonding as well as antibonding surface fragment orbitals are occupied upon interaction with the surface d_z^2-atomic orbital. The s,p-valence electron interactions, however, are predominantly controlled by bonding orbital fragments and, thus, favor higher coordination sites.

As discussed, the spatial extension of valence d-atomic orbitals tends to increase for transition metals in moving from right to left across any given row in the periodic system. This is coupled with the decreasing occupancy of the d-valence moving from right to left. The spatial extension also increases moving down along any given column of the periodic system.

Differences in the strength of the adsorbate metal d-orbital interaction are often the reason for differences in coordination to metal surfaces. An interesting example is that of the adsorption of ethylene.

While ethylene is known to π-bond to the low index planes of a number of fcc transition metal surfaces, such as Ni, W, Ir, Fe, Pt, and Pd at low surface coverages, di-σ interactions are also possible. As recently discussed by Madix et al. [84] for results on Pd, the distinction is sometimes difficult and both modes can actually coexist at low temperatures. Sautet et al. [85] analyzed both π and di-σ on bonding of ethylene to Pt(111) and Pd(111) to help understand the electronic structural features which might favor one site over the other. While ethylene clearly favored di-σ coordination on Pt(111), both di-σ and π surface complexes were deemed reasonable on Pd(111). This agrees with the experimental results of Madix [84], who indicates that both π and di-σ modes are present for ethylene on Pd.

Due to symmetry, the interaction between the doubly occupied surface d_z^2-orbital and the doubly occupied ethylene π-orbital is repulsive [see Fig. 13(a)]. On Pd and Ni this repulsive interaction is small. On Pt, however, it becomes considerably larger due to the larger spatial extension of the 5d-atomic orbitals compared to 4d-atomic orbitals. Repulsion is minimized on Pt through rehybridization the s–p interactions. Ethylene now interacts via di-σ coordination to two Pt atoms, such that each lone pair on the carbon atoms is coordinated to only one surface Pt atom [Fig. 13(b)].

Bonding of ethylene to a metal surface cannot be properly understood

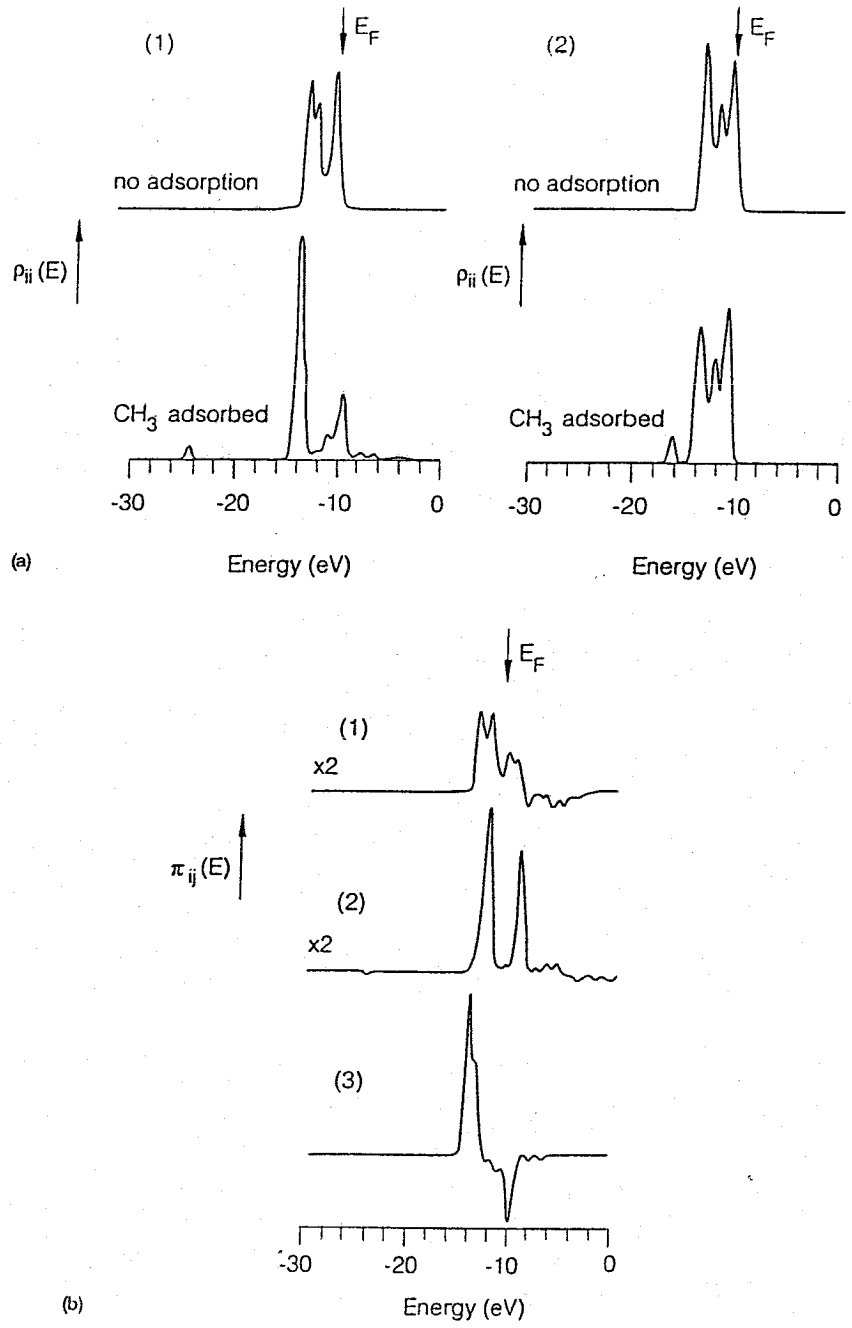

FIG. 12. (a) LDOS of Rh d_z^2 (1) and d_{xz} (2) before and after onefold adsorption of CH_3 on Rh(111) [82]. (b) Bond order overlap population densities of CH_3 with surface metal orbitals on Rh(111) [82]; (1) $n CH_{3-s}$, (2) $n CH_{3-pz}$; (3) $n CH_3 - d_z^2$.

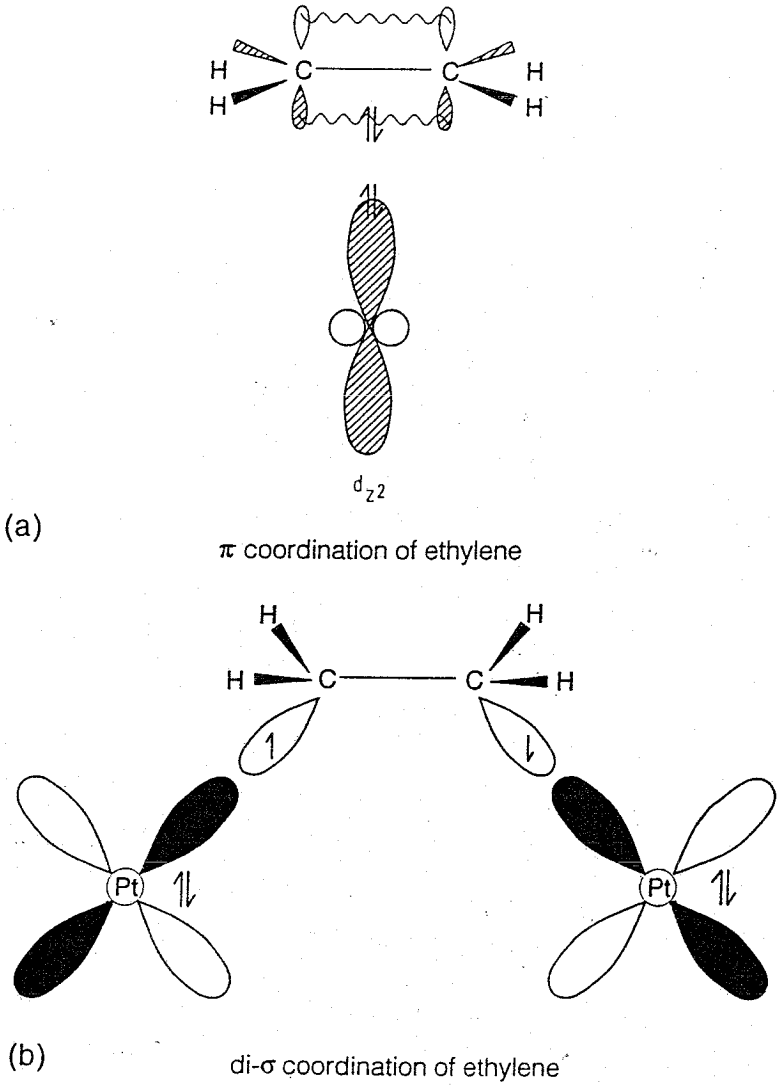

FIG. 13. (a) The repulsive interaction between a highly filled surface d_z^2 atomic orbital and the doubly occupied ethylene π-bond (schematic). (b) Rehybridization around the ethylene carbon atoms creates lone pair orbitals, each one-fold coordinated to a metal atom (schematic).

without considering both the donative and the backdonative interactions. Backdonation into the π^* orbital and its interaction energy is actually the subject of our next section. For the donative admolecule surface chemical bond, which involves partial occupation of antibonding adsorbate–surface orbital fragments, it is clear that the bond strength will decrease with increasing electron occupation of surface d-valence electrons. This is one of the factors that contributes to the observed trend that the adsorbate surface

chemical bond is weakened, when one moves from the left to the right along a row of transition metals in the periodic system.

In general, the strength of the donative interaction increases as the work function of the metal increases. The difference in the energy between the empty accepting surface orbitals and the occupied adsorbate orbitals decreases with increases in the work function. This occurs in moving from left to right across the periodic table. For NH_3 this will favor the interaction with Pt over Ni. For the interaction with the methyl group, one also has to consider the energy contribution due to the formation of the negatively charged CH_3 adsorbate species. Clearly the lower the work function, the greater the energy gain for ion formation. Platinum, which has a considerably greater work function than nickel, should, therefore, result in a much smaller contribution to the bond energy. As we will see later, electronegative adsorbates tend to bind more strongly to surfaces with lower work functions. This generally will result in higher reactivity for transition metals in the third row of the period table.

C. *The Backdonating Interaction: Chemisorption of CO, O_2, NO, Adatoms, and Intermediate Fragments*

1. *CO*

For diatomic molecules such as CO, NO, or O_2 that have only one molecular bond per atom, the difference between bonding and antibonding orbitals is much smaller. This implies that the backdonating interaction arising from the interaction between occupied metal valence electrons and unoccupied adsorbate molecular orbitals can no longer be ignored. To help elucidate these ideas we return to the CO adsorption example. CO binds perpendicular to the metal surface (Fig. 15) through the carbon atom to help optimize both donative and backdonative interactions. This is due to the lower electron affinity of the carbon atom. Coordination of a diatomic molecule can also occur parallel to the metal surface. While the parallel mode is common for the homonuclear diatomics such as O_2, N_2, and H_2, it can, in some instances, also occur for CO. The angle between the surface normal and the adsorbate internal bond direction depends on the balance of two factors. Overlap between the molecular $2\pi^*$-orbital and metal surface orbitals is optimum when the diatomic molecule is adsorbed parallel to the surface. This, however, is countered by the repulsive interactions between the doubly occupied orbitals. This repulsive interaction is overcome by low work function metal surfaces that can have a strong backdonating interaction with adsorbing molecules.

We use the interaction between the surface electrons of a Rh(111) and the lowest unoccupied molecular orbitals of CO, the $2\pi^*$-orbitals, to illustrate the quantum chemistry of the backdonative interaction [41] (Fig. 14).

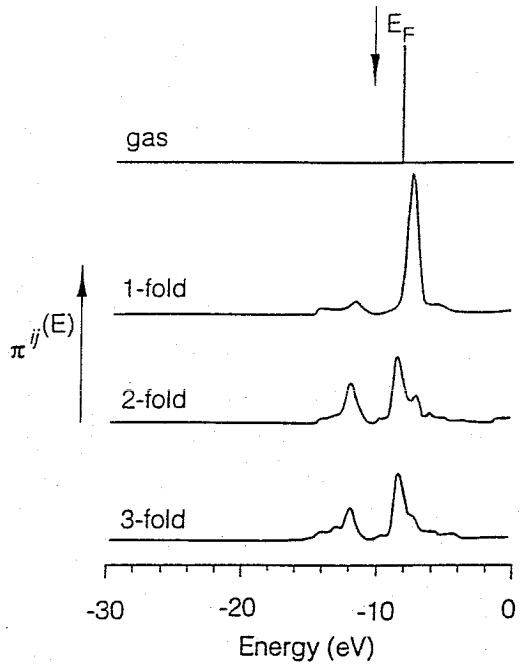

FIG. 14. LDOS of the $2\pi^*$ CO molecular orbitals in the gas phase, adsorbed on Rh(111) in onefold, twofold, and threefold coordination, respectively. The Fermi level is indicated by E_F [86].

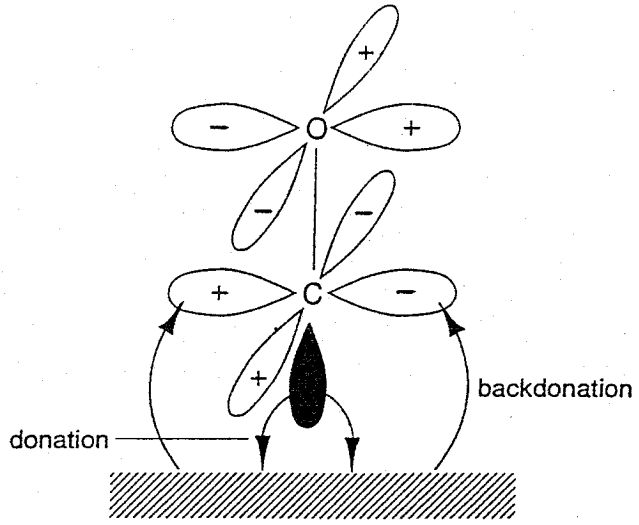

FIG. 15. Chemisorption of CO to a metal surface (schematic).

Results from extended Hückel calculations are presented here for the same cluster used in the previous section for the adsorption of a methyl fragment.

For CO adsorbed onefold, twofold, or threefold to the rhodium surface, the local density of states of the $2\pi^*$-orbitals of CO is shown in Fig. 14. When CO interacts with the transition metal surface, the single $2\pi^*$ CO energy level of the free molecule is split into two bands. The broadening of the energy distribution and the intensity of its low-energy part increases with increasing coordination number. The portion of the density of states which shifts upward in the manifold with respect to the vacuum corresponds to antibonding metal–adsorbate orbital fragments. The portion of the density of states which shift to lower energies, however, correspond to bonding metal–adsorbate orbital fragments. Figure 16 presents an analysis of the interaction in terms of bonding and antibonding orbital fragments.

The interaction of CO with the Rh d-atomic orbitals creates bonding as well as antibonding surface adsorbate fragment orbitals. The bonding orbitals are the only ones that are occupied. The interaction of the 5s and 5p Rh orbitals with CO is mainly of bonding character. The metal atomic orbitals dominate the bonding part of the backdonating CO surface interaction. The corresponding antibonding orbital fragments are mainly localized on CO. Electron occupation of bonding fragment orbitals favors sites of high coordination. The more d-valence electrons a metal contributes, the larger the occupancy of the corresponding bonding orbital fragments will be and the stronger the backdonating interaction. This leads to statement 6:

6. Backdonating interactions favor bonding to high coordination sites.

It follows from statements 1 and 3 (Sec. II.A) that donative interactions between the adsorbate and a surface behave opposite to that of backdonative interactions. For example, a low work function, which acts to increase the backdonative attraction, actually decreases the attractive donation interaction. The donative and backdonative interactions of CO on Rh with the metal d-atomic orbitals are schematically summarized in Fig. 17 [86].

We again point out that statement 6 refers to the consequence of theoretical models in which only one intrinsic parameter is changed, namely the number of d-valence electrons. As mentioned earlier, comparison with experimental evidence for components across a given row in the periodic table can only be made if there are no other features which also change. Isolating a single effect, however, is difficult to achieve experimentally. We illustrate this idea for the CO chemisorption problem just after presenting statement 7.

In analyzing CO binding, we see that the unoccupied $2\pi^*$ molecular orbitals accept electron density from the surface and thus become partially filled. Their electron occupation increases with increasing the coordination number about CO. This has an important consequence for the strength of

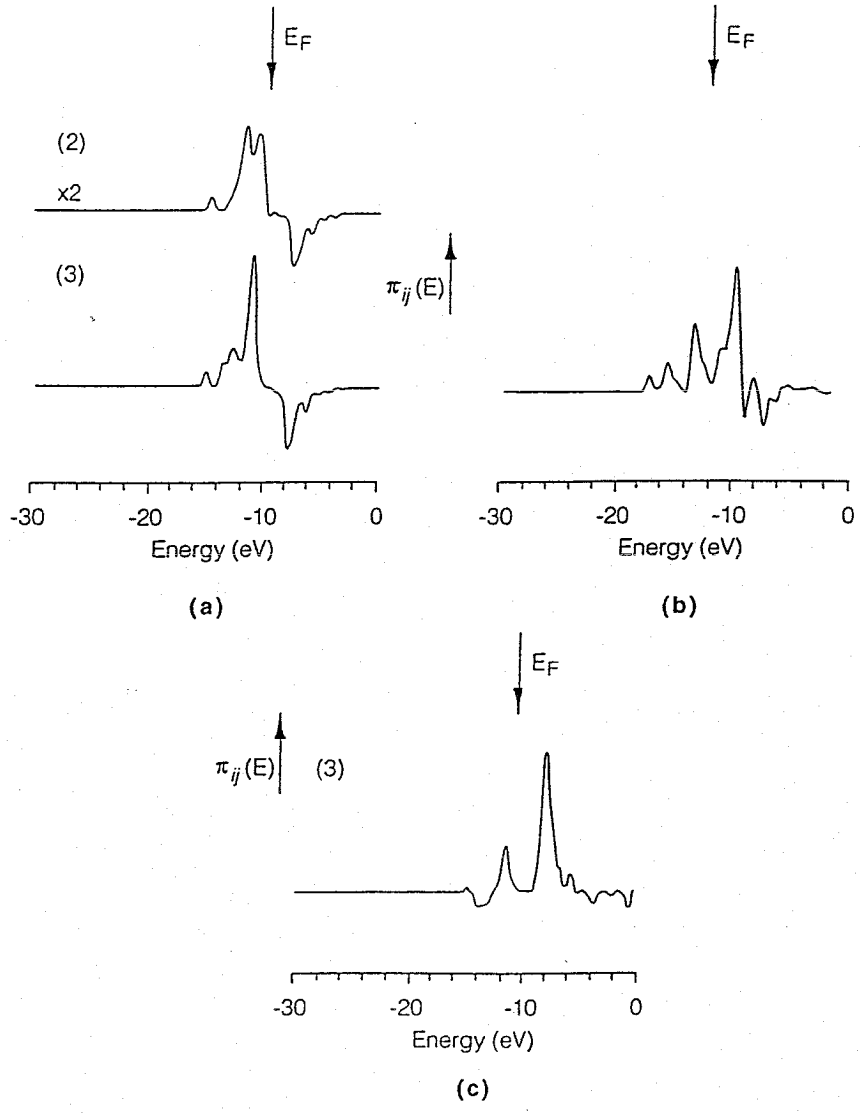

FIG. 16. Bond order group orbital overlap population densities of CO with surface metal orbitals on Rh(111). In all plots the Fermi level is indicated by E_F [2]:

(a) (1): CO twofold, $\left[\frac{1}{\sqrt{2 + 2s}}(d_{xz}(1) + d_{xz}(2))\right] - 2\pi^*$.

(a) (2): CO twofold, $\left[\frac{1}{\sqrt{2 - 2s}}(d_z^2(1) - d_z^2(2))\right] - 2\pi^*$.

(b): CO twofold, $\left[\frac{1}{\sqrt{2 - 2s}}(s(1) - s(2))\right] - 2\pi^*$.

(c): CO twofold, $\left[\frac{1}{\sqrt{2 - 2s}}(p_z(1) - p_z(2))\right] - 2\pi^*$.

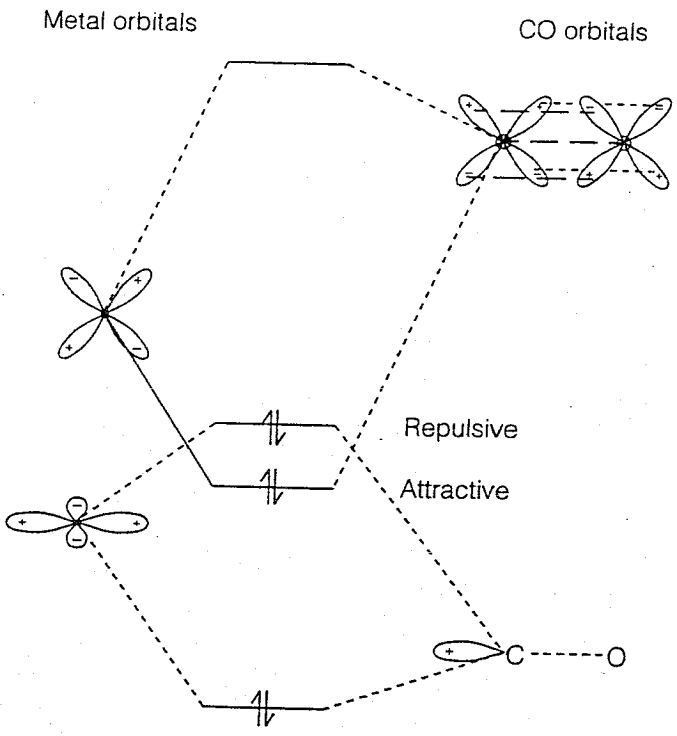

FIG. 17. Interaction of metal orbitals with orbitals of CO (schematic); above: interaction of d_{xz} of metal atom with $2\pi^*$-orbital of CO; below: interaction of d_z^2 of metal atom with 5σ-orbital of CO.

the C–O bond of chemisorbed CO. The CO $2\pi^*$ orbital is antibonding with respect to the C–O molecular bond. Therefore, any electron occupation of these orbitals ($2\pi^*$) weakens the C–O bond. CO bond weakening becomes larger when the CO surface coordination number increases. A weakening of the CO bond results in an elongation of the C–O bond length and a lowering of the CO stretching frequency. The general result can be stated as follows:

7. Electron backdonation into antibonding adsorbate orbitals weakens the internal adsorbate interactions.

The nature of CO 5σ donation, as well as the backbonding interaction on transition metal surfaces, was initially presented by Blyholder [65]. A direct consequence of statement 7 (as discussed later) is that the barrier for CO dissociation is tied to the degree of backdonation.

There have been an extensive set of experimental studies aimed at elucidating the nature of CO adsorption on transition metal surfaces. Many of these analyses follow the changes in CO stretch frequency upon adsorption [87] as a probe of chemisorption. For reasons cited earlier, the higher

coordination sites give rise to lower CO stretch frequencies than those for lower coordination sites. On Ni(111), for example, the C—O stretch associated with adsorption at a threefold coordination site is 1800–1850 cm^{-1}, while that for twofold coordination is 1910–1960 cm^{-1}, and that for onefold coordination is 2020–2100 cm^{-1} [88]. The comparison of statement 6 with available experimental information is only valid if the experiments are performed on similar surfaces and under essentially identical conditions. For example, if one compares CO chemisorption on Ni to Co, one will find that CO preferentially adsorbs bridging (twofold and threefold) [88] to Ni but is onefold coordinated to Co [89]. This is due to the very weak interaction with d-valence electrons for Ni, but the increased interaction with the spatially more extended d-valence electrons for Co. This results in a substantially more atop directing interaction with the CO s,p-orbitals for Co than Ni. As a consequence, the CO frequency on Co is higher than that on Ni. This is consistent with statement 5 if one takes into account the differences in surface adsorption sites. A similar situation holds when one compares the frequency of CO adsorbed to Cu and Ni. Whereas the d-valence electron band occupation is 10 electrons per atom for Cu, it is only 9 for Ni. The strong repulsive interaction with the doubly occupied d-valence electrons results in a strong repulsive interaction that forces CO to the atop site on Cu. As discussed earlier, backdonation from the atop adsorption position can only be attributed to the interaction with asymmetric d-atomic orbitals. The energy of the Cu d-valence electrons, however, is lower than that of Ni, thus making the backdonation of Cu d-valence electrons more difficult than on Ni. In comparing CO chemisorbed to Cu versus Ni, the donative interaction with the 5σ-electrons, once again, dominates CO coordination. The small spatial extent and low energy states for the Cu d-manifold typically result in weaker interactions with adsorbates, whereas the greater spatial extent and higher energy orbitals for Ni result in stronger interactions. The overall result is a stronger interaction of CO with Ni with a lower C—O stretch frequency for CO adsorbed atop than for that of Cu.

Nonlocal DFT cluster calculations which are aimed at analyzing the electronic differences and computing reliable adsorption energies are the focus of a forthcoming communication [90]. By allowing for both adsorbate and cluster optimizations, *in situ* nonlocal gradient corrections, and correct spin-state representation, we were able to predict adsorption energies to within 4 kcal/mol on relatively small clusters for Ni, Cu, and Pd. The cluster shapes chosen were those which corresponded to energy minimum. The results are depicted in Fig. 18.

A number of elegant theoretical treatments of CO binding on transition metal surfaces, which effectively demonstrated many of the concepts outlined here, also exist. A sampling of some of these include extended surface DFT analyses by Wimmer et al. [91] and Baerends [92]; DFT cluster calculations by Salahub [93] and Zonnevylle [94]; *ab initio* studies by Bagus

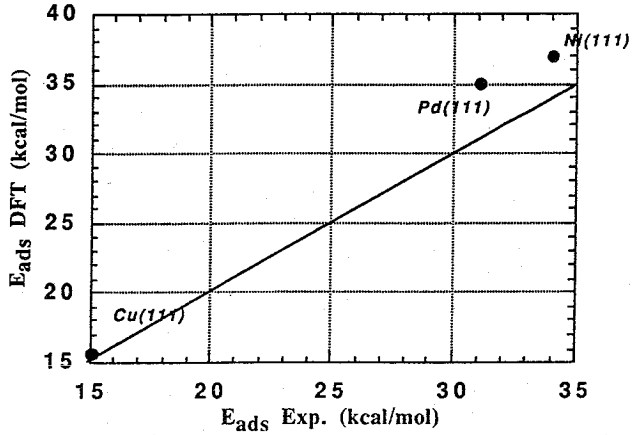

FIG. 18. Comparison of nonlocal DFT-computed adsorption energies for CO on Ni_6, Pd_6, and Cu_6 optimized clusters with experimental values for the corresponding (111) surfaces [90].

[95], Pacchioni [96], Blomberg [97], Raatz and Salahub [98], and Bauschlicher [99]; extended Hückel treatments by Hoffmann [100]; and the historical studies by Blyholder [65].

2. *O_2 and NO*

Various other molecular adsorbates follow similar donation/backdonation principles for adsorption. O_2 and NO are good examples. Oxygen has been cited as binding perpendicular, tilted and parallel to transition metal clusters and surfaces [101]. The low energy $2\pi^*$-orbital of oxygen is easily populated through backdonation from the surface. This is especially relevant in the parallel adsorption mode where the O–O bond is significantly weakened as typified by the long bond length and low O—O stretch frequencies. For all three modes, the mechanism involves the donation of electrons from the 2π-orbital of O_2 to available surface orbitals (on Cu this involves primarily the 4s- with some mixing in of 3d-orbital contributions), along with the subsequent backdonation from the surface to the $2\pi^*$-orbital of oxygen. As expected, this is accompanied with a charge transfer to the adsorbed oxygen. The charge transfer and occupation of the $2\pi^*$-orbitals lead to a weaker O–O bond. Both superoxo and peroxo intermediates have been suggested on different surfaces based on the degree of charge transfer and the weakening of the O–O bond.

We performed a set of DFT calculations (described earlier) and found that O_2 adsorbs molecularly on Cu(111) with a weak adsorption energy, 17 kJ/mol [76b]. This is consistent with experimental evidence on Cu [102]. Our results indicate that the threefold coordination is preferred. The dif-

ference between parallel and perpendicular adsorption modes is rather small, with the parallel mode being slightly favored. This is consistent with the relatively low experimental O—O stretch value of 660 cm^{-1} reported by Backx et al. [103] for O_2/Ag, which suggests a peroxo O_2(2-)-like surface species. Results from the calculated Mulliken population for O_2-parallel indicate that both oxygens pick up a substantial negative charge from the surface and a peroxo species is formed. This results in a substantially weaker O–O bond (1.43 Å), as is indicated by the 0.22 Å increase in bond length from gas-phase molecular oxygen (1.21 Å). The results for binding O_2 perpendicular differ primarily in the degree of charge transfer, and subsequently O–O bond weakening. A superoxo-like surface species is now predicted with a O–O bond length of 1.30 Å. These results are consistent with those found by Fischer and Whitten [104].

Turning our attention to other transition metals, the interaction of molecular oxygen with palladium was found to be somewhat stronger than that for O_2 with silver. Experimental results indicate a binding energy of 32–50 kJ/mol with a stretch frequency of 485 for Pd—O and 1035 for O—O. This considerable O—O shift (1035 cm^{-1}) suggests a peroxo surface species. Theoretical results by Nakatsuji et al. [105] also follow these general overall trends. They predict an adsorption energy of 22 kJ/mol with corresponding Pd–O and O–O bond lengths of 2.15 Å and 1.4 Å. Vibrational frequencies of 338 and 1250 cm^{-1} were reported for Pd—O and O—O, respectively.

Oxygen on Ag[110] also prefers to bind as a peroxo surface species [106–107]. This is confirmed by the significantly longer O–O bond length (1.47 Å) and very low O_2 stretch frequency (630 cm^{-1}) [103, 107]. Both the π^*- and the σ^*-orbitals are highly populated in the adsorbed surface state.

Experimental and theoretical results on Pt indicate that O_2 binds as a superoxo(1-) species. Bond lengths of 1.32 Å [106, 107] and O—O stretch frequencies of 870 cm^{-1} [109] were reported. These structural and infrared results are similar to the superoxo species reported by Panas for O_2 on Cr(110) [107].

The general bonding concepts for molecular O_2 adsorption are the same regardless of the adsorption complex formed. As was the case for CO adsorption, there is a donation from the O_2 π-orbital and a backdonation from the surface into O_2 π^*. Kamath and Rao [109] found molecular oxygen surface species on Ni, Cu, Ag, and Pt, and clearly identified distinct bands at 710, 766, 630, and 887 cm^{-1} which are attributed to the O—O stretch on each of these surfaces, respectively.

The analysis of NO adsorption is analogous to CO, in that NO typically binds to the surface primarily through the more electronegative nitrogen atom. There is, however, some recent evidence that on Ag(111), at low coverages, adsorption may occur through the oxygen [111]. From our DFT

calculations on Cu(111), we find that NO binds perpendicular to the surface and prefers the threefold coordination sites [76b, 111]. An optimized Cu–N distance of 2.18 Å was found. The computed adsorption energy is 83 kJ/mol. These results agree quite favorably with the *ab initio* calculations performed by Bagus et al. [112] and Fernández-García and Conesa [113]. The theoretical results on Ni(111) by Neyman and Rösch [114] also indicate binding at the threefold hollow site through the nitrogen atom. The general mechanism for adsorption is thought to be an interaction of the NO π-orbital and a backdonation of the surface electron density into the singly occupied NO π^*. This interaction can also be thought of as $NO^{(1-)}$ interaction with $M^{(+)}$ [112, 113].

3. *Adatoms and Intermediate Surface Fragments*

The backdonative interaction dominates the binding of adatoms such as C, O, or N to metal surfaces and drives these species to the high coordination sites. The greater degree of coordinative unsaturation of these adatoms is thus stabilized by forming bonds to a number of different metal surface atoms. Reactive surface intermediate fragments such as NH_x and CH_x which lie between adatom and stable gas-phase molecules in terms of degree of valence saturation, compromise between high and low coordination sites. The geometry of the adsorption site for partially dehydrogenated CH_x species and NH_x species is, to a significant extent, also determined by the backdonating interaction.

The LUMO of an atom such as C has a significantly lower energy than that of a molecule. In a molecule such as CO the carbon LUMO orbital is pushed upward in energy, because it corresponds to the antibonding component of the molecular interaction. This is depicted in Fig. 19. In other molecular fragments such as CH_2 or NH_2, this can lead to interesting consequences for the surface-chemical bond. For CH_2 (Fig. 20), the nonbonding $2p_x$-orbital on carbon has a lower energy than the antibonding C–H orbital fragments. The low energy of the $2p_x$ CH_2 LUMO then results in a strong interaction with the surface orbitals. Symmetry requires that the $2p_x$-orbital interact with an asymmetric surface group orbital. The CH_2 $2p_x$-orbital has a strong overlap with the asymmetric $(1/\sqrt{2 - 2S})\cdot[s(1) - s(2)]$ group orbital when CH_2 is adsorbed at a twofold site. As Table 7 shows, CH_2 prefers coordination to the Rh(111) surface in twofold coordination with the CH_2 bond perpendicular to the Rh–Rh bond. Yang and Whitten [79] also found a slight preference for CH_2 to be adsorbed twofold on Ni(111). The situation for NH_2 on Cu is quite similar, where NH_2 binds to the twofold coordination site with the H–N–H bond perpendicular to the Cu–Cu axis [76]. Returning to CH_2, the interaction with the d-valence electron band is significantly less for Ni than for Rh. The donating interaction is dominated by the interaction of the occupied CH_2, $sp^2(z)$-orbital with the metal s-p-

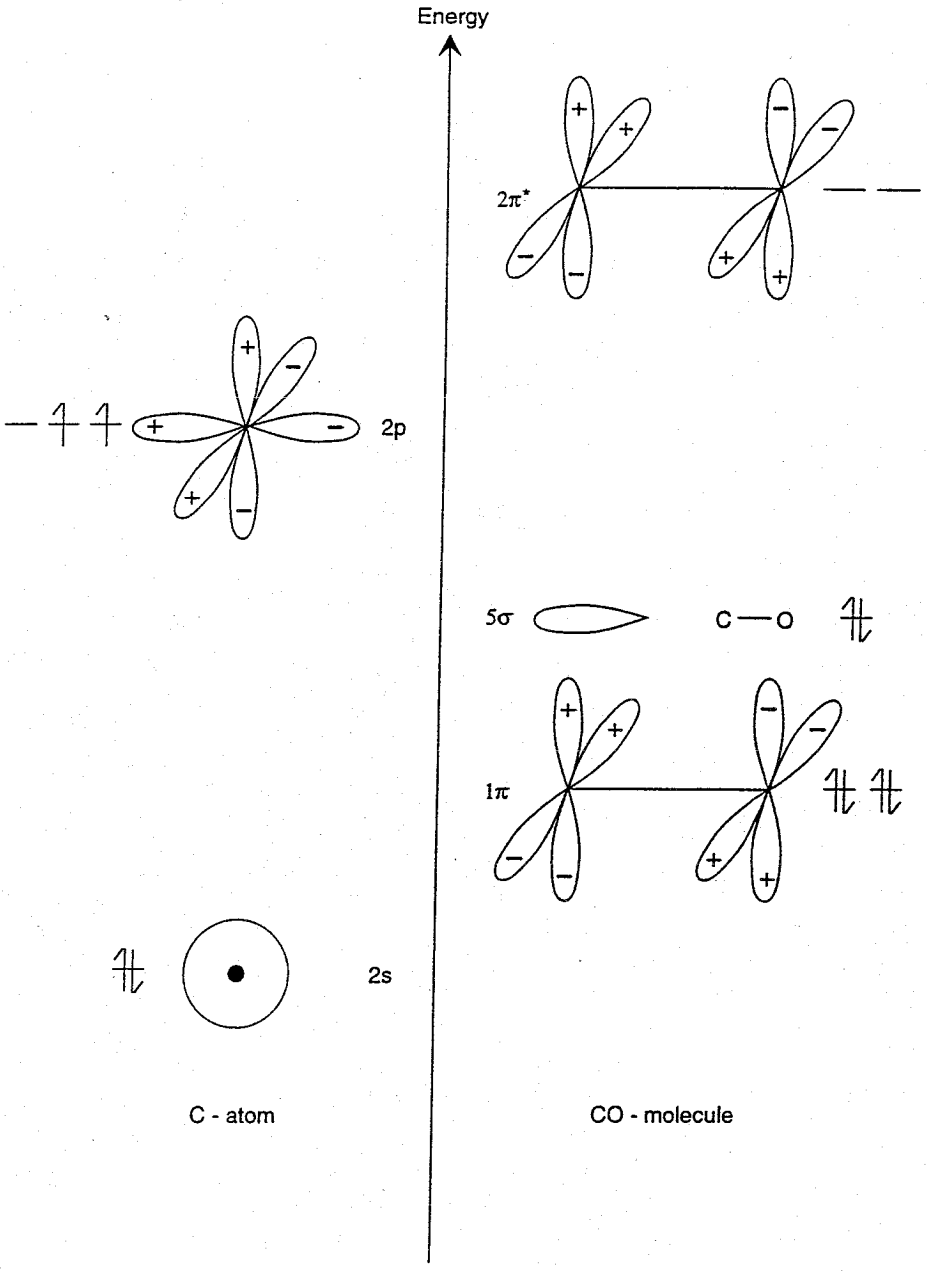

FIG. 19. Atomic and molecular valence electron levels of C and CO, respectively (schematic).

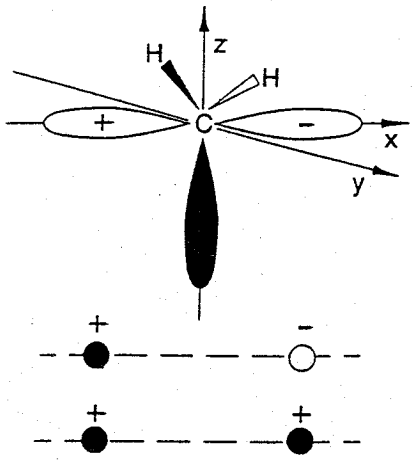

FIG. 20. Interaction of carbene with metal surface. The LUMO-2p atomic orbital of CH_2 interacts with asymmetric surface group orbital, the HOMO-$2p_z$ orbital of CH_2 interacts with a symmetric surface group orbital.

valence electrons, and now directs the CH_2 fragment to the threefold coordination site.

When the CH_2 fragment loses additional hydrogen to form either CH or C, two perpendicular partially filled $2p_x$ and $2p_y$ LUMO orbitals are generated on the carbon atom. Therefore, as can be observed in Table 7, the CH fragment and the carbon atom have a strong preference for bonding to the higher coordination site.

When bonding to metal surfaces with a high d-valence electron occupation is compared to that of metals with lower d-valence electron occupation, the strong increase in the adatom bond strengths of C, O, or N is attributed to two factors. First, the low energy of the 2p-orbitals results in the occupation of both bonding and antibonding adatom surface fragment orbitals. Reduction of the availability of d-valence electrons depletes the antibonding orbitals and strengthens the metal–adsorbate bond. Second, the work function of a metal decreases with decreasing d-valence electron occupation. This favors the backdonating interaction and also increases the adsorbate–metal bond energy. It is the latter effect that appears to dominate the observed trends.

D. Cluster Size Effects in Quantum-Chemical Calculations

As explicitly discussed in Secs. I.B.5 and II.B, the clusters chosen to model chemisorption on transition metal surfaces can be very important for the prediction of reliable energetics. Comparing the results of various models helps to define appropriate convergence criterion and the validity of various

TABLE 7

Interaction Energies of CH_x on a Rh(18,11) Cluster Modeling a (111) Surface [82]

Species	Site	E_{att}[a] (eV)	E_{rot}[b] (eV)	h_X[c] (Å)
H	1-fold	−4.91		1.6
	2-fold	−4.72		1.1
	3-fold fcc[d]	−4.58		1.0
	3-fold hcp	−4.51		1.0
C	1-fold	−6.49		1.8
	2-fold	−6.65		1.4
	3-fold fcc[d]	−8.08		1.2
	3-fold hcp	−8.19		1.2
CH	1-fold	−6.58		1.8
	2-fold	−6.92		1.4
	3-fold fcc[d]	−7.39		1.3
	3-fold hcp	−7.39		1.3
CH_2	1-fold	−4.61	0.05	1.9
	2-fold	−4.68	1.43	1.6
	3-fold fcc[d]	−4.19	0.11	1.5
	3-fold hcp	−4.18	0.11	1.5
CH_3	1-fold	−2.95	0.01	2.1
	2-fold	−2.14	0.02	1.9
	3-fold fcc[d]	−1.92	0.14	1.9
	3-fold hcp	−1.92	0.10	1.9

[a]Difference in maximum and minimum total energy during rotation.
[b]Height of adsorbing species (X=C, H or CH_x) above the surface.
[c]No Rh present in second layer.
[d]Rh present in second layer.

cluster models. In addition it helps to delineate the minimum size required to capture the appropriate electronic and structural features in deriving relevant chemisorption models. In the case of chemisorption, the answer will depend on the strength of the interaction. Adatom adsorption, such as O or C, on a transition metal is typically dominated by a strong attractive interaction and is typically in the range of 300–500 kJ/mol [2]. Molecular adsorption, on the other hand, is usually much weaker and of the order of 100 kJ/mol. The metal–metal bond energies between metal atom centers is typically of the order of 50 kJ/mol. Changes in the adsorbate environment will likely affect weakly bonded species much more than strongly bonded species. Hence the cluster size convergence criterion may be more critical for a weakly bound intermediates.

Because of the large overlap of adsorbate and metal–surface fragment orbitals in the chemisorbed state, chemisorption is not very sensitive to the

absolute value of the Fermi level or the local density of states at the Fermi level [2, 6a, 6b]. It is, however, a strong function of the width of the local density of states for the atoms involved in the chemisorption bond and the ionization potential and electron affinity of the cluster.

Whereas the local density for states (LDOS) for the d-valence electrons rapidly converges to bulk values with cluster size, the LDOS for the s- and p-valence electrons do not. This is attributed to the sparseness in their density. More accurate bond strength calculations would, therefore, dictate a more complete picture of the s and p states which would better simulate the metal surface. In the Models section (see Sec. I.B) we discussed a number of valuable proposals present in the literature aimed at enhancing convergence of the LDOS by increasing cluster size.

Here we analyze cluster size effects for two different situations using the results of DFT calculations. In the first system, we return to CO chemisorption and analyze the interaction of CO with different sized clusters of Co. We are concerned with modeling the proper balance between donating and backdonating interactions which is strongly dependent upon the coordination numbers of the cluster atoms. In the second system, we discuss the electrostatics of the potassium–rhodium bond and the effects of varying cluster size. We attempt to elucidate the proper description of electron transfer between adsorbate and metal surface.

E. The Interaction of CO with Co Clusters

The changes in the adsorption energy for CO adsorbed at different coordination sites are much smaller than the changes in binding energies for adatoms at different coordination sites. The relatively small changes for molecular adsorbates is attributed to a balance between the changes in the donating and backdonating interactions which occur in these systems. Moreover, the CO molecule often prefers adsorptive coordination atop at onefold surface sites. Corresponding adatoms, on the other hand, prefer to bind to highfold coordination sites at low surface coverages. The results discussed here are derived from cluster calculations for CO on Co_n and are aimed at analyzing the effect of cluster choice on the estimated adsorption energy.

Experimentally it has been shown that CO adsorbs onefold on the Co(111) surface and has an adsorption energy of the order of 150 kJ/mol [94]. The preference for atop coordination is largely due to the strong low coordination directing effect of the donating interaction of the CO 5σ to the Co d-atomic orbitals [61]. Two types of clusters were studied: clusters simulating the coordination on the transition metal surface configuration (Fig. 21), and clusters with a spherical geometry, similar to that of the 12 atoms surrounding a single "bulk" Co atom (Fig. 22). Table 8 summarizes

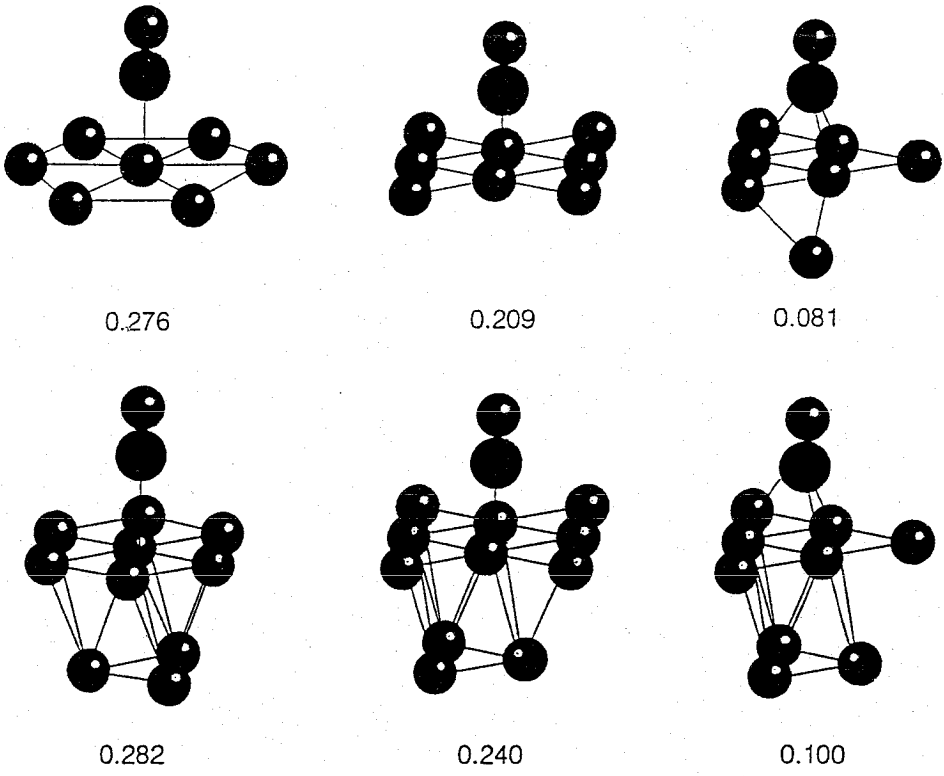

FIG. 21. C–Co bond order overlap population (P) for CO adsorbed to Co clusters [61, 94].

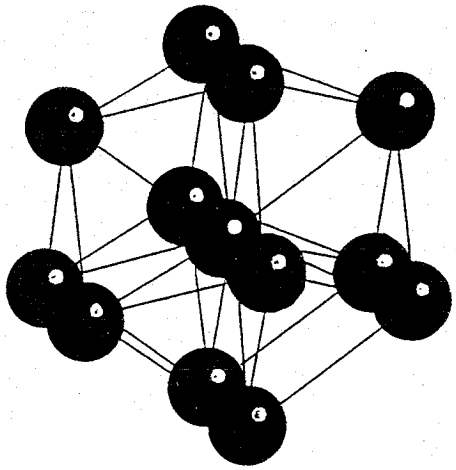

FIG. 22. Spherical ^{13}Co-atom cluster [61, 94].

TABLE 8

Comparison of CO Interaction Energies (kJ/mol) as a Function of CO Coordination Number Computed for Clusters of Fig. 21, with CO Interaction Energies Computed for Adsorption to the ^{13}Co Atom Cluster [61, 94] of Fig. 22

Cluster size	13	9–11	7–8
Onefold	−160	−200	−127
Twofold	−140	−263	−218
Threefold	−120	−241	−210

the computed interaction energies (in kilojoules/mole) for CO on each of these clusters.

The clusters on the first row of Fig. 21 contain 7–8 Co atoms, while those in the second row contain 9–11 Co atoms. Results from both sets of cluster calculations predict a strong CO–Co cluster interaction with a preference for the higher twofold and threefold coordination sites. This does not directly follow the experimental observations. As discussed later, this is primarily due to the improper description of the Co atoms at the edge of the cluster in the surface layer. This is attributed to the particular cluster used. CO chemisorbed to the spherical cluster depicted in Fig. 22, however, provides a better representation of the edge atoms and predicts the onefold coordination site of CO to be the preferred site.

The summed C–Co bond order orbital overlap population (P) is given below each cluster in Fig. 21. The overlap population is a measure of the isolated C–Co interaction which ignores changes in the Co–Co and C–O interaction which also occur upon chemisorption. In considering only the strength of the C–Co interaction (bond order overlap), the preference is for onefold coordination. In addition, preference is given for the nonspherical clusters. The very different preferences for CO adsorption and corresponding adsorption energies imply that there are changes in not only the adsorbate–surface bonding, but changes in the cluster bonding as well. The variation between clusters is due to the different responses of the cluster electrons to the disturbance with CO.

The clusters of Fig. 21 differ in two important ways from that of a real surface. On a real surface, the metal atoms have a lower coordination than those in the bulk. In the clusters depicted in Fig. 21, however, the Co atoms involved in the chemisorptive bonds actually have a greater number of Co neighbors than the Co atoms on the edge of the cluster. The number of Co atom neighbors for the cluster Co atoms is fewer than that in the bulk.

The clusters in Fig. 21, while informative, are not the optimal ones for studying the CO coordination problem. The Co atom coordination numbers of the Co atoms involved in the chemisorptive bond with CO vary with coordination of Co. As follows from bond order conservation (Sec.

I.B.2) or delocalization theory (Sec. II.A), the adsorbate–Co atom interaction is strongly affected by the metal atom's environment. The adsorbate–metal atom interaction will increase when the metal atom has low coordination (see also statement 4). The preference for twofold and threefold coordination over onefold coordination in the clusters of Fig. 21 can be directly related to these differences in cluster atom reactivity. Bond order conservation essentially indicates that the fewer the number of atoms that share a bond with the same atom, the stronger the corresponding metal–metal bonds.

This is illustrated in Table 9. One notes the considerably increased strength of the Co–Co interaction for atoms with a low coordination number. The higher values of the CO chemisorptive bond to the larger clusters in Fig. 21 are largely due to the weakened Co–Co bonds in the larger clusters.

In the clusters of Fig. 21, the lower coordination numbers of edge atoms compared to those at center atoms lead to an electron redistribution in which the center atoms have a lower d-electron atomic orbital occupancy than might be expected at the surface. This is different than the situation on a real metal surface where the narrowed d-bandwidth on the surface results in an increased d-atomic orbital electron occupation on the surface atoms compared to that on bulk atoms.

The electron distribution within the Co_{13} cluster depicted in Fig. 22, however, should provide a better representation of the surface. The outer Co atoms have lower coordination than those at the center. The result is a higher d-valence electron occupation on the outer atoms of the cluster in the spherical cluster of Fig. 21. This is responsible for the weaker adsorbate interactions than found for the Co_{9-11} clusters. The spherical Co_{13} cluster (Fig. 22) avoids the inconsistent surface orbital treatment and provides a better model to study CO–surface coordination modes. The chemisorption energy values are closer to the experimental values, and moreover, the chemisorption of CO is found to be atop. Both of which agree with the known experimental evidence [94].

The use of elliptic clusters, analogous to the spherical Co_{13} cluster used here, was originally pioneered by Goddard [4e]. He studied the chemisorption of hydrogen to the elliptic Ni cluster with a frozen d-valence electron band. Clearly there is a significant difference in the local coordination

TABLE 9

Average Co Metal–Metal Atom Bond Energy for Clusters Without CO Adsorbed (kJ/mol) [61, 94]

Bulk	13	10	7
71	100	111	140

of the outer cluster atoms of such clusters and dense surfaces. This gives rise to the small differences between computed interaction energy of CO on Co_{13} clusters and the experimental values found on single crystal surfaces.

A very strong indication for the validity of this statement derives from the recent results of Baerends et al. [92], who studied the chemisorption of CO on Cu slabs using their periodic DFT code [58]. On small clusters, CO preferred adsorption at the higher coordination sites with a stronger interaction energy. For extended slab calculations, however, te Velde and Baerends found a weaker interaction (~60 kJ/mol) with a preference for atop coordination, which is in good agreement with experiment. Both geometry optimization and nonlocal exchange-correlation corrections were essential in obtaining these results.

F. The Adsorption of Potassium to Rhodium

Potassium chemisorbs to a metal surface with an electron transfer from potassium to the metal surface leading to a K^+-M^--type of interaction. This is a direct consequence of the low potassium atom ionization potential. As shown schematically in Fig. 4, the positive charge generated on potassium is screened by the negative induced image charge on the lattice. The result is an electrostatic field along the surface which has been studied with theory and probed experimentally via photoemission of adsorbed noble gas atoms [115]. This agrees with well-established ideas from a series of previous calculations of charged cations on transition metal surfaces [116] and formal theory results by Norskov [63a].

Here we use nonlocal DFT calculation results to analyze the electrostatic field generated on rhodium clusters of varying size upon adsorption with potassium atoms [115a]. The clusters studied are shown in Fig. 23. Figure 24 present computed potential energy curves for each of these systems. Figure 24 also depicts the experimentally deduced electrostatic potential curves for Rh(111) surfaces with varying K coverages [115b]. One notes that on many of these clusters, potassium adsorption induces an electrostatic field that on the central surface metal atom has the opposite sign of that which was experimentally measured. This is especially true when the potassium is adsorbed at the edge of a cluster at a site of low coordination. The computed result is a consequence of electron conservation. Donation of electrons to Rh enhances the electron concentration on Rh. The rhodium atoms become slightly negatively charged. When the arrangement of Rh atoms in the cluster is such that the positive charge on potassium does not localize the excess electron charge on nearby rhodium atoms, the negative potential due to the rhodium atom charge will dominate the local electrostatic field and result in a positive potential. Only for large clusters, where the potassium atom becomes threefold or fourfold coordinated with Rh, do the nearest-neighbor surface atoms provide enough accommodating

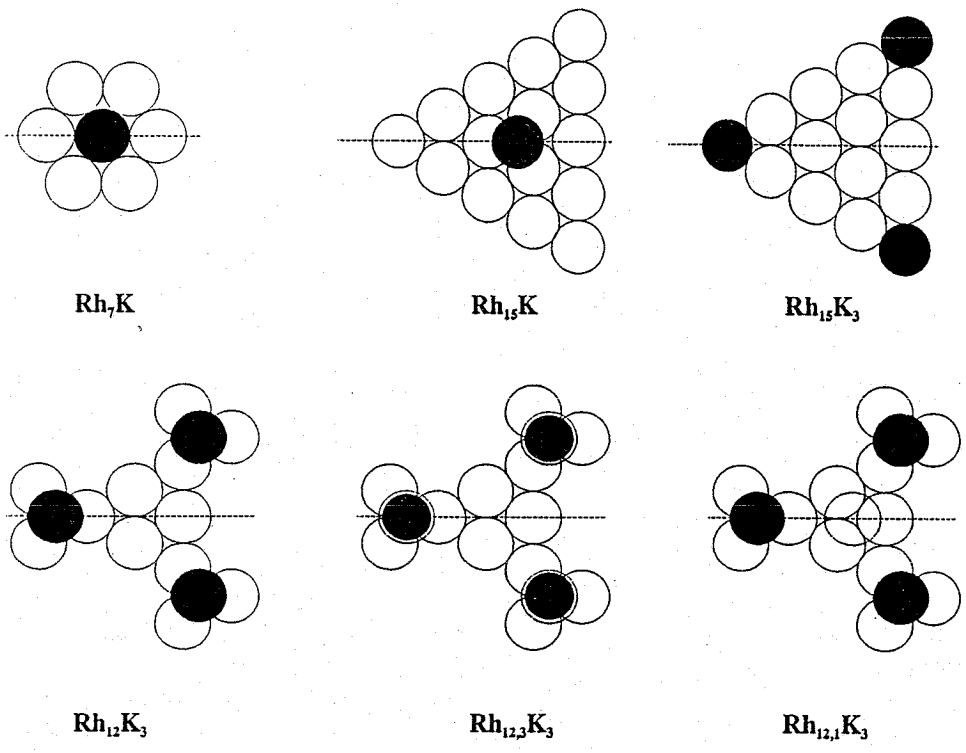

FIG. 23. The different K/Rh clusters used for Fig. 24 [115a].

empty orbitals to localize the negative charge near the positively charged adsorbed potassium atom. This then results in a negative potential at the center atom of the Rh cluster which agrees with the experimental results [115b].

For an infinite two-dimensional lattice, the electrostatic potential depends not only on the short-range interactions between neighboring atoms, but also on the long-range electrostatic interactions. The sum of these interactions result in the surface Madelung potential. The effect of the inclusion of these long-range interactions is shown in Fig. 24 ($Rh_{12,1}$ K_{3+} dipole). The negative potential at the center of the rhodium cluster is now enhanced. However, it still remains smaller than the experimentally determined potential. This is the combined effect of the larger effective potassium–rhodium surface ratio in the cluster and the cluster size effects discussed.

G. Surface Reconstruction

As mentioned several times already, the interaction between surface atoms and adsorbate leads to a weakening of the metal–metal atom bonds next to the metal atom involved in bonding with the adsorbate. According

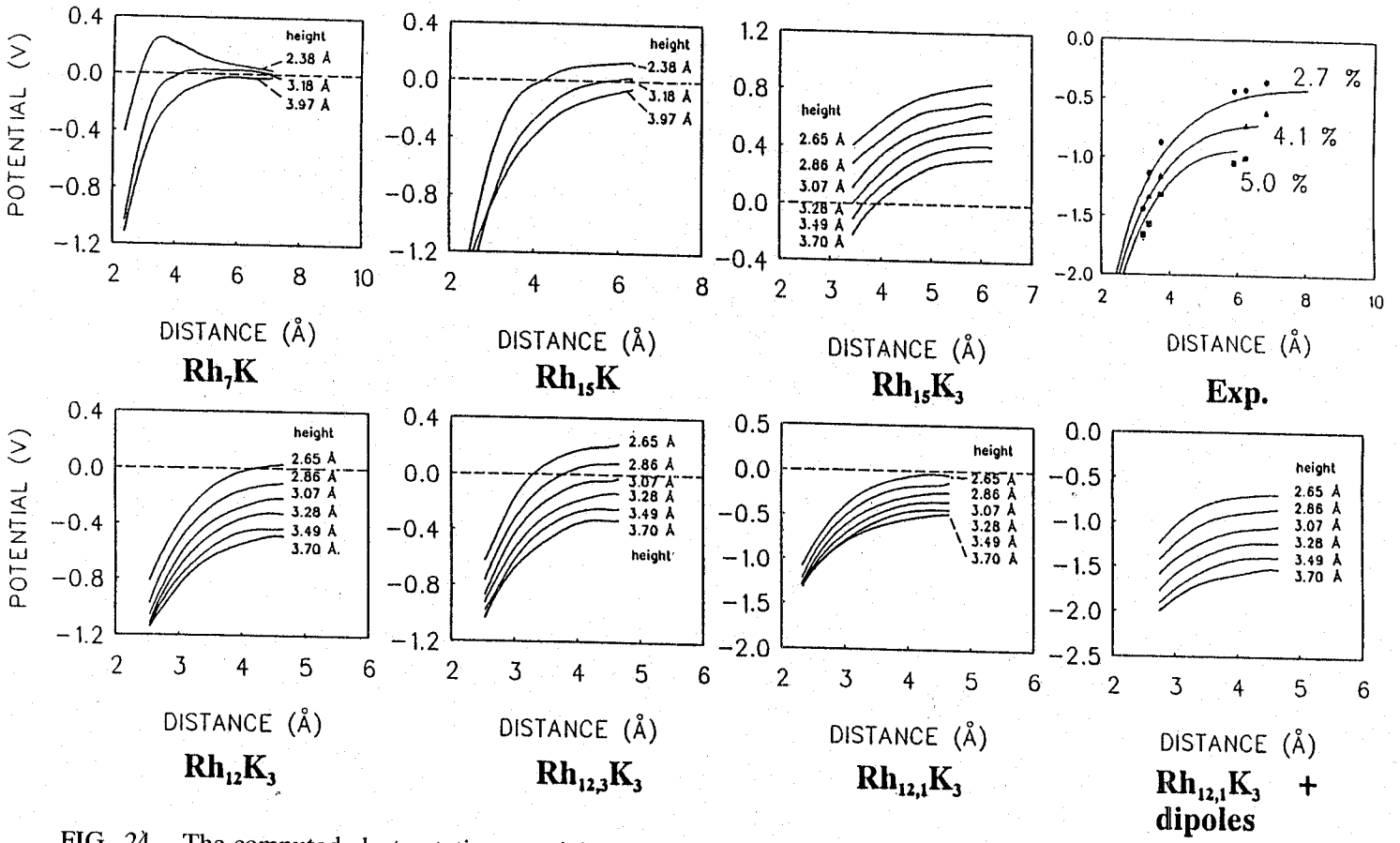

FIG. 24. The computed electrostatic potentials on the clusters of Fig. 21 [115a]. The experimental result for a surface with a varying K/Rh ratio (exp) has been added. The $Rh_{12,1}K_3^+$ dipoles result are the potential energy curves of the $Rh_{12,1}K_3$ cluster in the two-dimensional electrostatic field generated by the corresponding dipoles.

to this view, surface relaxation and reconstruction [117] are the consequence of alterations in the surface electronic interactions affected by chemisorption. A nice example of this is illustrated in recent cluster calculations by Neurock et al. [54], who allow for local relaxation of both the adsorbate and the cluster. All surface bonds which include the surface atoms involved in the adsorption complex become weaker. This is illustrated in both Figs. 25 and 26 for the adsorption of atomic hydrogen and oxygen on Pd_6 and Pd_{18} clusters. In Fig. 25, the three Pd–Pd bonds which make up the adsorption site (*Pd1–Pd3*, *Pd1–Pd6*, and *Pd3–Pd6*) elongate by 0.15–0.25 Å in the presence of oxygen and by 0.28–0.35 Å in the presence of atomic oxygen. They form strong Pd–H and Pd–O bonds as witnessed by the short Pd–H (1.77 Å) and Pd–O (2.07 Å) bonds. All cluster bonds involving the Pd atoms in the threefold adsorption site (*Pd1*, *Pd3*, *Pd6*) also become somewhat weaker as denoted by their bond elongation. For example, *Pd2–Pd6* elongates by nearly 0.1 Å in the presence of atomic hydrogen or oxygen. This same relaxation in metal–metal adsorption-complex bonds is also noted

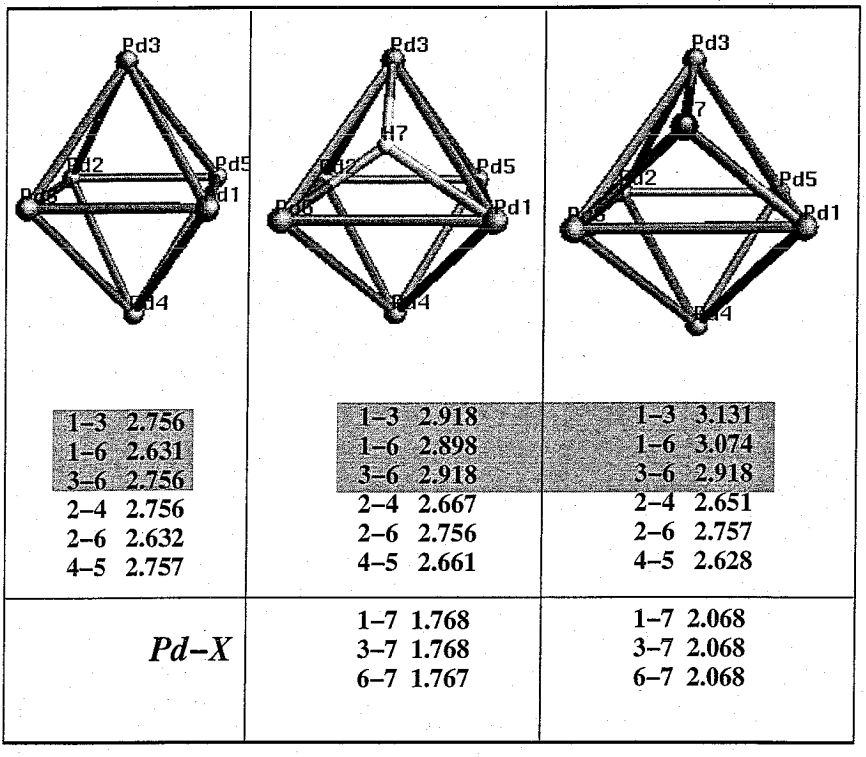

	1–3 2.756 1–6 2.631 3–6 2.756 2–4 2.756 2–6 2.632 4–5 2.757	1–3 2.918 1–6 2.898 3–6 2.918 2–4 2.667 2–6 2.756 4–5 2.661	1–3 3.131 1–6 3.074 3–6 2.918 2–4 2.651 2–6 2.757 4–5 2.628
Pd–X		1–7 1.768 3–7 1.768 6–7 1.767	1–7 2.068 3–7 2.068 6–7 2.068

Primary effects (local)

FIG. 25. Density functional optimized Pd_6 cluster calculations and adsorbate-induced cluster reconstruction in the presence of atomic hydrogen and atomic oxygen [54]. All distances are in angstroms.

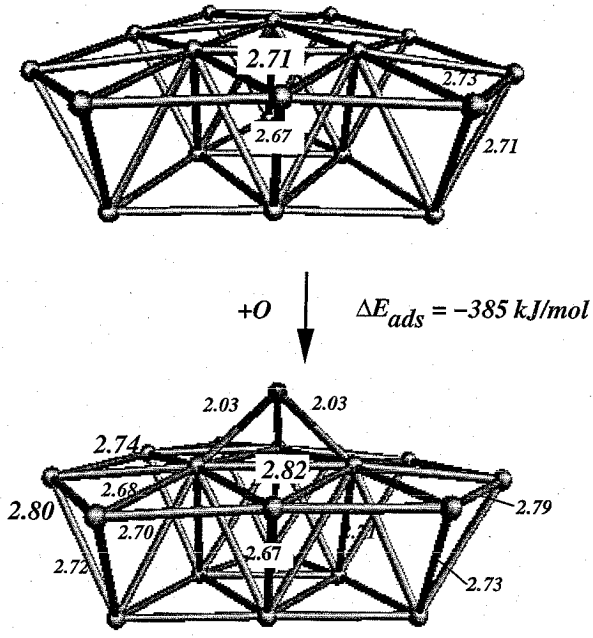

	Pd_{18}	$Pd_{18}O$
Pd–Pd	*2.71*	*2.82*
Pd–Pd next nearest	*2.73*	*2.68*

Pd(ads) pulled up by ~0.09 Å from surface
Pd–Pd Elongated by 0.1 Å

FIG. 26. An extended Pd_{18} cluster model of the Pd(111) surface. Fully relaxed geometry optimization of the initial Pd_{18} cluster and the Pd_{18}–O adsorbate/surface complex [54]. All distances are in angstroms.

for much larger clusters which more appropriately simulate the extended surface. This was demonstrated by allowing a Pd_{18} atom cluster to optimize in the presence of atomic oxygen. The results are depicted in Fig. 26. The Pd–Pd bonds involved in the adsorption complex relax by about 0.1 Å and do so by pulling up away from the surface by about 0.09 Å. The relaxation changes on the Pd_{18} cluster are smaller than those over the Pd_6 cluster. This is attributed to influence of the extended lattice (for Pd_{18}) that acts to restrict movement.

The results in Fig. 25 demonstrate that atomic oxygen more strongly perturbs the palladium cluster. This agrees with simple thermodynamic arguments that the Pd–O bond is substantially stronger then the Pd–Pd or Pd–H bonds and will likely lead to changes in local Pd–Pd bond lengths.

In both Figs. 25 and 26 it is interesting to note that the next-nearest

adsorbate neighbor Pd–Pd bonds, those which are one bond away from the adsorption site, are subsequently strengthened. The *Pd2–Pd4* bond in Fig. 25, for example, is shortened by nearly 0.1 Å. This nicely illustrates the consequence of bond order conservation.

The surface relaxation results depicted in Fig. 26 are consistent with the experimental results by Van Hove and Somorjai [118] for an analogous system of ethylidine on platinum. Both demonstrate how the surface atoms in the adsorption complex are pulled up out of the surface and next-nearest neighbors relax into the bulk. Both calculation and experiment show changes on the order of about 0.1 Å. Adsorption energy differences for rigid versus relaxed surfaces (determined through the calculations) are on the order of about 20 kJ/mol.

In the absence of rigorous structural optimizations, bond order population analysis provides a useful implicit measure of bond strength and bond weakening for adsorption on fixed metal clusters. We illustrate this in the next section for the Cu–NH_3–O system. The consequence of this weakening of the metal bonds next to the surface complex is a change of the bond angles and distances in the adsorption complex. The geometry of the adsorption complex, defined as the adsorbate plus next-nearest-neighbor metal atoms, is typically very similar to that of organometallic cluster analogs. This is notwithstanding the very different heats of formation due to the cost of reorganization of the surface electrons. On surfaces, the altered metal–metal bond strengths will lead to adsorbate-induced reconstruction effects [117]. We limit our discussion in this review to the short-range interactions that control the interaction of chemical reaction intermediates and consider the geometry of the adsorption site as determined by the geometry of the surface.

H. Coadsorbate Interactions on Cu Clusters

As part of a study on the oxidation of NH_3 by Cu, we have investigated the interaction between coadsorbates on a Cu(8,3) cluster. Three specific interaction cases were explored [76b]. Each of them are sketched in Fig. 27. The results were obtained from density functional calculations in which the adsorbate geometry and height of the adsorbate to the surface were optimized, while fixing the geometry of the atoms in the Cu cluster to their bulk Cu–Cu distances of 2.556 Å. Bond order conservation principles were found to be quite useful in rationalizing the structural and energetic changes which accompanied each of the different lateral surface interactions.

Atomic oxygen (O) and nitrogen (N), molecular O_2 (perpendicular, see Sec. III.E), and OH and NH fragments were all found to bind to threefold coordination sites. NH_3 and H_2O were both onefold coordinated, and NH_2 was found to bind to twofold coordination sites. Case I is a situation where both adsorbates prefer threefold coordination sites and share two

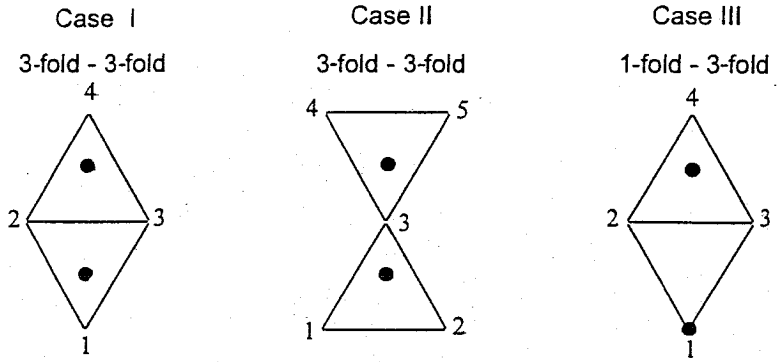

Species	Case I	Case II	Case III
NH_3 on Cu(8,3)-O	-	-	-32
NH_3 on Cu(8,3)-O	-	-	-17
NH_2 on Cu(8,3)-OH	-	-	-5
NH on Cu(8,3)-O	211	25	-
N on Cu(8,3)-O		30	-
N on Cu(8,3)-OH	170	29	-

Oxygen and hydroxyl are always threefold coordinated

FIG. 27. Lateral interaction between adsorbate on a Cu cluster as a function of adsorption geometry (units: kJ/mol) [76b].

metal atom neighbors. For all case I examples given in Fig. 27, there is large repulsive interaction between the adsorbates which arises from the sharing of adsorbate bonds with two metal surface atoms. This repulsive interaction is significantly reduced when only one surface atom is shared (case II). The interaction actually becomes an attractive one when no surface atoms are shared, but neighboring Cu atoms are involved in bonding. These results are consistent with predictions from bond order conservation. When surface atoms become involved in a chemisorptive bond, the number of surface atom neighbors increases and hence the metal–metal bonds directly connected with the surface adsorption complex weaken.

This can easily be demonstrated through bond order overlap population results. Table 10 lists the Cu–N and Cu–Cu bond order overlap populations for the case III example for NH_3 and O on Cu(111) for both before and after adsorption of the oxygen atom [119]. The Cu–Cu bond order overlap population decreases for bonds *Cu1–Cu2* and *Cu1–Cu3* when oxygen is coadsorbed. This decrease in bond orbital overlap is directly tied to a weakening in the Cu–Cu bond strength and subsequently strengthens the Cu–N interaction. The weakening of the Cu–Cu bond follows from the increase in the number of Cu atom neighbors. The weakened Cu–Cu

TABLE 10
Bond Order Overlap Population Between Atoms Along the Chain $[O^-]Cu-Cu+N$ [76]

	Copper with:		
	Nitrogen	Copper	Oxygen
Without oxygen	0.0785	0.0419	—
With oxygen	0.0896	0.0375	0.1110

interaction results in a redistribution of the bonding valency and a strengthening of the other connecting bonds, including the Cu–N interaction. One concludes that the short-range lateral interactions that can ultimately lead to island formation or formation of ordered overlayers are, to a significant extent, due to the changes in the surface electron distribution in the presence of coadsorbed surface species.

III. QUANTUM CHEMISTRY OF SURFACE REACTIONS

The preceding concepts and quantum-chemical principles which govern the nature of the surface–chemical bond and control adsorption are now extended to understanding the reactivity of molecular and fragment surface species. A prototype surface–chemical reaction is dissociative adsorption. This is often a rate-limiting step in different catalytic reaction cycles. In Sec. III.A we discuss the dissociation of diatomic molecules such as CO and NO. In order to compute overall reaction rates, reaction rate constants for each of the elementary reaction steps which constitute the overall catalytic reaction cycle must first be determined. Transition state reaction rate theory can be applied provided the transition state and its vibration–rotation frequency spectrum are known. First-principle quantum-chemical calculations can effectively be used to predict the transition state of surface–chemical reactions. This is subsequently used to compute partition functions, Arrhenius $\log_{10}A$ factors, and elementary rate constants. We illustrate this for the dissociation reactions of CO and NO, as well as for methane.

The prediction of overall catalytic reaction cycles requires the detailed computation of overall reaction energies of each elementary step in the cycle. In addition, the kinetics for each individual step in the overall cycle are required to make an *ab initio* prediction of the overall rate constant. For the oxidation of ammonia catalyzed by Cu, the energy changes for the pathways associated with complete reaction cycles have been calculated from a set of nonlocal DFT calculations. The results for different reaction mechanisms are presented in terms of overall reaction energy diagrams and used to help discriminate between possible mechanisms. We illustrate the

role of quantum chemistry in the estimation of measurable reaction orders and selectivity. This is ultimately tied to the likelihood as to whether oxidation of NH_3 occurs via H-abstraction from adsorbed atomic or molecular oxygen.

Other essential surface reaction paths in a general overall catalytic cycle include insertion and association reactions. In the epoxidation of ethylene, for example, significantly high surface coverages of oxygen are required to maintain selectivity toward the insertion route. This system is analyzed here to illustrate essential features governing the insertion mechanism on transition metal surfaces. Product formation usually occurs through associative surface reactions that require low temperatures to compete with nonselective dissociation routes. The carbon–carbon bond formation reaction that occurs in the Fischer–Tropsch reaction was chosen to discuss pathway selectivity issues whereby the optimal conditions for dissociative adsorption and desorption compete with those for the desired associative chain growth reaction.

A. The Dissociation of CO and NO

CO and NO are known to adsorb in perpendicular or slightly bent configurations on various noble metal surfaces. Due to the enhanced partial electron occupation of the antibonding orbital of NO over CO, the N–O bond in the adsorbed surface complex is weaker than that of the analogous C–O bond and hence will dissociate more readily. We focus the discussion here on the dissociation reaction of CO. Most of the details for CO dissociation are also valid for NO dissociation. Using the methanation reaction, we have demonstrated experimentally [120] that the rate of CO dissociation has the following general form:

$$r = k_{\text{diss}}\theta(1 - \theta)^x \tag{17}$$

The rate goes through a maximum with CO coverage, θ. This indicates that for the surface dissociation reaction to occur, empty surface sites next to the adsorbed molecule are required. In order to postulate a plausible mechanism for this reaction, it is necessary to first analyze both the initial and final states of the reaction. In the present example, these correspond to the associative molecular state (reactants) and surface adatoms (dissociation products). While molecules adsorbed to a metal surface show only small differences in energy when their coordination number changes, atoms on the other hand, are (except hydrogen, which has no accessible 2p-atomic orbitals) much more sensitive to adsorption site changes and prefer the higher coordination sites (see Sec. II.D). This implies that a dissociating molecule requires an ensemble of surface atoms to accommodate both the lower coordination adsorption site and the higher coordination adatom sites of the products. This is illustrated in Figs. 28 and 29. On a (111) face-

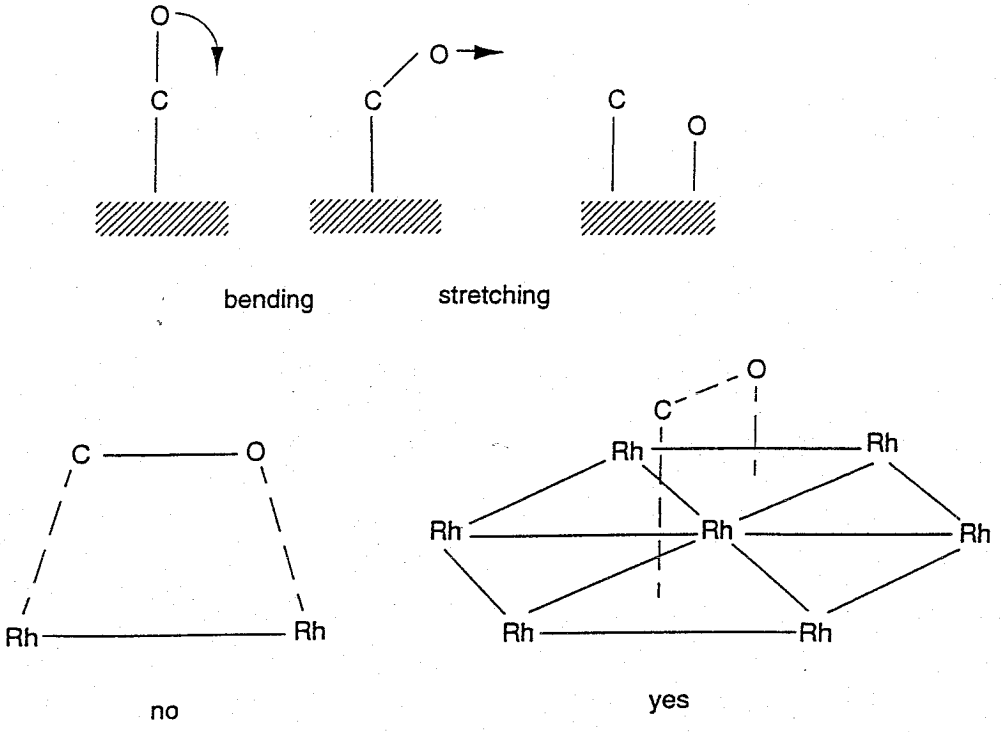

FIG. 28. Dissociation of CO. The allowed and a nonallowed dissociation path. In order to dissociate, the CO molecule has to bend and stretch as indicated in the top three sections (schematic).

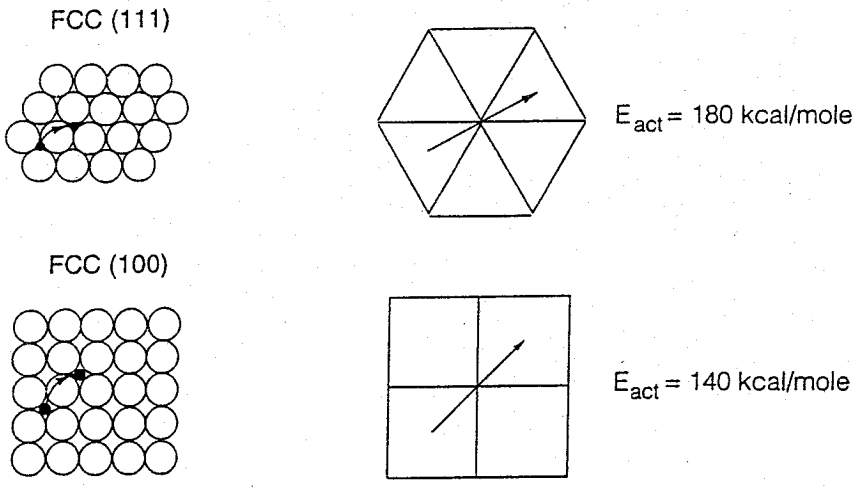

FIG. 29. Minimum dissociation energy paths of CO on large clusters of Rh according to the ASED method. The activation energy on the (111) surface is predicted to be 8 kcal mol^{-1} higher than on the (100) surface (1 ≈ 4.184 J) [146].

centered-cubic metal the dissociation of CO molecule requires at least an ensemble of 4 or 5 surface atoms. This is the basis of the so-called ensemble effect in heterogeneous catalysis [121].

As explained in Sec. II.H, adatoms that share surface atoms experience a repulsive interaction. Hence, thermodynamics prescribes a final state where the adatoms or adsorbates share the smallest number of surface atoms. This is known as the principle or minimum atom sharing [61]. On the (111) surface the preferred final state of the dissociated molecule would be the 5-atom surface ensemble shown in Fig. 28. The energy change of the surface dissociation reaction depends on the difference in energy of adsorbed molecule CO and that of the adsorbed atoms generated upon dissociation. Adatoms are much more sensitive to changes in surface topology and changes in the composition of transition metal surface than molecular species are. This sensitivity is directly tied to the more dramatic changes of adsorption energies for adatoms over molecules.

Figure 28 illustrates the lowest energy dissociation path computed for CO on clusters simulating the Rh(111) and Rh(100) surface. Calculations were performed using the semiempirical ASED method [25], and extended Hückel approach which explicitly includes repulsive potentials between the atoms. Specific accounting of these repulsive potentials leads to better estimated geometries and energetics and allows for the calculation of very large clusters. Note that the reaction path requires crossing of the C–O bond over the metal atom that connects the final sites of the product atoms. Essentially, this is a bending of the surface C–O angle coupled with the C–O stretch. The reaction path is not only determined by the energies of the initial and final state but also controlled by the electronic interactions that weaken the dissociating bond. The CO molecule bends until a strong enough interaction between the O atom and the surface–metal atoms develops. The C–O bond then begins to stretch (see Fig. 28). This bond is weakened by electron backdonation of electrons into its molecular antibonding orbitals. These are the LUMOs of CO, the $2\pi^*$-orbitals. Their interaction with surface requires proper symmetry of the surface group orbitals. The transition states of the two reaction paths that often compete are sketched in Fig. 28. When CO crosses atop over a surface atom (as found for Rh, Figs. 28 and 29), the activation of the $2\pi^*$-orbitals of CO is due to interaction with the surface d_{xz}- and d_{xy}-orbitals. The d_{xz}-orbitals are directed toward the $2\pi_z^*$-orbital and result in a large overlap. The other $2\pi_y^*$-orbital has a smaller overlap with the d_{xz} [Fig. 30(a)]. The interaction of the $2\pi_y^*$-orbital and metal surface can be increased, when the CO molecule crosses the surface metal–metal bond [Fig. 30(b)]. This occurs, however, at the expense of the favorable overlap of the $2\pi_z^*$–d_{xz} interaction from the atop adsorption configuration. On the (111) surface, NO dissociation is favored over the top of a single metal center, whereas on the more open (100) surface, NO dissociation proceeds across a metal–metal

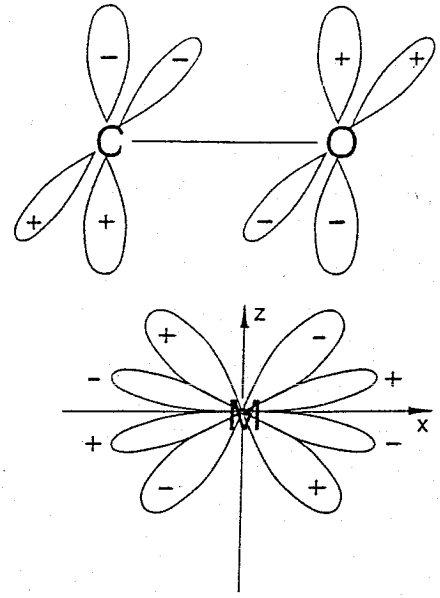

(a)

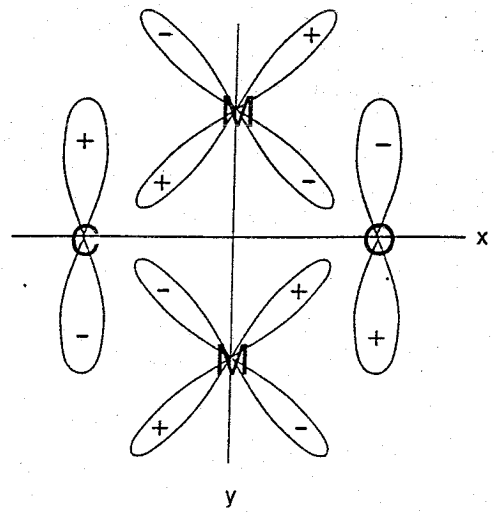

(b)

FIG. 30. Comparison of the $2\pi^*$-electronic interaction in transition states for CO dissociating by movement over a metal atom (a), and dissociating over a metal–metal bond (b).

bond [111]. This bond-crossing model also predicts a considerably high activation [122] for O_2 adsorbed to Ag. In these cases, orbital symmetry requirements overrule the energetics of the principle of minimum atom surface sharing, and drive the path over the metal–metal bond. Figure 29 illustrates the higher reactivity of an open surface compared to the denser surface. The metal surface atoms of the open surface have fewer surface atom neighbors than those in a dense surface. According to bond order conservation, this results in stronger surface bonds with adsorbing atoms. The change in energy is larger for adatoms than for molecules, due to the redistribution of the electron valency of the carbon atom in forming the molecular bond [see Eqs. (6) and (7)]. The larger energy change for the adatoms results in a thermodynamically more favored dissociation. According to Brønsted–Polanyi relation, as long as the reaction mechanism is unchanged the change in activation energy is proportional to that of the reaction energy. For dissociation reactions, the proportionality constant is approximately half.

$$\Delta E_{\text{act}} \approx \frac{1}{2} \Delta E_{\text{r}} \tag{18}$$

We explore how changes in the electronic structure of specific transition metals affect the surface dissociation energetics through a series of ASED calculations. Figure 31 compares the computed dissociation energetics for CO on the (111) surfaces of Pd, Rh, and Ru [82]. The metal parameters have been held fixed, and only the number of electrons per

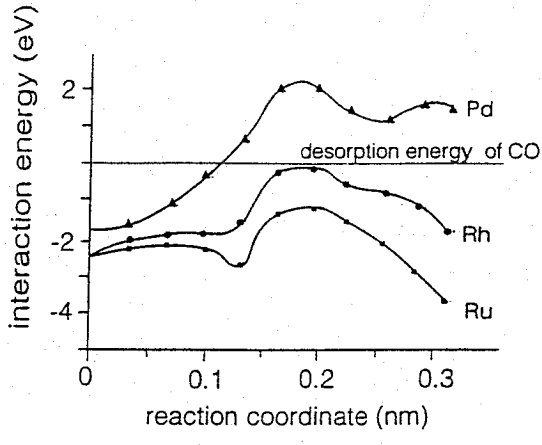

FIG. 31. Change in ASED interaction energy of a dissociating CO molecule on the Rh(111) surface. The recation coordinate is the projection of the CO distance on the surface. The calculations have been done for the minimum reaction energy path as determined for Rh [146]. ▲ denotes results for the same cluster with 1 electron per metal added (Pd). ● denotes results for the cluster with 1 electron per metal subtracted (Ru).

metal atom is varied. For Pd, one has 10 valence electrons, for Rh there are 9 electrons, and for Ru there are 8 electrons per atom. The number of s,p-valence electrons per atom is approximately 1 for each of the three metals while the d-valence electron number changes from 9 to 7 electrons per atom for each of these metals.

The reaction coordinate is represented by the projection of the CO axis onto the metal surface. Initially the reaction coordinate is at zero, where the CO binds perpendicular to the surface at a threefold coordination site. As the reaction proceeds, the CO molecule begins to bend with respect to the surface normal vector. This is followed by the C–O bond stretch. When the C–O distance is approximately 3.0 Å, the C-atom and O-atom are nearly completely separated.

Note the large differences in adatom binding energies on the different metal surfaces and the relatively small differences in energy for the adsorbed CO molecule. The changes in both donating and backdonating interactions tend to compensate for one another for molecular adsorbates on metal surfaces and, therefore, result in smaller observed variations. A depletion of the d-valence electron band which results as one moves from Pd to Rh to Ru, leads to an overall stronger interaction energy. Again because of the large changes of adatom energies compared to admolecule energies, the corresponding metal surfaces become more reactive for dissociative adsorption.

The activation energy for C–O dissociation on Rh(111), depicted in Fig. 31, was found to be comparable to that of desorption. As discussed in the next section, this leads to a faster rate of desorption than dissociation. This is due to the favorable entropic changes which accompany desorption. As one moves to right of Rh to Pd, the desorption of CO is found to be considerably lower than that for dissociation. In moving to the left to Ru, the barrier for dissociation becomes substantially lower than that for desorption.

Generally, the activation energy for dissociation of an adsorbed molecule is of the order of 10% of that of the dissociation energy. The action of a catalyst, to a significant extent, derives from to this feature. Reactions strongly endothermic in the gas phase can become exothermic when occurring on a metal surface and have a relatively low activation energy. This is the result of stabilization of the product fragments by adsorption to the metal surface.

B. Transition State Reaction Rate Theory for the Dissociation and Desorption of Diatomic Molecules

The transition state theory reaction rate constant expression k_r is [123]:

$$k_r = \frac{kT(p.f.)^{\#}}{h(p.f.)^0} e^{\frac{-E_b - E_0}{kT}} \tag{19}$$

where k is Boltzmann's constant, h is Planck's constant, T is the temperature, and $E_b - E_0$ is the transition state barrier energy that has to be overcome. $(p.f.)^{\#}$ is the partition function of the transition state with the exclusion of the contribution due to the reaction coordinate, and $(p.f.)^0$ is the partition function of the initial state. We use expression (19) to analyze differences between rates of dissociation and desorption. It has been observed experimentally [124] that the preexponent of the desorption reaction rate constant is often three to four orders of magnitude larger than that for dissociation. The preexponent of reaction rate constant in Eq. (19) can be defined as:

$$\nu_{\text{eff}} = \frac{kT(p.f.)^{\#}}{h(p.f.)^0} \tag{20}$$

The ratio R of the preexponents for the desorption and dissociation reaction rate constants is then given by:

$$R = \frac{(p.f.)^{\#}_{\text{des}}}{(p.f.)^{\#}_{\text{diss}}} \tag{21}$$

R is the ratio of partition functions for the transition states of desorption and that of dissociation, respectively. One can distinguish between two extremes for a transition state: the loose transition state and the tight transition state. They are sketched schematically in Fig. 32 for the CO–metal

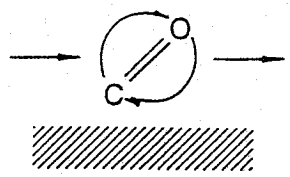

loose transition state

(a)

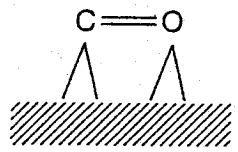

tight transition state

(b)

FIG. 32. Loose (a) and tight (b) transition state (schematic). In the loose transition state, CO has rotational and translational freedom in two dimensions.

system. In the loose transition state, the intermediate is considered to be mobile and nearly freely rotating. In the tight transition state, the intermediate is more tightly bound and, therefore, much more rigid.

Partition functions can often be simplified and written as the product of: (1) the two-dimensional partition function for translational motion parallel to the surface, (2) the partition function corresponding to the vibrational motion of the molecule, and (3) the partition function corresponding to rotational motion.

$$p.f. = (p.f.)_{\text{trans}}(p.f.)_{\text{vibr}}(p.f.)_{\text{rot}} \tag{22}$$

A loose transition state for a diatomic molecule with complete translational and rotational degrees of freedom, yet adsorbed on a metal surface, has a transition state partition function of:

$$(p.f.)^{\#}_{\text{loose}} \approx 10^4 \tag{23a}$$

Whereas for a tight transition state with frozen motion, the $(p.f.)^{\#}$ becomes:

$$(p.f.)^{\#}_{\text{tight}} \approx 1 \tag{23b}$$

Comparing the two leads to an approximate maximum bound value for R at 10^4. The large difference in reaction rate constants for desorption and dissociation for surface reactions with comparable activation energies for desorption and dissociation is due to the very different corresponding transition states. The transition state for desorption is typically a highly mobile state, whereas that for dissociation is much more rigid. For NO and CO, this is confirmed by quantum-chemical calculations. Figure 33 shows the predicted geometry for NO dissociation [34] computed on the Cu_{11} cluster model using nonlocal DFT calculations [76b, 111] discussed earlier. The result is very similar to that found earlier for CO on Rh using semiempirical calculations.

The level of calculation indicates that the results in Fig. 33 should be fairly reliable in terms of the geometries of the initial state, transition state, and final states. The geometry of the transition state in this system is quite similar to that of the final dissociated state. The bent NO bond has stretched considerably where the nitrogen atom distance to the surface is similar to that corresponding to the final dissociated state. The oxygen atom distance to the surface is also quite close to that found in the final state. This implies that the NO fragment has a limited mobility in its transition state and is likely a tight transition state. Table 11 lists computed preexponential values of CO and NO based on transition state density functional calculations [111]. Calculations have been done on clusters simulating the (111) and (100) surfaces of Cu. The computed preexponential values listed in Table 11, 10^{11}–10^{13}, are consistent with the tight nature of the transition states for dissociation of CO and NO.

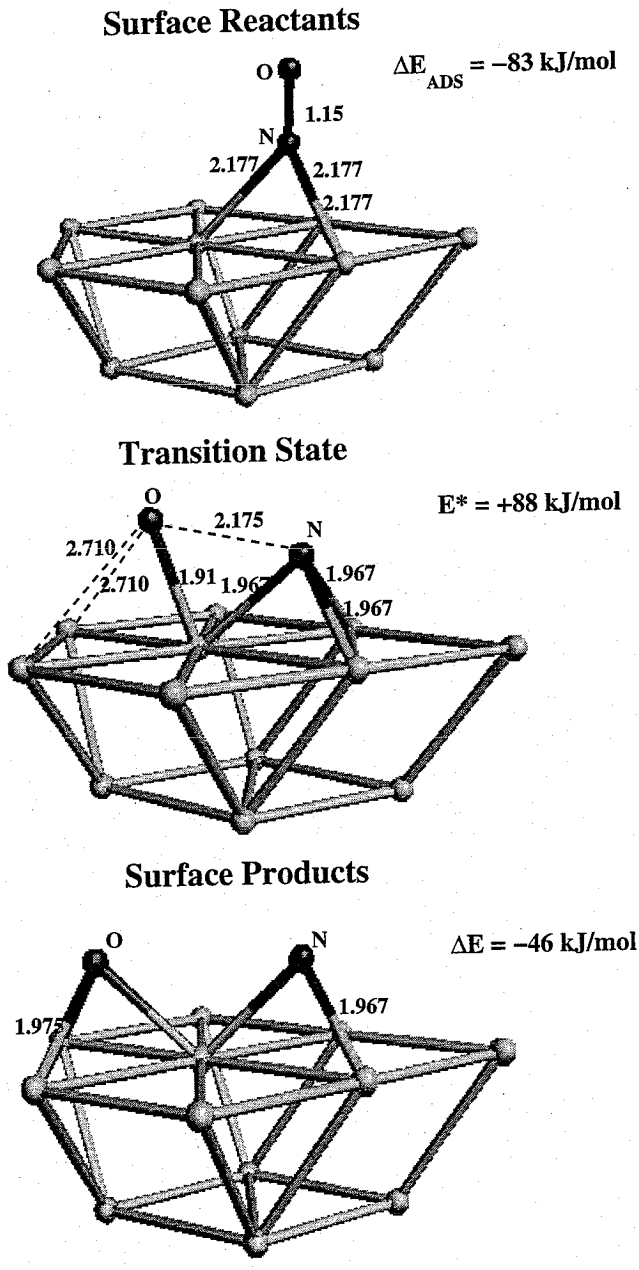

FIG. 33. Predicted transition state for NO dissociation on Cu. A comparison with the molecular and dissociated states [76b]. The numbers denote bond length in angstroms.

TABLE 11

Preexponential Factors ν_{eff} for CO and NO Dissociation [111]

	Cluster	Surface	ν_{eff} (sec^{-1})
CO	Cu_{10}	(111)	$4.8-10^{11}$
	Cu_{13}	(100)	$1.9-10^{13}$
NO	Cu_{13}	(100)	$5.3-10^{12}$

C. *The Rate of Dissociative Adsorption of Methane*

Ab initio studies on Ni clusters by Blomberg and Siegbahn [52] demonstrated very clearly that a low activation energy for methane dissociation requires a strong interaction between the dissociating C–H bond and the metal d-valence atomic orbitals. Dissociation occurs by stretching the C–H bond over the top of a nickel atom center.

The results of DFT calculations for the transition state of the oxidative addition of CH_4 on Ni atom center to form $HNiCH_3$ and over a Ni_7 cluster are shown in Fig. 34. The computed rate constants for oxidative addition of CH_4 and reductive elimination on the single Ni atom center are [125]:

$$k_{add} = 7.62 \times 10^7 \, e^{-\left\{\frac{36(kJ)}{kT}\right\}} \quad (s^{-1}) \tag{24a}$$

$$k_{red\ elim} = 1.16 \times 10^{13} \, e^{-\left\{\frac{73(kJ)}{kT}\right\}} \quad (m^3\ mol^{-1}\ s^{-1}) \tag{24b}$$

The preexponent for the rate of oxidative addition (10^7) is similar to that of the rate of hard-sphere collisions. This high preexponent for reaction is largely due to the rotational freedom of the methyl group in the transition state and the relative low frequencies of the transition state vibrational modes. The preexponent has already been corrected for quantum-mechanical tunneling. This enhanced the rate by a factor ~1.4. The preexponential factors for the rate constant of CH_4 to a Ni-atom and a Ni_7 cluster were found to be very similar. The sticking coefficient is the ratio of the rate of dissociative adsorption divided by the number of molecular collisions with the metal surface. The computed preexponent of this reaction is 1/10th that of the hard-sphere collision rate. Therefore, the transition state for methane dissociation is considered a loose transition state. The activation energy of the reaction arises from the need to stretch the C–H bond. The methyl group, therefore, becomes stabilized by the contact of the C-atom with the metal center. The activation energy of the reaction depends to a significant extent on the backdonation of electrons into the antibonding orbital of the stretching C–H bond. As the C–H bond stretches, the unoccupied C–H antibonding orbital is lowered in energy. This enhances the efficiency of backdonation. As expected the interaction of CH_4 with a Ni atom embedded

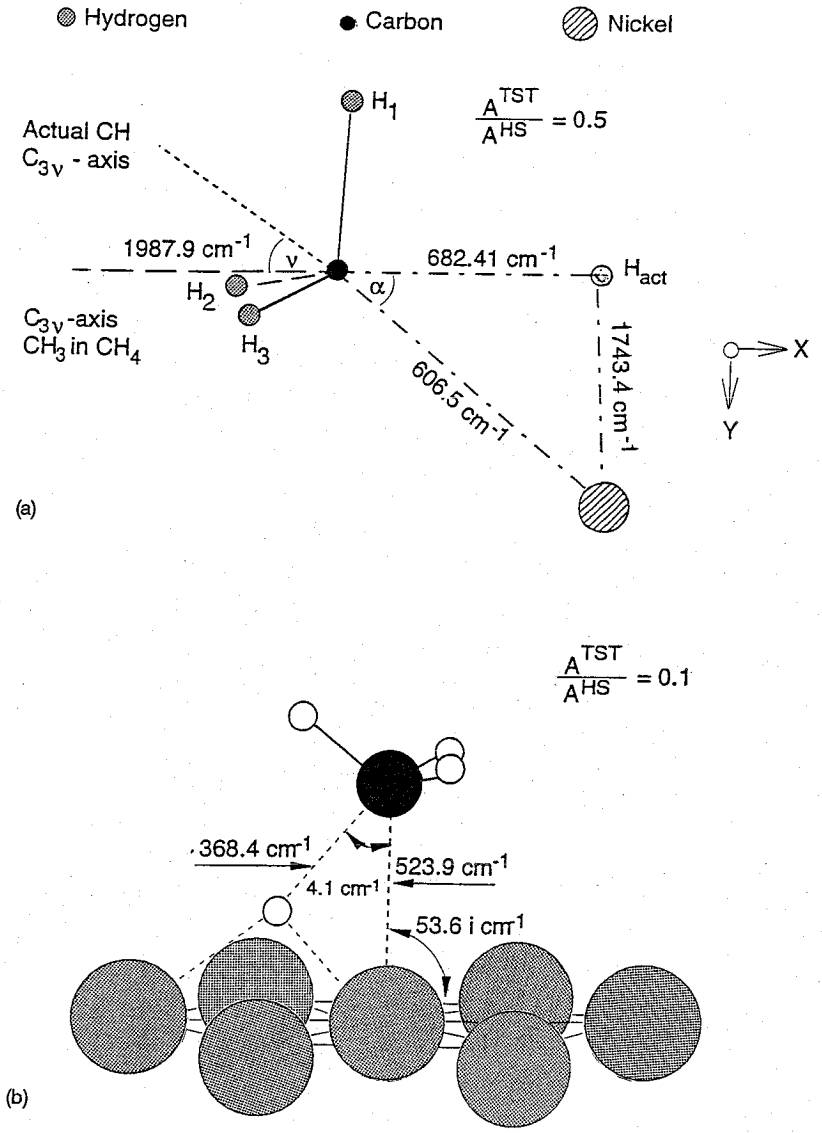

FIG. 34. Transition states for methane dissociation [125]. Real frequencies are vibrational frequencies of transition state normal model. The imaging frequency corresponds to the reaction coordinate. (a) CH_4 dissociation by a Ni atom. (b) CH_4 dissociation on a 7-atom Ni cluster.

in a cluster of atoms is less than that for the single Ni atom alone. The activation energy for dissociative adsorption of methane on the Ni_7 cluster was computed to be 198 kJ/mol, which is nearly four times higher than the experimental value found on Ni surfaces [126]. We have shown in Sec. II.F that the metal–metal bond strengths in a Co_7 cluster are significantly larger

than those in a metal surface. This is the evidence for the low reactivity of such a cluster. We also argued that spherical clusters, such as the Co_{13} cluster shown in Fig. 22, should be expected to have a reactivity that much more closely resembles that of the metal surface. Similar effects may be expected to play a role here on Ni. Indeed we find an activation energy of 99 kJ/mol for the dissociative adsorption of methane to a such a Ni_{13} cluster. This is still, however, nearly two times greater than the experimental measurement. The magnified deviations are attributed to the fact that in the dissociated transition state, there are essentially two adsorbates on the cluster. The results from Fig. 10 suggest that the surface stabilization energy for each will be systematically underpredicted by 20–30 kJ/mol due to the limited cluster size used. Factoring in these cluster size deviations will lower the barrier an additional 40–50 kJ/mol. This now brings the predicted value in line with measured activation barrier.

D. The Catalytic Reaction Cycle of the Oxidation of NH_3 by Cu: Transient Intermediates

The work discussed in this section was inspired by the intriguing experiments of Roberts et al. [127], who suggested that the presence of short-lived (transient) surface intermediates between O_2 and NH_3 initiates the oxidation of ammonia on different transition metal surfaces. This raises the issue whether quantum chemistry can be used to probe the reaction mechanism and discriminate between different mechanistic propositions. More specifically, we analyzed three different routes for the oxidation of ammonia by analyzing the elementary steps leading to ammonia activation, as well as the overall prescribed catalytic cycles. We start with the case of ammonia dissociation on a clean Cu surface. We then analyze the activation of ammonia on Cu in the presence of both atomic and molecular oxygen. Activation barriers, as well as overall reaction energy cycles for each, are presented. In earlier sections we discussed some basic features of ammonia adsorption (Sec. II.B.1) and the interaction of ammonia with oxygen (Sec. II.H). On Cu, ammonia favors the onefold adsorption sites where its bond strength is enhanced by coadsorption with either atomic or molecular oxygen.

1. The Activation of Ammonia by Oxygen [76, 128]

Results presented here were determined from DFT calculations on the same Cu_{11} cluster presented in Sec. II.I. The adsorption, transition state, and product complexes along with corresponding energetic values computed are listed in Fig. 35 for the atomic and molecular oxygen-mediated dissociation paths for ammonia on Cu(111). The difference in energy between adsorbed NH_2 (twofold), hydrogen (onefold), and ammonia (onefold) was found to be +176 kJ/mol, which indicates that ammonia dissociation on

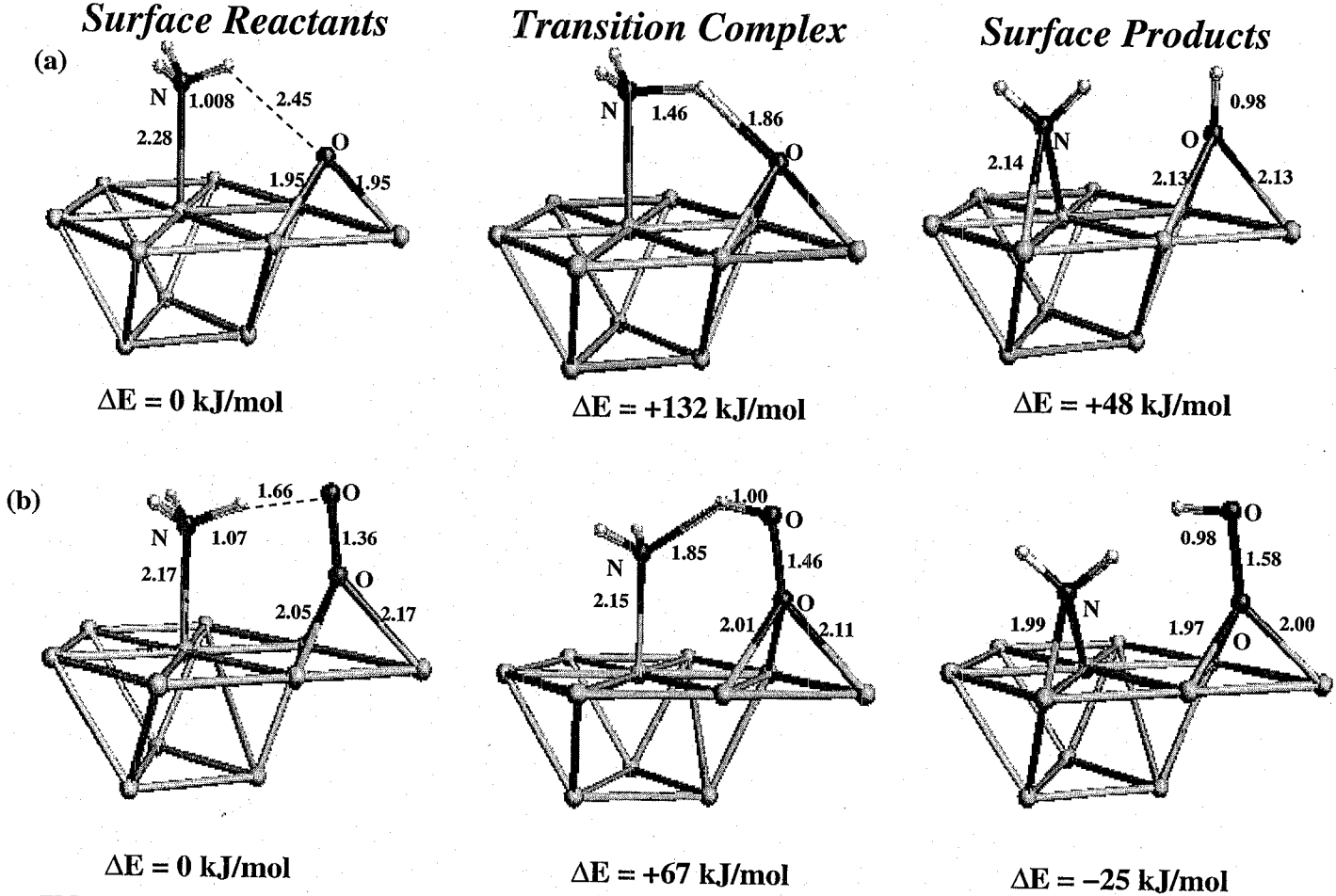

FIG. 35. Optimized reactant, transition complex, and product states along the reaction coordinate for the dissociation of ammonia over Cu(8,3) [77b]. Numbers denote bond length in angstroms. Dissociation mediated by (a) atomic oxygen, (b) molecular oxygen with the formation of the OOH* intermediate.

Cu(111) is highly endothermic. The reaction of NH_3 with atomically adsorbed oxygen to produce NH_2 and adsorbed hydroxyl was endothermic by +48 kJ/mol. The activation barrier for this path (ammonia dissociation in the presence of atomic oxygen) was found to be +132 kJ/mol. This is considerably lower than the 400 kJ/mol required for reaction over the bare Cu surface. In the presence of molecularly adsorbed oxygen, the reaction of NH_3 with O_2 to produce NH_2 and an adsorbed OOH* surface intermediate is exothermic by −25 kJ/mol, and the barrier is lowered even further to +60 kJ/mol.

Clearly, ammonia dissociation requires the presence of either atomic or molecular oxygen to facilitate the activation of the N–H bond and drive the overdissociation path. The results follow the three cited pieces of experimental evidence rather well: (1) ammonia dissociation on a clean copper surface is negligible, (2) dissociation in the presence of preadsorbed oxygen occurs but at a rather slow rate and is impeded by chemisorbed oxygen overlayers (indicative of O* mediated pathways), and (3) NH_3 dissociation is favorable and facile when O_2 and NH_3 are simultaneously introduced to the clean surface (indicative of O_2^* mediated pathways).

The higher reactivity of molecularly adsorbed O_2 and NH_3 compared to that with atomically adsorbed O can be rationalized in terms of bond order conservation theory. The Cu–O bond is quite strong and thus has only a weak interaction with the neighboring hydrogen on ammonia. In the molecular O_2 case, however, the second oxygen atom is in close proximity of the nearby hydrogen. In addition, the oxygen–oxygen bond strength is significantly weakened due to its interaction with the surface. The route for hydrogen abstraction here is favored. As discussed earlier, O_2 weakly adsorbs on Cu(111) via a mechanism consistent with the Blyholder [65]. The filled 2p-orbital donates electrons to the surface while unfilled $2\pi^*$-orbitals accept electrons from a backdonation from the surface, thus considerably weakening the O–O bond. Oxygen will dissociate at room temperature and has a low activation energy due to the large backdonation of electrons from Cu into the antibonding orbitals of O_2. The effective activation barrier for the oxidation of ammonia with oxygen is equal to the activation energy of the surface reaction minus the heat of adsorption of the participating surface species (NH_3^* and O_2^* or O*). The value for the molecularly mediated dissociation route was found to be nearly 20 kJ/mol lower than that for the competing path for the dissociative adsorption of oxygen. Reaction with ammonia will, therefore, only compete with O_2 dissociation when the collision frequency with NH_3 is high. In the experiments by Roberts a large excess of ammonia was used. Figure 35 shows the initial, transition, and final states for the two oxidation reaction modes of ammonia. The weak hydrogen bonding interaction between NH_3 and O_2 favors the negatively charged O_2 molecule to be adsorbed perpendicular to the surface. In the absence of NH_3, however, the oxygen molecule was

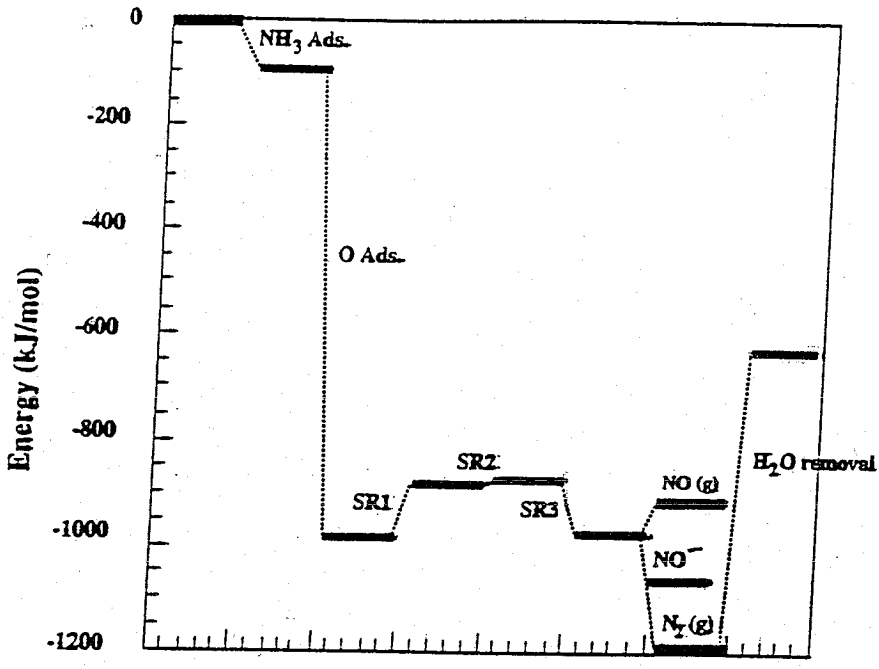

(a)

FIG. 36. (a) The overall energetics for the catalytic reaction cycle $2NH_3(g) + O_2 \rightarrow N_2(g) + H_2O(g)$ for the mechanism controlled by chemisorbed atomic oxygen [77b] The cycle follows the reaction path: (1) NH_3 adsorption; (2) dissociative O_2 adsorption; (3) the sequential hydrogen transfer steps to form NH^*_2(SR1), NH*(SR2), N*(SR3), and OH*. The final terms and steps, $N_2(g)$, NO*, NO(g), and H_2O removal, refer to recombinative desorption of nitrogen adatoms to $N_2(g)$, recombinative desorption of NO, surface reaction of N* and O* to form NO*, and recombination of surface hydroxyl groups to form $H_2O(g)$, respectively. (b) The overall energetics for the catalytic reaction cycle $2NH_3(g) + O_2 \rightarrow N_2(g) + H_2O(g)$ for the mechanism controlled by chemisorbed molecular oxygen [76b]. The cycle follows the reaction paths: (1) NH_3 adsorption; (2) molecular O_2 adsorption; (3) dissociative O_2 adsorption; (4) the sequential hydrogen transfer steps to form NH^*_2(SR5), NH*(SR2), N*(SR3), and OOH*. The final terms and steps, $N_2(g)$, NO*, NO(g), OOH* diss, and H_2O removal, refer to recombinative desorption of nitrogen adatoms to $N_2(g)$, recombinative desorption of NO, surface reaction of N* and O* to form NO*, dissociation of surface OOH* to form O* and OH*, and recombination of surface hydroxyl groups to form $H_2O(g)$, respectively.

found to adsorb parallel to Cu. The interaction of NH_3 with O_2 drives O_2 to the perpendicular adsorption mode. The activation energy for the dissociative surface reaction of NH_3 is seen significantly lower for reaction with adsorbed molecular oxygen than atomic oxygen. This is reflected in the smaller stretch of the N–H bond for reaction with molecular oxygen than for reaction with atomically adsorbed oxygen.

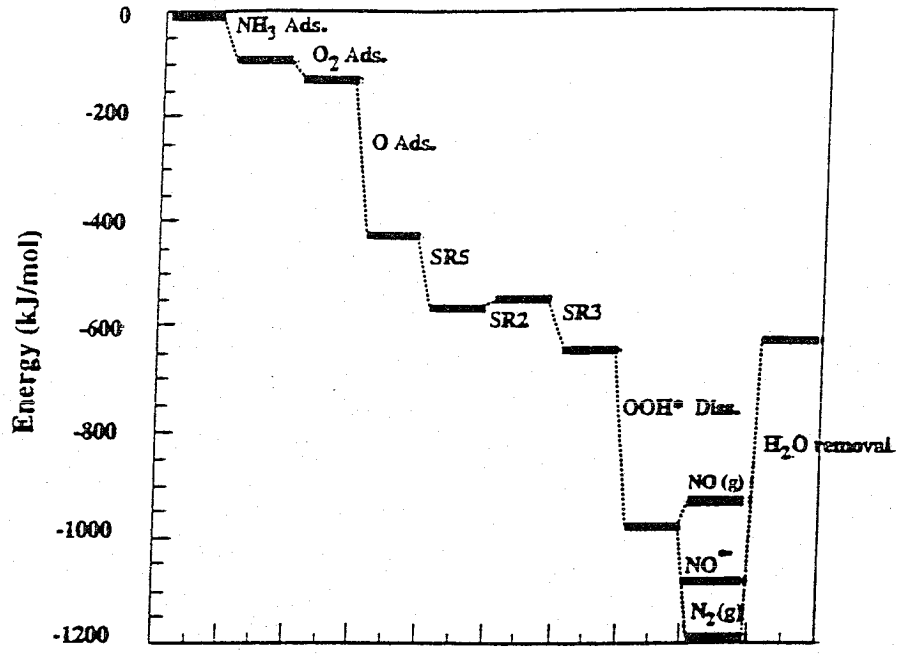

(b)

FIG. 36. Continued.

2. *The Catalytic Reaction Cycle* [*76b, 128, 129*]

The energy changes which correspond to the elementary reaction steps in the overall catalytic reaction cycle for ammonia dissociation are summarized in Figs. 36(a) and 36(b). The energy values shown in Fig. 36 follow from the stoichiometric ratios used in the corresponding elementary reaction equations.

The cycle is initiated here by the adsorption of ammonia, which is relatively weak (-48 kJ/mol) in comparison to the highly exothermic dissociative adsorption of oxygen, which is -300 kJ/mol. It is interesting to note that the largest endothermic step in the overall process appears to be the associative recombination of surface hydroxyls leading to the desorption of H_2O (~185 kJ/mol). In this step, however, there is a large entropic gain which will help drive reaction provided the temperature is high enough. Desorption of H_2O will occur around 200 kelvin.

The next most endothermic step is the initial activation of the first N–H bond of NH_3^* by oxygen to produce the NH_2^* and OH*. This step costs some 50 kJ/mol. The subsequent dissociation step of NH_2^* + O* to NH* and OH* is nearly thermodynamically neutral while the dissociation of NH* + O* to N* and OH* actually becomes exothermic.

This progression from NH_3 to N, which leads to more favorable thermodynamics as the number of hydrogens is reduced, is a very general phenomenon which is also found for the dissociation of hydrocarbons. On a Ni surface, for example, the dissociation of CH_3 is considerably activated, CH_2 and CH, however, dissociate much more readily [129]. The general features can be rationalized in terms of bond order conservation model. The adatom surface bond of an adsorbed nitrogen atom is stronger than that in NH, because of the valency of nitrogen. For atomic adsorption, N is only shared with the surface metal atoms. For the NH fragment, the nitrogen atom is shared with both the hydrogen atom and the surface. This results in a weaker nitrogen–metal bond. The addition of a hydrogen atom to NH to form NH_2 should then cost less in terms of energy than that for attachment of a hydrogen atom to ad-nitrogen atom to form NH.

Returning to the overall cycle depicted in Fig. 36(a), the subsequent recombination of two nitrogen surface atoms on the Cu(111) surface to produce gas-phase N_2 is exothermic. While the surface addition of N* and O* to form NO* is exothermic, the overall step to associatively desorb NO to the gas phase is endothermic due to the high endothermicity for the desorption of NO* [or high exothermicity for the adsorption of NO(g)]. This step, however, becomes considerably more favorable at higher temperatures due to the gain in entropy in going from surface adatoms to NO(g). At higher partial pressures of oxygen, the statistical likelihood of N–O surface pairs is substantially increased over N–N pairs, whereby NO is now suspected to become the dominant product.

In comparing all of the steps, it appears as if the initial activation of the N–H bond by oxygen is likely to be rate limiting. The other two endothermic steps are both desorption processes, which have strong entropic components that drive desorption provided the temperature is high enough. The N–H surface activation step, however, gains little from entropic considerations to the free energy and is therefore suspected to be rate determining. Assuming this to be true and assuming that all other steps in the cycle to be in equilibrium, conventional kinetic expressions can be used to deduce the overall reaction rate for the dissociation of ammonia.

Due to the high heat of dissociative O_2 adsorption, the surface is predicted to have a high coverage with atomic oxygen at the temperature required for the reaction to proceed. The reaction rate is therefore expected to be negative order in oxygen concentration. As ammonia dissociates, both surface hydroxyls and nitrogen adatoms are formed. In addition to these N* and OH* surface species a significant concentration of surface oxygen adatoms is also expected due to the low barrier for O_2 activation. Notwithstanding the more favorable thermodynamics for N_2 formation, the low surface nitrogen adatom concentration and the high surface oxygen adatom concentration significantly increase the chances for N–O collision over N–N collisions. The rate of NO and N_2 formation, as well as the overall reaction

selectivity, is therefore closely tied to the reaction rate constants for the $NH_3^* + O^*$. At higher conversions of NH_3, the surface coverage of nitrogen will increase, and thus the selectivity to NO is expected to decrease because of a higher selectivity for the formation of surface nitrogen.

The oxidative dissociation of NH_3 by reaction with coadsorbed O_2 has a lower activation energy than that by coadsorbed atomic oxygen. Computations of the overall selectivity based on the molecular oxygen ammonia dissociation path suggest a lower product NO/N_2 ratio than the reaction of ammonia with adsorbed atomic oxygen. This helps to illustrate the importance of information on the actual mechanism for reaction.

We did not discuss the effect of lateral surface interactions on the overall catalytic kinetics. For a detailed discussion of this point, we refer the interested reader to Zhdanov [130], who has analyzed consequences due to the resulting nonideal mixing of surface adsorbates. Apart from such statistical effects, lateral interactions may also affect the selectivity by changing the chemical reactivity of adsorbed species. We discuss these features in the next section on the ethylene epoxidation mechanism.

E. Associative Surface Reactions: The Mechanism of Ethylene Epoxidation Catalyzed by Silver, Coadsorbate Promoted Reactivity

The selectivity of the ethylene epoxidation reaction is, to a significant

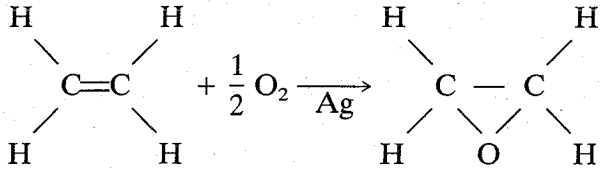

extent, controlled by the chemistry of the oxygen adlayer on the silver surface [131]. The selectivity of the epoxidation reaction increases with increasing oxygen surface coverage. To produce epoxide, the oxygen-to-silver atom ratio in the reactive surface layer has to be in excess of 0.5. Such a surface concentration, however, cannot be accommodated on a silver surface. Some of the adsorbed oxygen atoms are required to move to the subsurface. Using isotope labeling experiments, the presence of this subsurface layer of O atoms has been demonstrated at reaction conditions [132]. It was also determined that the oxygen atoms which exchange between surface and subsurface layer are used to form the epoxide. This demonstrates adsorbed atomic oxygen as the intermediate oxygen species for the epoxidation reaction rather than the molecular oxygen species that had originally been proposed [133].

The nonselective reaction is the total combustion of ethylene. Using

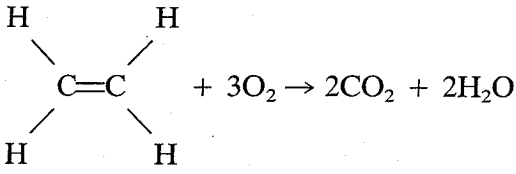

isotopically labeled C_2D_4 [134] it was demonstrated that the nonselective total combustion reaction is initiated by a reaction involving the activation of the C–H bond. The experimental data indicate that the chemical reactivity of atomic oxygen changes with oxygen coverage. The basis for this change was elucidated from a series of DFT quantum-chemical calculations [135]. The interaction of ethylene with atomically adsorbed oxygen was studied on small silver clusters models of the (110) surface. The difference between clusters is the presence of coadsorbed atomic oxygen in subsurface atomic positions. Calculations were repeated on different Ag cluster sizes shown in Fig. 37. Representative results are shown in Fig. 38.

The reaction is conveniently analyzed in terms of the bond order overlap population density for the orbital fragments corresponding to the interaction of ethylene carbon atoms and the adsorbed oxygen adatoms. The results are depicted in Fig. 38. The oxygen atom adsorbed to a silver cluster without subsurface oxygen acts to create bonding as well as antibonding orbital fragments upon interaction with ethylene. The antibonding orbitals are partially occupied as displayed by the band passing through the Fermi energy in Fig. 38(a). The oxygen atoms bound to silver in sites with a high

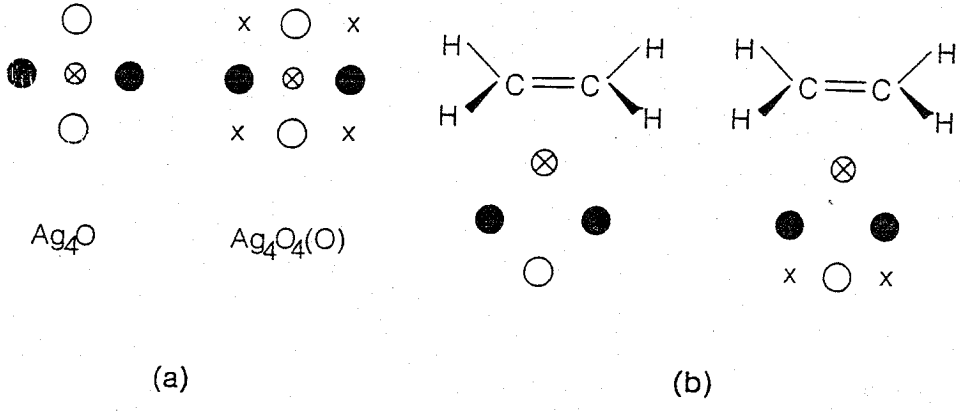

FIG. 37. The silver cluster with the Ag(110) surface geometry [135]. ⊗, chemisorbed oxygen atom; ●, silver atom in outer layer; ○, silver atom in inner layer; ×, subsurface oxygen atom. (a) top view without ethylene; (b) side view with ethylene.

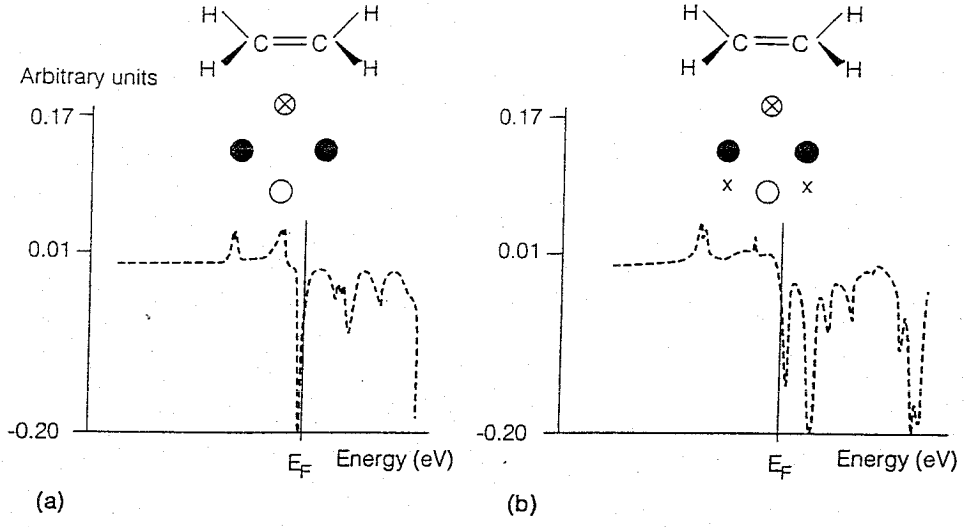

FIG. 38. Bond order overlap densities of ethylene C and O_{ads} orbitals [135]: (a) without subsurface oxygen; (b) with subsurface oxygen.

oxygen density, however, have only bonding occupied orbital fragments. The contact between the π-orbital of ethylene and the isolated adsorbed oxygen atom is then repulsive.

On the oxygen-rich site, however, the interaction potential obtains a significant attractive contribution due to the depletion of antibonding fragment orbitals. This favors the approach of the two ethylene–carbon atoms to the oxygen and results in epoxidation. The Pauli repulsion between the oxygen adatom and ethylene is converted into an attractive interaction by the promotion of coadsorbed oxygen atoms. Interestingly, the distribution of the electrons between bonding and antibonding orbital fragments of the oxygen adatom with the Ag cluster in the presence (or absence) of coadsorbed subsurface oxygen behaves in an opposite way (see Fig. 39).

On the oxygen-rich cluster, bonding, as well as antibonding, orbital fragments between oxygen adatoms and neighboring silver atoms are occupied by electrons. On the isolated oxygen atom cluster, however, the antibonding orbital fragments are empty. The result is a weak Ag–O bond for the oxygen-rich cluster and a strong Ag–O bond for the isolated oxygen atom cluster. This subsequently leads to a strong $O-C_2H_4$ interaction on the oxygen-rich and a weak $O-C_2H_4$ on the isolated oxygen atom cluster, which is in agreement with bond order conservation expectations. The interaction of ethylene with the oxygen-rich cluster polarizes the reacting oxygen atom so that it becomes electron depleted. It can then readily insert into the electron-rich ethylene π-bond. Note that without the interaction with ethylene, the oxygen atom has a negative charge. Interaction with ethylene polarizes the O–Ag bond such that electrons become donated into

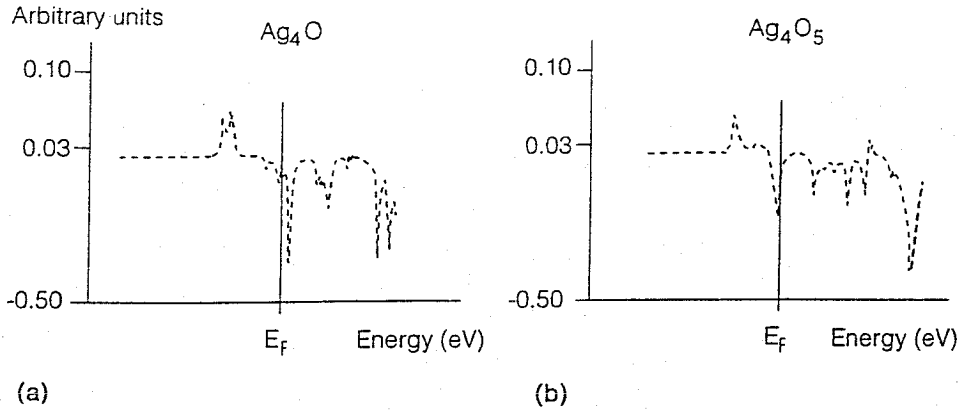

FIG. 39. Bond order overlap population densities of the $Ag-O_{ads}$ bonds [135]: (a) $Ag_4(O_{ads})$; (b) $Ag_4O_4(O_{ads})$.

empty cluster orbitals. The oxygen inserted into the π-bond of ethylene has become electrophilic upon contact with ethylene! For the low oxygen concentration cluster, this is not possible because of the lower energy of the $O-C_2H_4$ antibonding orbital fragments with respect to the unoccupied silver cluster orbitals. The promoting role of subsurface oxygen can be replaced by other electronegative elements. In practice chlorine is used.

F. The Fischer–Tropsch Chain Growth Reaction: Associative Recombination

In Secs. III.A and III.B, we discussed the energetics and dynamics of CO and NO dissociation. CO dissociation has been demonstrated to be the elementary step in the catalytic reaction cycle, which produces the surface C_1-adspecies that are the building units for the hydrocarbons formed in the Fischer–Tropsch synthesis gas conversion reaction [136]:

$$CO + 2H_2 \rightarrow \text{“}CH_2\text{”} + H_2O$$

or

$$2CO + H_2 \rightarrow \text{“}CH_2\text{”} + CO_2$$

In order to dissociate a molecule, the energy difference between the initial and final products has to be thermodynamically acceptable. A surface reaction path of low activation energy requires optimal backdonation of metal electrons into antibonding orbitals, thus weakening the molecular CO bond (Secs. II.D. and III.A). For the association reaction, one expects the reverse to be more favorable. The more weakly the surface fragments interact with the surface, the more favorable the association reaction becomes.

Depletion of electron density from the antibonding orbital fragments

formed by combining adfragments will now relieve repulsive interactions and assist the association reaction. An example of the latter is provided for by the "oxygen-promoted" oxygen insertion into the electron-rich π-bond discussed in the previous example.

The carbon–carbon bond formation path was modelled using the ASED method and the clusters presented earlier for the CO dissociation examples. The results are given in Fig. 40. The chosen reaction coordinate, displayed in Fig. 40, is depicted here in **I**. The reaction coordinate, X, refers to the

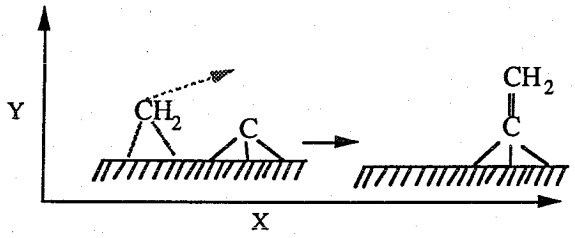

I

distance along the surface that the CH_2 group travels in forming the $C{=}CH_2$ product. In the scheme in Fig. 40, the reaction proceeds from left to right. The reactants are CH_2^* and C^* surface species (X = 0) while the product is the surface vinylidene species (X = final).

The recombination of a surface carbide atom with a surface CH_2 species is shown for the (111) surfaces of Pd, Rh, and Ru. Reactivity differences

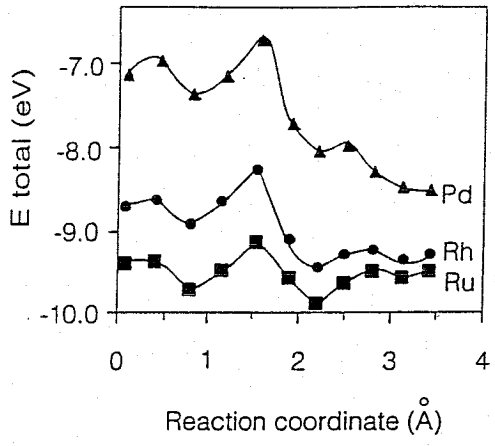

FIG. 40. Potential energy curves for carbon–carbon bond formation on Ru, Rh, and Pd surfaces from C_{ads} + CH_{2ads} to give $CH_2{=}C_{ads}$ [138]. The reaction coordinate is the distance between the carbon fragments along the reaction path.

over different metal clusters are attributed to the differences in the total number of valence electrons for each metal. Once again, the difference in the binding energy of fragments, the carbon atom and carbene, varies much more strongly with the metal than that of the vinylidene species with its C–C bond intact. The reaction path with the lowest activation barrier is that which crosses the minimum number of metal surface atoms between the reactants and product. This implies movement of the CH_2 species over a metal surface atom [137]. Carbon–carbon bond formation is found to be thermodynamically most favored for Pd, which has the weakest metal–carbon bonds. Indeed, graphitic overlayers are known to form more readily on surfaces of nonreactive metals, whereas carbidic overlayers are more favored by the more reactive metals. While carbon–carbon bond formation is thermodynamically favored by metals with the high d-valence electron count (Pd > Rh > Ru), the selectivity of C_2^+ formation in the presence of hydrogen increases experimentally in the opposite order Ru > Rh > Pd [138]. This is due to the appearance of a competing reaction path. In the presence of hydrogen, methane formation becomes the predominant reaction that competes with formation of higher hydrocarbons. The selectivity, therefore, depends on the relative value of the reaction rate for methanation versus that for carbon–carbon bond formation. As noted from Fig. 40, the activation energy for carbon–carbon bond formation varies very little for the three metals.

On the contrary, the activation energy for methane formation will vary strongly with the strength of the metal–carbon bond. A surface methyl group must first be hydrogenated. This requires considerable elongation of the metal–carbon bond length. Due to the low activation energy for carbon–carbon bond formation, the selectivity for C_2^+ formation is favored at low temperatures. In the transition state for carbon–carbon bond formation, the metal–carbon bonds are still to a considerable extent intact (see Fig. 41). This is the main reason for the weak dependence of the activation energy for carbon–carbon bond formation on the metal–carbon interaction that was found in the extended Hückel calculations.

One can extend the analysis presented here to a general understanding of experimental selectivity differences between different metals [138]. For example, methanol formation will be favored on such metal surfaces that do not dissociate CO very easily. This is the reason why Cu, with its completely filled d-valence electron band, has a low selectivity for methane formation but a high selectivity for methanol. On nickel, CO dissociates much more easily, and therefore methane is the main product. On Co, the stronger metal carbon bond leads to C_{2+} production with higher selectivities. Reduced Fe is very reactive and reacts with CO and hydrogen to form an iron carbide. The carbon bonds of the carbide are too strong to react at mild conditions with hydrogen [139]. Nonetheless, iron is still an excellent Fischer–Tropsch catalyst. On the less reactive iron carbide surface, CO

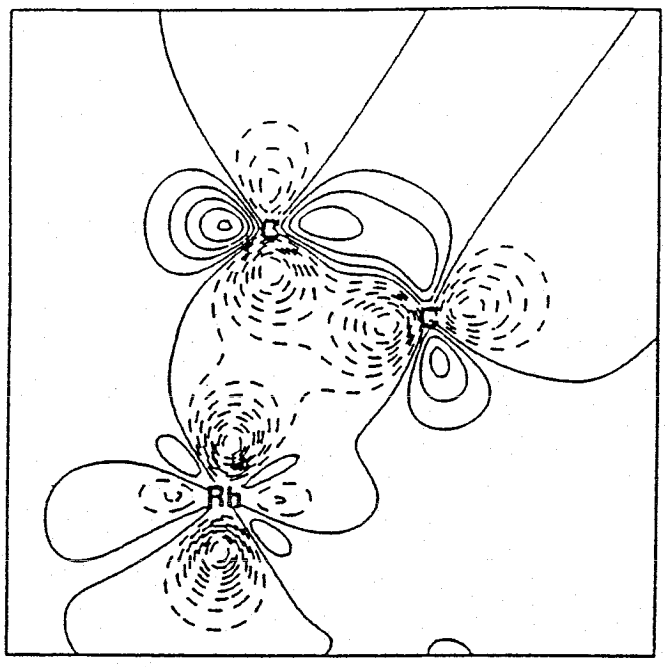

FIG. 41. Changes in electron density of C and CH_2 in the transition state during coupling on a Rh(111) surface [138]. Calculated is the change in electron density by subtracting the electron density of the loose fragments (Rh_{11} cluster, CH_2, and C) from those of the Ru_{11}–C–CH_2 cluster. The dotted line connects points with the same electron density loss; the solid line connects points with the same increase of electron density.

dissociation still occurs and carbon–carbon recombination competes efficiently with methane formation. On more reactive metals, stable carbidic or oxidic surface overlayers form and no longer react to higher hydrocarbons. Continuing to the next row of the periodic system, Pd has a low activity and produces methanol as well as methane. On Rh particles, the dissociation probability of CO has become comparable to that of CO desorption. Higher oxygenates can therefore be produced. Ruthenium readily dissociates CO and is an excellent alkane-forming catalyst. Platinum and iridium have a low activity, because the strong CO chemisorption bond inhibits CO dissociation [140].

G. The Principle of Sabatier

According to the principle of Sabatier, there exists a specific adsorbate–surface interaction for which the reaction rate of a catalytic reaction is optimum. If the adsorbate–surface interaction is weak, the rate for dissociative adsorption becomes limiting. On the other hand, when the adsorbate–surface interaction strength becomes too strong, the rates of de-

sorption become limiting. At the adsorbate–surface interaction optimum, the rate constants for dissociative adsorption and associated desorption tend to balance. Hence, while the adsorbate–metal interaction energies tend to uniformly increase with decreasing d-electron occupation of the transition metal surface, the rate of a catalytic reaction has an optimal activity for elements with a particular d-electron content (usually an intermediate count). In ammonia synthesis, for example, Fe has the maximum rate for all third row transition metal surfaces (see Ref. 4a). When one compares the surface coverage to the left of the Sabatier optimum (a weak adsorbate–surface interaction) with that to the right (a strong adsorbate–surface interaction), the surface coverage has likely changed. To the left, the surface coverage is low, while to the right the adsorbate–surface coverage is high. The high surface coverage limits lead to site blocking. Surface dissociation reactions are especially strong functions of surface coverage. As we have shown in Sec. III.A, molecular dissociation requires a critical ensemble of surface atoms to carry out the dissociation. The rate of dissociation is, therefore, highly dependent upon the surface coverage. Assuming the rate of CO dissociation to be rate limiting, the rate of methanation follows from the surface coverage, θ_{CO}. At low hydrogen coverage, θ_{CO} follows from the adsorption isotherm of CO. Assuming Langmuir adsorption, one finds for the rate of methanation:

$$r_{CH_4} = r_{diss} = k_{diss}\left[\frac{K_{CO}P_{CO}}{(1 + K_{CO}P_{CO})^2}\right] \qquad (x = 1) \tag{25}$$

The part within the brackets is a maximum at $K_{CO}P_{CO} = 1$. This gives an approximate definition for the optimum adsorbate–surface interaction strength for the methanation reaction. Using Polanyi's relationship [Eq. (10)] in conjunction with Eq. (25), one can arrive at a reaction rate expression that is an explicit function of the interaction energy. k_{diss} will therefore change with variation of the adsorbate–surface interaction strength. The optimum interaction values will be different for different catalytic systems. They depend not only on the reactants but also on the mechanism of reaction. Hence, a general theory of catalysis, based on the identification of the optimal surface electronic distributions for catalytic reactions, is only partially useful. As a corollary to the principle of Sabatier expression, Eq. (25) indicates that the order of the reaction will also change in comparing the rates for weak versus strong adsorbate–surface interaction. For a weak interaction the rate is first-order in the partial pressure of CO; for strong interaction the order becomes negative in the partial pressure of CO.

IV. CONCLUDING REMARKS

We presented an overview of governing theoretical catalytic concepts, illustrated with selected examples mainly from our own work on transition

metal catalysis, as well as highlights from other theoretical work and available experimental data. The focus has been on the relation between the nature of the surface–chemical bond and its importance altering the selectivity of a catalytic reaction. This relationship is complex due to the relative number and competition of elementary steps which comprise the overall catalytic cycle and the nonlinear way in which different adsorbates interact on surfaces. The composition of the catalytic surface overlayer is of great importance in dictating reaction selectivity. The makeup of the overlayer and its dynamic changes throughout reaction strongly depend upon the operating conditions. Different conditions can actually alter the nature of the rate-limiting step.

A selective catalytic reaction requires that the strengths of the adsorbate–surface chemical bonds are such that adsorption, activation, and desorption occur at the same conditions. This leads to an optimum interaction energy for a maximum in the desired catalytic reaction rate. This is the basis of Sabatier's principle. Sometimes no satisfactory compromise between surface activation and surface association conditions exists. Consecutive reaction steps are then necessary over the same catalyst set at different operating conditions to achieve the desired activity or selectivity [139]. We have discussed in detail the factors that determine the strength of the chemisorption bond and control adsorbate recombination reactions. These factors can be considered reasonably well understood.

The nature of the surface–chemical bond is described here in terms of bonding and antibonding orbital fragments formed between adsorbate and surface metal atomic orbitals. Information on the upward and downward shifts of these orbitals in the adsorption complex, while important, cannot be used alone to predict bond strengths. The bond strength is determined by the distribution of electrons over the bonding, as well as antibonding, adsorbate–surface orbital fragments. There is a considerable redistribution of the electrons over bonding and antibonding orbitals within the transition metal upon formation of the surface–chemical bond. Electron occupation of antibonding orbital fragments leads to Pauli repulsion; the occupation of bonding orbital fragments results in attractive interactions. A large local density of states of orbitals around the Fermi level gives rise to a large interaction with adsorbate valence orbitals and a large splitting between bonding and antibonding adsorbate–surface orbital fragments. The relative position of the Fermi level of the metal with respect to these bonding and antibonding fragment orbitals determines the electron distribution over these surface–orbital fragments. The bond strength of adatoms is very sensitive to variation of the coordination number, metal valence electron distribution, and changes in surface geometry. This dependence is less severe for molecules, due to the counteracting changes of donating and back-donating contributions to the bond energy.

Electron density changes on the surface metal atoms involved in the

chemisorptive bond usually lead to a bond weakening of the metal–metal bonds next to the adsorption site. The atoms involved in the adsorbate–surface bond can adjust their distances in order to optimize the adsorbate–surface atom interaction. When the weakening of the surface metal bonds is large, surface reconstruction may be a consequence. The electron density redistribution induced by chemisorption depends on the surface state, as well as the size and shape of metal clusters. The differences in electronic response are mainly responsible for the differences in their reactivity. Repulsive, as well as attractive, lateral interactions of coadsorbates can be the consequence of the short-range interactions mediated by the perturbed metal–surface electron distributions. These short-range lateral interactions may cause long-range effects due to nonideal mixing of coadsorbates, formation of ordered layers, and island formation. Long-range effects are statistical thermodynamic consequences of these short-range lateral interactions.

Repulsive lateral interactions occur when coadsorbates share the same surface atom. They may, of course, also appear when coadsorbates are adsorbed so close to each other that they experience a direct repulsive interaction due to orbital overlap. Attractive lateral effects appear via metal electron density mediated interactions, when coadsorbates share next-nearest-neighbor metal atoms. In addition to the through-metal interactions direct electrostatic interactions may also be effective. Surface metal atoms or cluster metal atoms with a low number of neighbor surface atoms are usually more reactive than surface atoms with higher neighbor atom coordination numbers. This is the result of the lower degree of delocalization of electrons on atoms with low coordination numbers.

Surface reaction paths are primarily controlled by the factors that increase the exothermicity of the surface reaction and lower the activation energy. A low activation energy is often favored by reaction paths that follow the minimum surface atom sharing principle. When the surface fragments generated upon dissociation are only stable in high coordination sites, surface dissociation reactions require an ensemble of surface atoms for dissociation.

The reactivity of open surfaces or small clusters is usually larger than that of the dense surface, because of the increased sensitivity of adatoms or surface fragments to reactivity changes than adsorbed molecules. For adsorbate dissociation the activation energy is minimized by electron back-donation into adsorbate, bond-weakening, antibonding orbitals. Bond formation between adsorbates in associative recombination reactions is favored by a depletion of antibonding fragment orbitals through donation of electrons to the surface. These electronic interactions require the interaction with surface group orbitals of a symmetry that matches that of antibonding orbitals of adsorbate orbitals. This restricts the options for surface reaction paths. The selectivity of a reaction depends on relative reaction probabil-

ities. For competitive association reactions it will also depend on the probability for recombination with a particular coadsorbed surface intermediate. This probability is controlled by the surface adlayer composition and surface phases. When an association reaction competes with a dissociation reaction, there is an optimum in the surface interaction energy. Again the composition of the surface adlayer is important. A dissociation reaction requires an ensemble of vacant surface atoms, whose availability will depend on surface concentration. The rate of surface dissociation reactions will, therefore, be strongly surface coverage dependent. Lateral effects may stabilize the presence of a particular overlayer (surface reconstruction) or a selective reactive intermediate (e.g., electropositive oxygen for epoxidation). To predict the activity and selectivity of a catalytic reaction, all elementary reaction steps have to be known. This includes rates of formation of surface species that do not participate in the reaction (spectator species) but control the reactivity of the catalytically active surface adlayer. The electron density and electron redistribution controls the stability of surface intermediates. Microstatistical kinetics will, in the end, be used to help determine overall catalytic behavior.

ACKNOWLEDGMENT

We gratefully acknowledge Joop van Grondelle for his help in preparing figures.

REFERENCES

Text

1. J. A. Dumesic, D. F. Rudd, L. M. Aparicio, J. E. Rekoske, and A. A. Trevino, *The Microkinetics of Heterogeneous Catalysis*, ACS, Washington, DC, 1993.
2. R. A. van Santen, *Theoretical Heterogeneous Catalysis*, World Scientific, Singapore 1991.
3. (a) G. Ertl, *Surf. Sci.*, *299/300*, 742 (1994). (b) G. Ertl, *Crit. Rev. Solid State Mater. Sci.*, 1982, p. 349. (c) T. N. Rhodin and G. Ertl, *The Nature of the Surface Chemical Bond*, North-Holland, Amsterdam, 1979. (d) G. A. Somorjai, *Surf. Sci.*, *299/300*, 849 (1994). (e) G. A. Somorjai, *Chemistry in Two Dimensions*, Cornell University Press, 1981. (f) G. A. Somorjai, *Introduction to Surface Chemistry and Catalysis*, Wiley, New York, 1994. (g) R. J. Madix, *Surf. Sci.*, *299/300*, 785 (1994).
4. (a) J. K. Norskov, *Progr. Surf. Sci.*, *38*, 103 (1992). (b) P. Feiblman (LDF), *Surf. Sci.*, *299/300*, 426, 1994. (c) T. H. Upton and W. A. Goddard, *CRC Crit. Rev. Solid State Mater. Sci.*, *10*, 261 (1981). (d) D. R. Salahub, M. Catro, and E. I. Proynov, NATO ASI B318, *Relativistic and Electron Cor-*

relation Effects in Molecules and Solid (G. L. Malli, ed.), Plenum Press, New York, 411 (1994). (e) T. H. Upton and W. A. Goddard, *CRC Crit. Rev. Solid State Mater. Sci.*, *10*, 261 (1981). (f) D. E. Ellis, J. Guo, H. P. Cheng, and J. J. Low, *Adv. Quant. Chem.*, *22*, 125 (1991).

5. (a) J. Koutecky, *Phys. Rev.*, *108*, 13 (1957). (b) T. B. Grimley, *Adv. Catal.*, *12*, 24 (1960). (c) D. M. Newns, *Phys. Rev.*, *178*, 1123 (1969). (d) J. R. Schrieffer, in *Dynamic Aspects of Surface Physics*, Proc. Int. School of Physics, Enrico Fermi course XVII, Bologna, 1974. (e) J. W. Gadzuk, *J. Vac. Techn.*, *12*, 90 (1975). (f) J. W. Gadzuk, *Phys. Rev. B*, *14*, 2267 (1976). (g) N. D. Lange and A. R. Williams, *Phys. Rev. B*, *18*, 616 (1978). (h) N. D. Lange and A. R. Williams, *Phys. Rev. Lett.*, *37*, 212 (1976). (i) J. K. Norskov, *Progr. Surf. Sci.*, *38*, 103 (1992).
6. (a) R. Hoffmann, *Solids and Surfaces*, VCM publishers, New York, 1988. (b) R. Hoffmann, *Ang. Chem. Ent. Ed. Eng.*, *21*, 711 (1982). (c) T. A. Albright, J. K. Burdett, and M. H. Whangbo, *Orbital Interactions in Chemistry*, Wiley, New York, 1985. (d) Fukui, *Science*, *218*, 747 (1982).
7. (a) R. A. van Santen and E. J. Baerends, in *Theoretical Models of Chemical Bonding*, Part 4 (Z. B. Maksic, ed.), Springer Verlag, 1991. (b) E. J. Baerends, in *Cluster Models for Surface and Bulk Phenomena*, NATO ASI, B283 (G. Pacchioni and P. Bagus, eds.), Plenum Press 1992.
8. R. Smoluchowski, *Phys. Rev.*, *60*, 661 (1941).
9. J. C. Slater, *Phys. Rev.*, *81*, 385 (1951).
10. J. C. Slater, *Adv. Quant. Chem.*, *6*, 1 (1972).
11. J. C. Slater, *The Self Consistent Field for Molecules and Solids: Quantum Theory of Molecules and Solids*, McGraw-Hill, New York, 1974.
12. K. H. Johnsom and R. P. Messner, *Int. J. Quant. Chem. Symp.*, *10*, 47 (1976). K. H. Johnson, *Adv. Quant. Chem.*, *7*, 143 (1973).
13. V. A. Gubanov, J. Weber, and J. W. P. Connolly, *J. Chem. Phys.*, *64*, 1455 (1975).
14. (a) S. Harris, *Chem. Phys.*, *67*, 229 (1982). (b) S. Haris and R. R. Chianelli, *J. Catal.*, *86*, 400 (1984).
15. (a) E. M. Shustorovich, *Surf. Sci. Rep.*, *6*, 1 (1986). (b) E. M. Shustorovich, *Adv. Catal.*, *37*, 101 (1990). (c) E. M. Shustorovich and A. T. Bell, *Surf. Sci.*, *268*, 397, 19 (1992).
16. A. T. Bell, in *Metal–Surface Reaction Energetics: Theory and Applications to Heterogeneous Catalysis, Chemisorption, and Surface Diffusion*, VCH, New York, 1991, p. 191.
17. J. Benziger, in *Metal–Surface Reaction Energetics: Theory and Applications to Heterogeneous Catalysis, Chemisorption, and Surface Diffusion*, VCH, New York, 1991.
18. H. Sellers, *Surf. Sci.*, *310*, 281 (1994).
19. Baetzhold, in *Metal–Surface Reaction Energetics: Theory and Applications to Heterogeneous Catalysis, Chemisorption, and Surface Diffusion*, VCH, New York, 1991.
20. E. M. Shustorovich (ed.), in *Metal–Surface Reaction Energetics: Theory and Applications to Heterogeneous Catalysis, Chemisorption, and Surface Diffusion*, VCH, New York, 1991.
21. E. M. Shustorovich and A. T. Bell, *J. Catal.*, *113*, 341 (1988).

22. E. M. Shustorovich and A. T. Bell, *Surf. Sci.*, *268*, 397 (1992).
23. E. M. Shustorovich, in *Quantum Chemistry Approaches to Chemisorption and Heterogeneous Catalysis* (F. Ruette, ed.), Kluwer Academic Pub., Netherlands, 1992, p. 233.
24. (a) R. Hoffmann, *J. Chem. Phys.*, *19*, 1397 (1963). (b) R. Hoffmann, *Rev. Mod. Phys.*, *60*, 101 (1988). (c) R. Hoffmann, *Angnew. Chem. Int. Ed. Engl.*, *26*, 846 (1987). (d) R. Hoffmann and W. N. Lipscomb, *J. Chem. Phys.*, *36*, 2179 (1962). (e) R. Hoffmann and W. N. Lipscomb, *J. Chem. Phys.*, *37*, 2872 (1962).
25. (a) A. B. Anderson, R. W. Grimes, and S. Y. Hong, *J. Phys. Chem.*, *91*, 4245 (1987). (b) A. B. Anderson, *J. Chem. Phys.*, *60*, 2477 (1974). (c) A. B. Anderson, *J. Chem. Phys.*, *62*, 1187 (1975). (d) A. B. Anderson and R. Hoffmann, *J. Chem. Phys.*, *60*, 4271 (1974). (e) A. B. Anderson and J. A. Nichols, *J. Am. Chem. Soc.*, *108*, 1385 (1986). (f) A. B. Anderson, *Inorg. Chem.*, *15*, 2598 (1976).
26. (a) A. B. Anderson and J. J. Maloney, *J. Phys. Chem.*, *92*, 809 (1988). (b) D. B. Kang and A. B. Anderson, *J. Am. Chem. Soc.*, *107*, 7858 (1985). (c) A. B. Anderson, M. R. McDevitt, and F. L. Urbach, *Surf. Sci.*, *146*, 80 (1984).
27. (a) M. J. S. Dewar and W. Thiel, *J. Am. Chem. Soc.*, *99*, 15, 4899 (1977). (b) M. J. S. Dewar, E. G. Zoebisch, E. F. Healy, and J. P. Stewart, *J. Am. Chem. Soc.*, *107*, 3902 (1985). (c) J. J. P. Stewart, *J. Comp. Chem.*, *10*, 2, 209 (1989). (d) M. J. S. Dewar, C. Jie and J. Yu, *Tetrahedron*, *49*, 34, 7393 (1993). M. J. S. Dewar, C. Jie, and J. Yu, *Tetrahedron*, *49*, 23, 5003 (1993). A. J. Holder, AMPAC 5.0, Semichem Company, 1994. (e) See also *Reviews in Computational Chemistry* (K. B. Lipkowitz and D. B. Boyd, eds.), VCH, New York, Vols. 1–5.
28. (a) F. Ruette and A. J. Hernandez, in *Computational Chemistry: Structure, Interactions and Reactivity* (S. Fraga, ed.), Studies in Phys. and Theoretical Chemistry 77, Elsevier Sci. Pub. B. B., 1992. (b) F. Ruette, A. Sierraalta, and A. J. Hernandez, in *Quantum Chemistry Approaches to Chemisorption and Heterogeneous Catalysis* (F. Ruette, ed.), Kluwer Academic Pub., Netherlands, 1992, p. 233.
29. (a) D. Bacon and M. C. Zerner, *Theo. Chim. Acta*, *53*, 21 (1979). (b) J. Ridley and M. Zerner, *Theo. Chim. Acta*, *32*, 111 (1973). (c) M. C. Zerner, G. H. Loew, R. F. Kirchner, and U. T. Mueller-Westerhoff, *J. Am. Chem. Soc.*, *102*, 589 (1980). (d) M. Zerner and D. R. Salahub (eds.), *The Challenge of d and f Electrons: Computation and Theory*, ACS Symposium Series 394, 1989.
30. G. L. Estiu and M. C. Zerner, *Int. J. Quant. Chem.: Quant. Chem. Symp.*, *27*, 195 (1993). G. L. Estiu and M. C. Zerner, *J. Phys. Chem.*, *97*, 51, 13720 (1993). G. L. Estiu and M. C. Zerner, *J. Phys. Chem.*, *98*, 98, 9972 (1994).
31. (a) J. K. Norsov and N. D. Lang, *Phys. Rev. B*, *21*, 2136 (1980). (b) J. K. Norskov, *Phys. Rev. B*, *26*, 2875 (1982). (c) J. D. Kress and A. E. DePristo, *J. Chem. Phys.*, *87*, 4700 (1987). (d) J. D. Kress and A. E. DePristo, *J. Chem. Phys.*, *99*, 2596 (1988). (e) T. J. Raeker and A. E. DePristo, *Phys. Rev. B*, *39*, 99676 (1989).
32. M. S. Dow, S. M. Forles, and M. I. Baskesy, *Mater. Sci. Rep.*, *9*, 7&8, 1993.

33. C. W. Bauschlicher, Jr., *J. Chem. Phys.*, *101*, 4, 3250 (1974). C. W. Bauschlicher, Jr., P. S. Bagus, C. J. Nelin, and B. O. Roos, *J. Chem. Phys.*, *85*, 354 (1986). C. W. Bauschlicher, Jr., and P. S. Bagus, *J. Chem. Phys.*, *81*, 58898 (1984). S. P. Walch and C. W. Bauschlicher, Jr., in *Comparison of ab initio Quantum in Chemistry with Experiment* (R. Bartlett, ed.), Boston, Reidel, 1985, p. 17. C. W. Bauschlicher and S. R. Langhoff, *J. Chem. Phys.*, *85*, 5936 (1986). S. R. Langhoff and C. W. Bauschlicher, Jr., *Chem. Phys. Lett.*, *124*, 241 (1986). C. W. Bauschlicher, *Chem. Phys. Lett.*, *129*, 586 (1986).
34. (a) P. E. M. Siegbahn, U. Wahlgren, and E. Shustorovich, in *Metal–Surface Reaction Energetics: Theory and Applications to Heterogeneous Catalysis, Chemisorption, and Surface Diffusion*, VCH, New York, 1991. (b) P. E. M. Siegbahn, M. R. A. Blomberg, and C. W. Bauschlicher, Jr., *J. Chem. Phys.*, *81*(4), 2103 (1984). (c) P. E. M. Siegbahn and I. Panas, *Surf. Sci.*, *240*, 37 (1990). (d) P. E. M. Siegbahn and U. Wahlgren, *Int. J. Quant. Chem.*, *42*, 1149 (1992). (e) P. E. M. Siegbahn and M. R. A. Blomberg, *J. Am. Chem. Soc.*, *114*, 10548 (1992). (f) P. E. M. Siegbahn, M. R. A. Blomberg, and M. Svensson, *J. Am. Chem. Soc.*, *115*, 1952 (1993). (g) P. E. M. Siegbahn, *J. Am. Chem. Soc.*, *115*, 5803 (1993). (h) P. E. M. Siegbahn and M. Svensson, *Chem. Phys. Lett.*, *216*(1,2), 147 (1993). (i) P. E. M. Siegbahn, M. R. A. Blomberg, and M. Svensson, *J. Am. Chem. Soc.*, *115*, 4191 (1993). (j) P. E. M. Siegbahn, *Theor. Chim. Acta*, *87*, 277 (1994). (k) P. E. M. Siegbahn and M. R. A. Blomberg, *Organmet.*, *13*, 354 (1994). (l) M. R. Blomberg, K. Brandemark, and P. E. M. Siegbahn, *J. Am. Chem. Soc.*, *105*, 5557 (1983). (m) M. R. Blomberg, P. E. M. Siegbahn, K. Nagashima, and J. Wennerberg, *J. Am. Chem. Soc.*, *113*, 424 (1991).
35. (a) E. J. J. Kirchner and E. J. Baerends, *Surf. Sci.*, *311*, 126 (1994). (b) E. J. J. Kirchner and E. J. Baerends, *Surf. Sci.*, *304*, 12 (1994). (c) E. J. J. Kirchner and E. J. Baerends, *J. Chem. Phys.*, *97*(5), 3821 (1992). (d) P. J. van den Hoek and E. J. Baerends, *Appl. Surf. Sci.*, *41*, 236 (1989). (e) A. Rosa and E. J. Baerends, *Inorg. Chem.*, *33*, 584 (1994). (f) R. L. DeKock, M. A. Peterson, L. E. Renolds, L. H. Chen, E. J. Baerends, and P. Vernooijs, *Organomet.*, *12*(7), 2794 (1993). (g) E. A. Schmitt, L. Noodleman, E. J. Baerends, and D. Hendrickson, *J. Am. Chem. Soc.*, *114*(15), 6109 (1992). (h) M. A. Buijse and E. J. Baerends, *Theor. Chim. Acta*, *79*(6), 389 (1991). (i) M. A. Buijse and E. J. Baerends, *J. Chem. Phys.*, *93*(6), 4129 (1990). (j) P. J. van den Hoek and E. J. Baerends, *Surf. Sci.*, *221*, 3 (1971).
36. (a) T. Ziegler, W. Cheng, E. J. Baerends, and W. Ravenek, *Inorg. Chem.*, *27*, 3458 (1988). (b) T. Ziegler, *Pure Appl. Chem.*, *63*(6), 873 (1991). (c) T. Ziegler, E. Folga, and A. Berces, *J. Am. Chem. Soc.*, *115*, 636 (1993). (d) L. Versluis, T. Ziegler, E. J. Baerends, and W. Ravenek, *J. Am. Chem. Soc.*, *111*, 2018 (1989). (e) L. Fan and T. Ziegler, *J. Am. Chem. Soc.*, *114*, 10890 (1992). (f) T. Ziegler, E. Folga, and A. Berces, *J. Am. Chem. Soc.*, *115*, 636 (1993). (g) T. Ziegler, V. Tschinke, E. J. Baerends, J. G. Snijders, and W. Ravenek, *J. Phys. Chem.*, *93*, 3050 (1989). (h) T. Ziegler, V. Tschinke, L. Versluis, E. J. Baerends, and W. Ravenek, *Polyhedron*, *7*(16), 1625 (1988).
37. (a) D. R. Salahub, in *Ab Initio Methods in Quantum Chemistry–II* (K. P. Lawley, ed.), Wiley, 1987, p. 447. (b) D. R. Salahub, in *Ab Initio Methods*

in Quantum Chemistry–II (K. P. Lawley, ed.) Wiley, 1987, p. 447. (c) J. Ushio, I. Papai, A. St-Amant, and D. R. Salahub, *Surf. Sci. Lett.*, *262*, L134 (1992). (d) R. Fournier, J. Andzelm, A. Goursot, N. Russo, and D. R. Salahub, *J. Chem. Phys.*, *93*(4), 2919 (1990). (e) V. B. Malkin, O. L. Malkina, and D. R. Salahub, *Chem. Phys. Lett.*, *221*, 91 (1994). (f) I. Pápai, A. Goursot, A. St-Amant, and D. R. Salahub, *Theo. Chim. Acta*, 1991. (g) A. Rochefort, J. Andzelm, N. Russo, and D. R. Salahub, *J. Am. Chem. Soc.*, *112*, 8239 (1990). (h) I. Pápai, J. Ushio, and D. R. Salahub, *Surf. Sci.*, *282*, 262 (1993). (i) I. Pápai, A. St-Amant, and D. R. Salahub, *Surf. Sci. Lett.*, *240*, L604 (1990). (j) I. P. Goursot and D. R. Salahub, *J. Am. Chem. Soc.*, *114*, 7452 (1992). (k) I. Pápai, D. R. Salahub, and C. Mijoule, *Surf. Sci.*, *236*, 241 (1990). (l) R. Fournier, and D. R. Salahub, *Surf. Sci.*, *245*, 263 (1991). (m) I. Pápai, J. Mink, R. Fournier, and D. R. Salahub, *J. Phys. Chem.*, *97*, 9986 (1993). (n) R. Fournier and D. R. Salahub, *Int. J. Quant. Chem.*, *29*, 1077 (1986). (o) P. Mlynarski and D. R. Salahub, *J. Chem. Phys.*, *95*(8), 6050 (1991). (p) N. A. Baykara, J. Andzelm, and D. R. Salahub, *Int. J. Quant. Chem.*, *29*, 1025 (1986). (q) D. R. Salahub, M. Castro, R. Fournier, P. Calaminici, N. Godbout, A. Goursot, C. Jamorski, H. Kobayashi, A. Martinez, I. Papai, E. Proynv, N. Russo, S. Sirois, J. Ushio, and A. Vela, in *Theoretical and Computational Approaches to Interface Phenomena* (H. Sellers and J. T. Golab, eds.), 1994.

38. R. Ahlrichs, P. Scharf, and C. Ehrhardt, *J. Chem. Phys.*, *82*, 890 (1985).
39. D. P. Chong and S. R. Langhoff, *J. Chem. Phys.*, *84*, 5606 (1986).
40. Overview of HF, MBPT, CC, MCSCF techniques, in A. Szabo and N. S. Ostlund, eds., *Modern Quantum Chemistry: An Introduction to Advanced Electronic Structure Theory*, Macmillan, New York, 1992.
41. (a) K. Balasubramanian, P. Y. Feng, and M. Z. Liao, *J. Chem. Phys.*, *87*(7), 3981 (1987). (b) K. Balasubramanian, P. Y. Feng, and M. Z. Liao, *J. Chem. Phys.*, *88*(11), 6955 (1988). (c) K. Balasubramanian, *J. Phys. Chem.*, *93*, 6585 (1989). (d) D. Dai and K. Balasubramanian, *J. Chem. Phys.*, *100*(6), 4401 (1994).
42. R. G. Parr and W. Yang, *Density Functional Theory of Atoms and Molecules*, Oxford Univ. Press, New York, 1989.
43. L. H. Thomas, *Proc. Camb. Phil. Soc.*, *26*, 376 (1926). E. Fermi, *Z. Phys.*, *48*, 542 (1926).
44. P. Hohenberg and W. Kohn, *Phys. Rev.*, *136*, B864 (1964).
45. W. Kohn and L. J. Sham, *Phys. Rev.*, *140*, A1133 (1965).
46. T. Ziegler, *Chem. Rev.*, *91*, 651 (1991).
47. *Density Functional Methods in Chemistry* (J. Labanowski and J. Andzelm, eds.), Springer, New York, 1991.
48. (a) E. J. Baerends and P. Ros, *Int. J. Quant. Chem., Quant. Chem. Symp.*, *12*, 340, 169 (1978). E. J. Baerends, D. E. Ellis, and P. Ros, *Chem. Phys.*, *2*, 41 (1973). E. J. Baerends, D. E. Ellis, and P. Ros, *Chem. Phys.*, *2*, 52 (1973). E. J. Baerends, D. E. Ellis, and P. Ros, *Chem. Phys.*, *8*, 412 (1975). P. M., G. te Velde, and E. J. Baerends, *Int. J. Quant. Chem.*, *33*, 87 (1988). (b) J. Andzelm and E. Wimmer, *J. Chem. Phys.*, *96*(2), 1280 (1992). C. Sosa, J. Andzelm, B. C. Elkin, E. Wimmer, K. Dobbs, and D. A. Dixon, *J. Phys. Chem.*, *96*, 6630 (1992). (c) B. Delley, *J. Chem. Phys.*, *92*, 508 (1990). (d)

A. St.-Amont and D. R. Salahub, *Chem. Phys. Lett.*, *169*, 387 (1990). D. R. Salahub, R. Fournier, P. Mlyunarski, I. Papai, A. St.-Amant, and J. Ushio, in *Density Functional Methods in Chemistry*, Springer, New York, 1991. (e) B. G. Johnson, P. M. W. Gill, and J. A. Pople, *J. Chem. Phys.*, *98*(7), 5612 (1993). B. G. Johnson, P. M. W. Gill, and J. A. Pople, *J. Chem. Phys.*, *97*(10), 7846 (1992).

49. (a) D. M. Cox, A. Kaldor, P. Fayet, W. Eberhardt, R. Brickman, R. Sherwood, Z. Fu, and D. Sondericher, ACS Symp. Ser. 437, Novel Mat. Heter. Catal. 172, 1990. (b) A. Kaldor and D. M. Cox, *High Temp. Sci.*, *27*, 1 (1990). (c) A. Kaldor and D. M. Cox, *Pure Appl. Chem.*, *62*(1), 79 (1990). (d) D. M. Cox, M. R. Zakin, and A. Kaldor, NATO ASI Ser. 158, in *Physical Chemistry of Small Clusters*, *741* (1987). (e) R. L. Whetten, D. M. Cox, D. F. Trevor, and A. Kaldor, *Phys. Rev. Lett.*, *54*, 1494 (1985).
50. (a) P. E. M. Siegbahn, U. Wahlgren, and E. Shustorovich, in *Metal–Surface Reaction Energetics: Theory and Applications to Heterogeneous Catalysis, Chemisorption, and Surface Diffusion*, VCH, New York, 1991. (b) P. E. M. Siegbahn and U. Wahlgren, *Int. J. Quant. Chem.*, *42*, 1149 (1992). (c) G. L. Estiu and M. C. Zerner, *Int. J. Quant. Chem.: Quant. Chem. Symp.*, *27*, 195 (1993). (d) G. L. Estiu and M. C. Zerner, *J. Phys. Chem.*, *98*, 9972 (1994). (e) C. Mijoule, Y. Bouteiller, and D. R. Salahub, *Surf. Sci.*, *253*, 375 (1991). (f) C. Mijoule, M. F. Baba, and V. Russier, *J. Molec. Catal.*, *83*, 367 (1993). (g) V. Russier and C. Mijoule, *J. Phys. Chem.*, *96*, 7579 (1992). (h) V. Russier, D. R. Salahub, and C. Mijoule, *Phys. Rev. B*, *42*, 5046 (1990). (i) M. Castro and D. R. Salahub, *Phys. Rev. B*, *49*(17), 11842 (1993). (j) L. Goodwin and D. R. Salahub, *Phys. Rev. A*, *47*(2), 774 (1993). (k) A. Rochefort, J. Andzelm, N. Russo, and D. R. Salahub, *J. Am. Chem. Soc.*, *112*, 8239 (1990).
51. P. Madlowen and J. Whitten, *J. Chem. Phys.*, *77*, 2673 (1982).
52. (a) M. R. Blomberg, K. Brandemark, and P. E. M. Siegbahn, *J. Am. Chem. Soc.*, *105*, 5557 (1983). (b) M. R. Blomberg, P. E. M. Siegbahn, K. Nagashima, and J. Wennerberg, *J. Am. Chem. Soc.*, *113*, 424 (1991).
53. W. Biemolt, G. J. C. S. Kerkhof, P. R. Davies, A. P. J. Jansen, and R. A. van Santen, *Chem. Phys. Lett.*, *188*, 477 (1992).
54. M. Neurock, D. A. Dixon, and G. W. Coulston, 1994 (in preparation).
55. (a) C. Pisani and R. Dovesi, *Int. J. Quant. Chem.*, *17*, 501 (1980). (b) R. Dovesi, C. Pisani, C. Roetti, and B. Silvi, *J. Chem. Phys.*, *86*, 6967 (1987). (c) R. Dovesi, C. Pisani, C. Roetti, and V. R. Saunders, *Phys. Rev. B*, *28*, 5781 (1987).
56. (a) E. H. Teunissen, C. Roetti, C. Pisani, A. J. M. de Man, A. P. J. Jansen, R. Orlando, R. A. van Santen, and R. Dovesi, *Mod. Sim. Mat. Sci. Eng.*, *2*, 921 (1994). (b) E. H. Teunissen, A. P. J. Jansen, R. A. van Santen, and R. Orlando, *J. Phys. Chem.* (accepted). (c) R. Dovesi, R. Orlando, F. Ricca, and C. Roetti, *Surf. Sci.*, *186*, 267 (1987). (d) M. R. Thompson, A. C. Hess, J. B. Nicholas, J. C. White, J. Anchell, and J. R. Ebner, in *New Developments in Selective Oxidation II*, Elsevier Science, Amsterdam, 1994, p. 167. (e) J. E. Jaffe and A. C. Hess, *Condens. Mat.*, *48*(11), 7903 (1993). (f) C. A. Scamehorn, A. C. Hess, and M. I. Mc Carthy, *J. Chem. Phys.*, *99*(4), 2786(1993).
57. M. P. Teter, M. C. Payne, and D. C. Allan, *Phys. Rev. Lett.*, *55*, 2471 (1985).

58. (a) G. te Velde and E. J. Baerends, *Phys. Rev. B*, *44*, 7888 (1991). (b) G. te Velde and E. J. Baerends, *Chem. Phys.*, *177*, 399 (1993).
59. (a) P. J. Feibelman, *Surf. Sci.*, *313*, L801 (1994). (b) P. J. Feibelman, *Phys. Rev. Lett.*, *67*(4), 461 (1991). (c) J. C. Boettger, *Int. J. Quant. Chem.: Quant. Chem. Symp.*, *27*, 147 (1993). (d) B. Hammer, K. W. Jacobsen, and J. K. Norskov, *Phys. Rev. Lett.*, *69*(13), 1971 (1992). (e) J. R. Chelikowsky, S. G. Louie, D. Vanderbilt, and C. T. Chain, *Int. J. Quant. Chem. Symp.*, *18*, 105 (1984). (f) M. Y. Chou and J. R. Chelikosky, *Phys. Rev. Lett.*, *59*, 1737 (1987). (g) M. Y. Chou and J. R. Chelikosky, *Phys. Rev. B*, *39*, 5623 (1989). (h) Y. Wang, S. W. Mahler, and R. J. Kasowski, *J. Chem. Phys.*, *87*, 7315 (1987).
60. (a) P. Bagus and K. Hermann, *Phys. Rev. B*, *33*, 2987 (1986). (b) P. S. Bagus, C. J. Nelin, and Ph. Avouris, *J. Vac. Sci. Technol.*, *5*(4), 701 (1987). (c) P. S. Bagus and F. Illas, *Phys. Rev. B*, *42*(17), 10852 (1990). (d) P. S. Bagus and F. Illas, *Chem. Phys. Lett.*, *224*, 576 (1994).
61. R. A. van Santen, M. C. Zonnevylle, and A. P. J. Jansen, *Phil. Trans. Roy. Soc.*, *A341*, 269 (1992).
62. (a) M. W. Roberts, *J. Molec. Catal.*, *74*, 11 (1993). (b) B. Afsin, P. R. Davies, A. Pashusky, M. W. Roberts, and D. Vincent, *Surf. Sci.*, *284*, 109 (1993). (c) A. Boronin, A. Pashusky, and M. W. Roberts, *Catal. Lett.*, *16*, 345 (1992).
63. (a) J. K. Norskov, *Prog. Surf. Sci.*, *38*, 2 (1991). (b) P. Stoltze and J. K. Norskov, *Phys. Rev. Lett.*, *55*, 2502 (1985). (c) P. Stoltze and J. K. Norskov, *J. Catal.*, *110*, 110 (1988).
64. R. A. van Santen, *J. Chem. Soc. Far. Trans.*, *I*, *83*, 1915 (1987).
65. G. Blyholder, *J. Phys. Chem.*, *68*, 2772 (1964).
66. (a) J. W. Gadzuk, *J. Vac. Techn.*, *12*, 90 (1975). (b) J. W. Gadzuk, *Phys. Rev. B*, *14*, 2267 (1976). (c) N. D. Lange and A. R. Williams, *Phys. Rev. B*, *18*, 616 (1978). (d) N. D. Lange and A. R. Williams, *Phys. Rev. Lett.*, *37*, 212 (1976). (e) N. H. March, Plenum Press, 1986.
67. J. E. Inglesfield, *Prog. Surf. Sci.*, *20*, 105 (1985).
68. (a) R. A. van Santen, *Catal. Lett.*, *16*, 59 (1992). (b) R. A. van Santen, in *Fundamental Aspects of Heterogeneous Catalysis Studied by Particle Beams* (H. H. Brongersma and R. A. van Santen, eds.), Plenum, New York, 1991, p. 83.
69. K. Tanaka and K. Tamara, *J. Catal.*, *2*, 366 (1963).
70. A. Chattopadhyay, H. Yang, and J. L. Whitten, *J. Phys. Chem.*, *94*, 6379 (1990).
71. C. T. Au and M. W. Roberts, *Chem. Phys. Lett.*, *74*(3), 472 (1982).
72. H. Sambe and R. H. Felton, *J. Chem. Phys.*, *62*, 1122 (1975).
73. S. H. Vosko, L. Wile, and M. Nusair, *Can. J. Phys.*, *58*, 1200 (1980).
74. (a) A. D. Becke, *Phys. Rev. A*, *38*, 3098 (1988). (b) A. D. Becke, *ACS Symp. Ser.*, *394*, 165 (1989).
75. J. P. Perdew, *Phys. Rev. B*, *33*, 8822 (1986).
76. (a) W. Biemolt, G. J. C. S. Kerkhof, P. R. Davies, A. P. J. Jansen, and R. A. van Santen, *Chem. Phys. Lett.*, *188*, 477 (199). (b) M. Neurock, R. A. van Santen, W. Biemolt, and A. P. J. Jansen, *J. Am. Chem. Soc.*, *116*, 6860 (1994).

77. P. E. M. Siegbahn and I. Panas, *Surf. Sci.*, *240*, 37 (1990).
78. J. Schüle, P. E. M. Siegbahn, and U. Wahlgren, *J. Chem. Phys.*, *89*, 6982 (1988).
79. H. Yang and J. L. Whitten, *J. Am. Chem. Soc.*, *113*, 6442 (1991).
80. H. Burghgraef, A. P. J. Jansen, and R. A. van Santen, *Surf. Sci.*, 1995 (accepted).
81. C. Zheng, Y. Apeloig, and R. Hoffmann, *J. Am. Chem. Soc.*, *110*(3), 749 (1988).
82. A. de Koster and R. A. van Santen, *J. Catal.*, *127*, 141 (1991).
83. C. Minot, M. A. van Hove, and G. A. Somorjai, *Surf. Sci.*, *127*, 441 (1982).
84. E. M. Stuve and R. J. Madix, *J. Phys. Chem.*, *89*, 105 (1985).
85. P. Sautet and J. F. Paul, *Catal. Lett.*, *9*, 245 (1991).
86. A. de Koster, A. P. J. Jansen, R. A. van Santen, and H. Geerlings, *Far. Disc. Chem. Soc.*, *87*, 221 (1989).
87. P. Hollins and J. Pritchard, *Prog. Surf. Sci.*, *19*, 275 (1985).
88. K. Coulter, X. Xu, and D. W. Goodman, *J. Phys. Chem.*, *98*, 1245 (1994).
89. C. Backx and C. P. M. de Groot, unpublished results.
90. M. Neurock, G. W. Coulston, and D. A. Dixon, in preparation.
91. E. Wimmer, C. L. Fu, and A. J. Freeman, *Phys. Rev. Lett.*, *55*, 2618 (1985).
92. G. te Velde and E. J. Baerends, *Chem. Phys.*, *177*, 399 (1993).
93. A. Goursot, I. Papai, and D. R. Salahub, *J. Am. Chem. Soc.*, *114*, 7452 (1992).
94. M. C. Zonnevylle, J. J. C. Geerlings, and R. A. van Santen, *J. Catal.*, *148*, 417 (1994).
95. (a) P. Bagus and K. Hermann, *Phys. Rev. B*, *33*, 2987 (1986). (b) J. M. Ricart, J. Rubio, F. Illas, and P. S. Bagus, *Surf. Sci.*, *304*, 335 (1994).
96. (a) L. Ackermann, N. Rösch, B. I. Dunlap, and G. Pacchioni, *Int. J. Quant. Chem.: Chem. Symp.*, *26*, 605 (1992). (b) G. Pacchioni and J. Koutecky, *J. Phys. Chem.*, *91*, 2658 (1987). (c) G. Pacchioni and N. Rösch, *Surf. Sci.*, *306*, 169 (1994).
97. M. R. A. Blomberg, C. B. Lebrilla, and P. E. M. Siegbahn, *Chem. Phys. Lett.*, *150*(6), 522 (1988).
98. F. Raatz and D. R. Salahub, *Surf. Sci.*, *176*, 219 (1986).
99. C. W. Bauschlicher, Jr., *J. Chem. Phys.*, *101*(4), 3250 (1994).
100. R. Hoffmann, *Rev. Mod. Phys.*, *60*(3), 601 (1988).
101. (a) K. C. Prince and A. M. Bradshaw, *Surf. Sci.*, *126*, 49 (1983). (b) W. A. Fraser, J. V. Florio, W. N. Delgass, and W. D. Robertson, *Surf. Sci.*, *36*, 661 (1973).
102. F. H. P. M. Habraken, E. Ph. Kiefer, and B. A. Bootsma, *Surf. Sci.*, *83*, 45 (1979).
103. C. Backx, C. P. M. de Groot, and P. Biloen, *Surf. Sci.*, *104*, 300 (1981).
104. C. R. Fischer and J. L. Whitten, *Phys. Rev. B*, *40*(8), 5745 (1989).
105. H. Nakatsuji, H. Nakai, and Y. Fukunishi, *J. Chem. Phys.*, *95*(1), 640 (1991).
106. D. A. Outka, J. Stöhr, W. Jark, P. Stevens, J. Salomons, and R. J. Madix, *Phys. Rev. B*, *35*, 4119 (1987).
107. I. Panas and P. Siegbahn, *Chem. Phys. Lett.*, *153*(5), 458 (1988).
108. J. L. Gland, B. A. Sexton, and G. B. Fisher, *Surf. Sci.*, *95*, 587 (1980).
109. P. V. Kamath and C. N. R. Rao, *J. Phys. Chem.*, *88*, 464 (1984).

110. P. S. Bagus and F. Illas, *Chem. Phys. Lett.*, *224*, 576 (1994).
111. M. A. van Daelen, Y. S. Li, J. M. Newsam, and R. A. van Santen, *Chem. Phys. Lett.*, *226*, 100 (1994).
112. P. S. Bagus, C. J. Nelin, and Ph. Avouris, *J. Vac. Sci. Techn. A*, *5*(3), 701 (1987).
113. M. Fernández-Garciá and J. C. Conesa, *Surf. Sci.*, *280*, 441 (1993).
114. Neyman and Rösch, *Surf. Sci.*, *307*, 1193 (1994).
115. (a) T. V. W. Janssens, J. W. Niemantsverdriet, and R. A. van Santen, *J. Chem. Phys.*, *101*, 2995 (1994). (b) T. V. W. Janssens, K. Wandelt, and J. M. Niemantsverdriet, *Catal. Lett.*, *19*, 263 (1993).
116. (a) W. Ravenek, A. P. J. Jansen, and R. A. van Santen, *J. Phys. Chem.*, *93*, 6445 (1989). (b) A. P. J. Jansen and R. A. van Santen, *J. Phys. Chem.*, *94*, 6764 (1990). (c) E. Sanchez Marcos, A. P. J. Jansen, and R. A. van Santen, *Chem. Phys. Lett.*, *167*, 399 (1990). (d) M. Baba, C. Mijoule, N. Godbout, and D. R. Salahub, *Surf. Sci.*, 1994 (in press).
117. (a) J. K. Norskov, *Rep. Progr. Phys.*, *53*, 1253 (1990). (b) J. K. Norskov, in *The Chemical Physics of Solid Surfaces and Heterogeneous Catalysis* (D. A. King and D. P. Woodruff, eds.), Elsevier, 1993, Vol. 6. (c) J. K. Norskov, *Surf. Sci.*, *299/300*, 690 (1994).
118. (a) G. A. Somorjai and M. A. van Hove, *Progr. Surf. Sci.*, *30*, 201 (1989). (b) M. A. van Hove, *Surf. Sci.*, *299/300* (1994). (c) G. Ertl, *Surf. Sci.*, *152/153*, 328 (1985).
119. G. J. C. S. van de Kerkhof, W. Biemolt, A. P. J. Jansen, and R. A. van Santen, *Surf. Sci.*, *284*, 361 (1993).
120. T. Koerts, W. J. J. Welters, and R. A. van Santen, *J. Catal.*, *134*, 1 (1992).
121. W. M. H. Sachtler and R. A. van Santen, *Adv. Catal.*, *26*, 69 (1977).
122. T. H. Upton, P. Stevens, and R. J. Madix, *J. Chem. Phys.*, *88*, 3988 (1988).
123. K. J. Laidler, *Theories of Chemical Reaction Rates*, McGraw-Hill, New York, 1969.
124. C. T. Campbell, Y. K. Sun, and W. H. Weinberg, *Chem. Phys. Lett.*, *179*, 53 (1991).
125. (a) H. Burghgraef, A. P. J. Jansen, and R. A. van Santen, *J. Chem. Phys.*, *98*(11), 8810 (1993). (b) H. Burghgraef, A. P. J. Jansen, and R. A. van Santen, *Chem. Phys.*, *177*, 407 (1993).
126. T. P. Beebe, D. W. Goodman, B. D. Kay, and J. T. Yates, *J. Chem. Phys.*, *87*, 2305 (1987).
127. (a) C. T. Au and M. W. Roberts, *Nature*, *319*, *206* (1986). (b) B. Apin, P. R. Davies, A. Pashusky, and M. W. Roberts, *Surf. Sci. Lett.*, *259*, L724 (1991). (c) A. Boronin, A. Pashusky, and M. W. Roberts, *Catal. Lett.*, *16*, 345 (1992).
128. W. Biemolt, A. P. J. Jansen, M. Neurock, G. J. C. S. van de Kerkhof, and R. A. van Santen, *Surf. Sci.*, *287/288*, 183 (1993).
129. (a) S. T. Ceyer, J. Beckerle, M. B. Lee, S. L. Tang, Q. Y. Yang, and M. A. Hines, *J. Vac. Sci. Techn.*, *A*, *5*, 501 (1987). (b) M. B. Lee, Q. Y. Yang, and S. T. Ceyer, *J. Chem. Phys.*, *87*, 2724 (1987).
130. V. P. Zhdanov, *Surf. Sci. Rep.*, *12*, 183 (1991).
131. R. A. van Santen and H. P. E. Kuipers, *Adv. Catal.*, *35*, 265 (1987).
132. R. A. van Santen and C. P. M. de Groot, *J. Catal.*, *98*, 530 (1986).

133. P. A. Kilty and W. M. H. Sachtler, *Catal. Rev. Sci. Eng.*, *10*, 1 (1974).
134. R. A. van Santen, J. Moolhuysen, and W. M. H. Sachtler, *J. Catal.*, *65*, 478 (1980).
135. P. van den Hoek, E. J. Baerends, and R. A. van Santen, *J. Phys. Chem.*, *93*, 6469 (1989).
136. P. Biloen and W. M. H. Sachtler, *Adv. Catal.*, *30*, 165 (1981).
137. T. Koerts and R. A. van Santen, *J. Mol. Catal.*, *70*, 119 (1991).
138. R. A. van Santen, A. de Koster, and T. Koerts, *Catal. Lett.*, *7*, 1 (1990).
139. (a) T. Koerts and R. A. van Santen, *J. Chem. Soc. Comm.*, *18*, 1281 (1991). (b) T. Koerts, M. J. A. G. Deelen, and R. A. van Santen, *J. Catal.*, *138*, 101 (1992).
140. J. Moulijn, P. W. N. M. van Leeuwen, and R. A. van Santen, *Catalysis and Integrated Approach*, Elsevier, Amsterdam, 1993.
141. F. H. P. M. Habraken, E. Ph. Kiefer, and G. A. Bootsma, *Surf. Sci.*, *83*, 45 (1979).
142. K. J. Wu and S. D. Kevan, *J. Chem. Phys.*, *94*, 7494 (1991).
143. T. S. Chuang, H. Seki, and I. Hussla, *Surf. Sci.*, *158*, 525 (1985).
144. B. J. Hinch and L. H. Dubois, *J. Chem. Phys.*, *96*(4), 3262 (1992).
145. J. M. Heras, M. C. Asensio, and L. Z. Visido, *Phys. Chem. Neue. Folge.*, *160*, 199, 1986 (est. adsorption energy).
146. R. A. van Santen and A. de Koster, in *New Trends in CO Activation* (L. Guczi, ed.), Elsevier, Amsterdam, 1991, p. 1.

Tables 1 and 2

T1. A. T. Bell, in *Metal–Surface Reaction Energetics: Theory and Applications to Heterogeneous Catalysis, Chemisorption, and Surface Diffusion*, VCH, New York, 1991, p. 191.
T2. J. Benzinger, in *Metal–Surface Reaction Energetics: Theory and Applications to Heterogeneous Catalysis, Chemisorption, and Surface Diffusion*, VCH, New York, 1991.
T3. P. Paredes Olivera, E. M. Patrito, and H. Sellers, *Surf. Sci.*, *313*, 25 (1994).
T4. E. M. Patrito, P. Paredes Olivera, and H. Sellers, *Surf. Sci.*, *294*, 99 (1993).
T5. H. Sellers, *Surf. Sci.*, *310*, 281.
T6. H. Sellers, *Surf. Sci.*, *306*, 447 (1994).
T7. E. Shustorovich and A. T. Bell, *Surf. Sci.*, *253*, 386 (1991).
T8. E. Shustorovich and A. T. Bell, *J. Catal.*, *113*, 341 (1988).
T9. E. Shustorovich and A. T. Bell, *Surf. Sci.*, *268*, 397 (1992).
T10. E. Shustorovich, in *Quantum Chemistry Approaches to Chemisorption and Heterogeneous Catalysis* (F. Ruette, ed.), Kluwer, Netherlands, 1992.
T11. P. Sautet and J. F. Paul, *Catal. Lett.*, *9*, 245 (1991).
T12. C. Minot, M. A. van Hove, and G. A. Somorjai, *Surf. Sci.*, *127*, 441 (1982).
T13. C. Y. Zheng, Apeloig, and R. Hoffmann, *J. Am. Chem. Soc.*, *110*(3), 749 (1988).
T14. J. Y. Saillard and R. Hoffmann, *J. Am. Chem. Soc.*, *106*, 2006 (1984).
T15. S. S. Sung and R. Hoffmann, *J. Chem. Soc. Farad. Trans.*, *86*, 553 (1985).
T16. S. S. Sung, R. Hoffmann, and P. A. Thiel, *J. Phys. Chem.*, *90*, 1380 (1986).

T17. A. B. Anderson and S. J. Choe, *J. Phys. Chem.*, *93*, 6145 (1989).
T18. D. Simon and B. Bigot, *Surf. Sci.*, *306*, 459 (1994).
T19. S. C. Richtsmeier, J. L. Gole, and D. A. Dixon, *Proc. Natl. Acad. Sci.*, *77*(10), 5611 (1980).
T20. S. C. Richtsmeier, J. L. Gole, and D. A. Dixon, *J. Phys. Chem.*, *86*, 3937 (1982).
T21. S. C. Richtsmeier, J. L. Gole, and D. A. Dixon, in *Metal Bonding and Interactions*, ACS Series 177, 1980.
T22. G. L. Estiu and M. C. Zerner, *Int. J. Quant. Chem.: Quant. Chem. Symp.*, *27*, 195 (1993).
T23. G. L. Estiu and M. C. Zerner, *J. Phys. Chem.*, *97*(51), 13720 (1993).
T24. G. L. Estiu and M. C. Zerner, *J. Phys. Chem.*, *98*, 9972 (1994).
T25. T. H. Upton and W. A. Goddard, *CRC Crit. Rev. Solid State Mater. Sci.*, *261* (1981).
T26. T. H. Upton, P. Stevens, R. J. Madix, *J. Chem. Phys.*, *88*(6), 3988 (1988).
T27. J. J. Low and W. A. Goddard III, *J. Am. Chem. Soc.*, *106*, 8321 (1984).
T28. H. Zakharov, V. I. Avdeev, and G. M. Zhidomirov, *Surf. Sci.*, *277*, 407 (1992).
T29. G. Ohanessian and W. A. Goddard III, *Acc. Chem. Res.*, *23*, 386 (1990).
T30. E. V. Anslyn and W. A. Goddard III, *Organomett*, *8*, 1550 (1989).
T31. E. Carter and W. A. Goddard, *J. Catal.*, *112*, 80 (1988).
T32. E. Carter and W. A. Goddard, *Surf. Sci.*, *209*, 243 (1989).
T33. E. Carter and W. A. Goddard, *J. Phys. Chem.*, *92*, 2109 (1988).
T34. M. H. McAdon and W. A. Goddard III, *J. Phys. Chem.*, *91*, 2607 (1987).
T35. M. H. McAdon and W. A. Goddard III, *J. Phys. Chem.*, *92*, 1352 (1988).
T36. M. R. A. Blomberg and P. E. M. Siegbahn, *J. Chem. Phys.*, *78*(9), 5682 (1983).
T37. P. E. Siegbahn, M. R. A. Blomberg, and C. W. Bauschlicher, Jr., *J. Chem. Phys.*, *81*(4), 2103 (1984).
T38. V. R. Jensen and P. E. M. Siegbahn, *Chem. Phys. Lett.*, *212*(3,4), 353 (1993).
T39. S. A. Mitchell, M. A. Blitz, P. E. M. Siegbahn, and M. Svensson, *J. Chem. Phys.*, *100*(1), 423 (1994).
T40. P. E. Siegbahn and U. Wahlgren, *Int. J. Quant. Chem.*, *42*, 1149 (1992).
T41. M. R. A. Blomberg, P. E. M. Siegbahn, and M. Svensson, *J. Phys. Chem.*, *96*, 5783 (1992).
T42. J. E. Backvall, E. E. Bjorkman, L. Pettersson, P. Siegbahn, and A. Strich, *J. Am. Chem. Soc.*, *107*, 7408 (1985).
T43. I. Panas, P. Siegbahn, and U. Wahlgren, *J. Chem. Phys.*, *90*(11), 6791 (1989).
T44. M. R. A. Blomberg, P. E. M. Siegbahn, U. Nagashima, and J. Wennerberg, *J. Am. Chem. Soc.*, *113*, 424 (1991).
T45. P. E. M. Siegbahn and I. Panas, *Surf. Sci.*, *240*, 37 (1990).
T46. P. E. M. Siegbahn, M. R. A. Blomberg, and M. Svensson, *J. Am. Chem. Soc.*, *115*, 1952 (1993).
T47. M. R. A. Blomberg, P. E. M. Siegbahn, and M. Svensson, *J. Phys. Chem.*, *96*, 9794 (1992).
T48. P. E. M. Siegbahn, *Theor. Chim. Acta*, *87*, 277 (1994).

T49. P. E. M. Siegbahn and M. R. A. Blomberg, *Organmet.*, *13*, 354 (1994).
T50. P. E. M. Siegbahn, *J. Am. Chem. Soc.*, *115*, 5803 (1993).
T51. M. R. A. Blomberg, P. E. M. Siegbahn, and J. E. Backvall, *J. Am. Chem. Soc.*, *109*, 4456 (1987).
T52. P. E. M. Siegbahn, M. R. A. Blomberg, and M. Svensson, *J. Am. Chem. Soc.*, *115*, 4191 (1993).
T53. P. E. M. Siegbahn and M. Svensson, *Chem. Phys. Lett.*, *216*(1,2), 147 (1993).
T54. P. E. M. Siegbahn, M. A. Nygren, and U. Wahlgren, in *Cluster Models for Surface and Bulk Phenomena* (G. Pacchioni, P. S. Bagus, and F. Parmigiani, eds.), NATO ASI Series 267, 1991.
T55. M. R. A. Blomberg, C. A. M. Karlsson, and P. E. M. Siegbahn, *J. Phys. Chem.*, *97*, 9341 (1993).
T56. M. R. A. Blomberg, P. E. M. Siegbahn, and M. Svensson, *J. Phys. Chem.*, *98*(8), 2063 (1994).
T57. M. R. A. Blomberg, C. B. Lebrilla, and P. E. M. Siegbahn, *Chem. Phys. Lett.*, *150*(6), 522 (1988).
T58. M. Blomberg, U. Brandemark, L. Pettersson, and P. Siegbahn, *Int. J. Quant. Chem.*, *23*, 855 (1983).
T59. P. E. M. Siegbahn and M. R. A. Blomberg, *J. Am. Chem. Soc.*, *114*, 10548 (1992).
T60. M. R. A. Blomberg, P. E. M. Siegbahn, and M. Svensson, *Inorg. Chem.*, *32*, 4218 (1993).
T61. M. R. A. Blomberg and P. E. M. Siegbahn, *J. Am. Chem. Soc.*, *115*, 6908 (1993).
T62. K. Hermann, M. Witko, L. G. M. Pettersson, and P. Siegbahn, *J. Chem. Phys.*, *99*(1), 610 (1993).
T63. P. S. Bagus and F. Illas, *Chem. Phys. Lett.*, *224*, 576 (1994).
T64. P. S. Bagus and F. Illas, *Phys. Rev. B*, *42*(17), 10852 (1990).
T65. P. S. Bagus, C. J. Nelin, and Ph. Avouris, *J. Vac. Sci. Technol.*, *5*(4), 701 (1987).
T66. P. S. Bagus and G. Pacchioni, in *Cluster Models for Surface and Bulk Phenomena* (G. Pacchioni, P. S. Bagus, and F. Parmigiani, eds.), NATO ASI Series, 1991.
T67. J. M. Ricart, J. Rubio, F. Illas, and P. S. Bagus, *Surf. Sci.*, *304*, 335 (1994).
T68. M. Fernández-García and J. C. Conesa, *Surf. Sci.*, *280*, 441 (1993).
T69. F. Illas, M. Bachs, J. Rubio, and J. M. Ricart, *J. Chem. Phys.*, *91*(9), 5466 (1989).
T70. P. Bagus and K. Hermann, *Phys. Rev. B*, *33*, 2987 (1986).
T71. J. M. Ricart, J. Torras, F. Illas, and J. Rubio, *Surf. Sci.*, *307–309*, 107 (1994).
T72. C. W. Bauschlicher, Jr., *J. Chem. Phys.*, *101*(4), 3250 (1994).
T73. K. Hermann, in *Cluster Models for Surface and Bulk Phenomena* (G. Pacchioni, P. S. Bagus, and F. Parmigiani, eds.), NATO ASI Series 209, 1991.
T74. K. Hermann and C. Meyer, *Surf. Sci.*, *277*, 377 (1992).
T75. G. Pacchioni and R. M. Lambert, *Surf. Sci.*, *304*, 208 (1994).
T76. G. Pacchioni and J. Koutecky, *J. Phys. Chem.*, *91*, 2658 (1987).
T77. G. Pacchioni and J. Koutecky, in *The Challenge of Transition Metals and*

Coordination Chemistry (A. Veillard, ed.), D. Reidel, 1986, p. 465.
T78. C. R. Fischer and J. L. Whitten, *Phys. Rev. B*, *40*(8), 40 (1989).
T79. A. Chattopadhyay, H. Yang, and J. L. Whitten, *J. Phys. Chem.*, *94*, 6379 (1990).
T80. H. Yang, J. L. Whitten, R. E. Thomas, R. A. Rudder, and R. Markunas, *Surf. Sci.*, *277*, L95 (1992).
T81. H. Yang and J. L. Whitten, *J. Chem. Phys.*, *91*(1), 126 (1989).
T82. H. Yang, J. L. Whitten, and C. M. Friend, *Surf. Sci.*, *313*, 295 (1994).
T83. J. Whitten, in *Cluster Models for Surface and Bulk Phenomena* (G. Pacchioni, P. S. Bagus, and F. Parmigiani, eds.), NATO ASI Series 375, 1991.
T84. L. C. Bonacic-Koutecky, P. Fantucci, and J. Koutecky, *J. Chem. Phys.*, *98*, 7981 (1993).
T85. M. L. McKee, *J. Chem. Phys.*, *87*(5), 3143 (1987).
T86. O. Gropen, J. Almlof, and U. Wahlgren, in *Cluster Models for Surface and Bulk Phenomena* (G. Pacchioni, P. S. Bagus, and F. Parmigiani, eds.), NATO ASI Series, 1991.
T87. G. Blyholder and H. Sellers, in *Cluster Models for Surface and Bulk Phenomena* (G. Pacchioni, P. S. Bagus, and F. Parmigiani, eds.), NATO ASI Series, 321, 1991.
T88. H. Sellers, A. Ulman, Y. Shnidman, and J. E. Eilers, in *Cluster Models for Surface and Bulk Phenomena* (G. Pacchioni, P. S. Bagus, and F. Parmigiani, eds.), NATO ASI Series 441, 1991.
T89. H. Nakatsuji and M. Hada, in *Quantum Chemistry: The Challenge of Transition Metals and Coordination Chemistry*, D. Reidel, 1986, p. 477.
T90. H. Nakatsuji, H. Nakai, and Y. Fukunishi, *J. Chem. Phys.*, *95*(1), 640 (1991).
T91. T. R. Cundari, *J. Am. Chem. Soc.*, *116*, 340 (1994).
T92. H. Nakatsuji, M. Hada, and T. Yonezawa, *J. Am. Chem. Soc.*, *109*, 1902 (1987).
T93. K. Balasubramanian, *J. Phys. Chem.*, *93*, 6585 (1989).
T94. K. Balasubramanian, P. Y. Feng, and M. Z. Liao, *J. Chem. Phys.*, *87*(7), 3981 (1987).
T95. K. Balasubramanian, P. Y. Feng, and M. Z. Liao, *J. Chem. Phys.*, *88*(11), 6955 (1988).
T96. D. Dai and K. Balasubramanian, *J. Chem. Phys.*, *100*(6), 4401 (1994).
T97. S. R. Langhoff and C. W. Bauschlicher, Jr., *Ann. Rev. Phys. Chem.*, *39*, 181 (1988).
T98. M. A. Chesters, D. Lennon, L. Ackermann, O. Haberlen, S. Kruger, and N. Rösch, *Surf. Sci.*, *291*, 177 (1993).
T99. K. Neyman and N. Rösch, *Surf. Sci.*, *307–309*, 1193 (1994).
T100. G. Pacchioni and N. Rösch, *Surf. Sci.*, *306*, 169 (1994).
T101. L. Ackermann, N. Rösch, B. I. Dunlap, and G. Pacchioni, *Int. J. Quant. Chem.: Chem. Symp.*, *26*, 605 (1992).
T102. N. Rösch, in *Cluster Models for Surface and Bulk Phenomena* (G. Pacchioni, P. S. Bagus, and F. Parmigiani, eds.), NATO ASI Series, 1991.
T103. G. Pacchioni, S. C. Chung, S. Krüger, and N. Rösch, *Chem. Phys.*, *184*, 125 (1994).
T104. L. Fan and T. Ziegler, *J. Am. Chem. Soc.*, *114*, 10890 (1992).

T105. L. Versluis, T. Ziegler, E. J. Baerends, and W. Ravenek, *J. Am. Chem. Soc.*, *111*, 2018 (1989).
T106. T. Ziegler, E. Folga, and A. Berces, *J. Am. Chem. Soc.*, *115*, 636 (1993).
T107. T. Ziegler, W. Cheng, E. J. Baerends, and W. Ravenek, *Inorg. Chem.*, *27*, 3458 (1988).
T108. T. Ziegler, V. Tschinke, E. J. Baerends, J. G. Snijders, and W. Ravenek, *J. Phys. Chem.*, *93*, 3050 (1989).
T109. E. J. Baerends and P. Ros, *Int. J. Quant. Chem., Quant. Chem. Symp. 12*(340), 169 (1978).
T110. E. J. Baerends, in *Cluster Models for Surface and Bulk Phenomena* (G. Pacchioni, P. S. Bagus, and F. Parmigiani, eds.), NATO ASI Series 189, 1991.
T111. T. Ziegler, *Pure Appl. Chem.*, *63*(6), 873 (1991).
T112. T. V. W. Janssens, J. W. Niemantsverdriet, and R. A. van Santen, *J. Chem. Phys.*, *101*(4), 2995 (1994).
T113. M. C. Zonnevylle, J. J. C. Geerlings, and R. A. van Santen, *Surf. Sci.*, *240*, 253 (1990).
T114. H. Burghgraef, A. P. J. Jansen, and R. A. van Santen, *Chem. Phys.*, *177*, 407 (1993).
T115. W. Ravenek, A. P. J. Jansen, and R. A. van Santen, *J. Phys. Chem.*, *93*, 6445 (1989).
T116. W. Biemolt, A. P. J. Jansen, M. Neurock, G. G. C. S. van de Kerkhof, and R. A. van Santen, *Surf. Sci.*, *287/288*, 183 (1993).
T117. G. J. C. S. van de Kerkhof, W. Biemolt, A. P. J. Jansen, and R. A. van Santen, *Surf. Sci.*, *284*, 361 (1993).
T118. W. Biemolt, G. J. C. S. van de Kerkhof, P. R. Davies, A. P. J. Jansen, and R. A. van Santen, *Chem. Phys. Lett.*, *188*(5,6), 477 (1992).
T119. R. A. van Santen, M. C. Zonnevylle, and A. P. J. Jansen, *Phil. Trans. R. Soc. Lond. A*, *341*, 269 (1992).
T120. H. Burghgraef, A. P. J. Jansen, and R. A. van Santen, *Surf. Sci.*, 1994 (accepted).
T121. D. E. Ellis, J. Guo, H. P. Cheng, J. J. Low, *Adv. Quant. Chem.*, *22*, 125 (1991).
T122. A. R. Burns, D. R. Jennison, E. B. Stechel, and Y. S. Li, *Phys. Rev. Lett.*, *72*(24), 3895 (1994).
T123. C. Sosa and C. Lee, *J. Chem. Phys.*, *98*(10), 8004 (1993).
T124. T. Nakao, D. A. Dixon, and H. Chen, *J. Phys. Chem.*, *97*, 12665 (1993).
T125. H. Chen, M. Krasowski, and G. Fitzgerald, *J. Chem. Phys.*, *98*(11), 8710 (1993).
T126. B. G. Johnson, P. M. W. Gill, and J. A. Pople, *J. Chem. Phys.*, *98*(7), 5612 (1993).
T127. V. Russier and C. Mijoule, *J. Phys. Condens. Mat.*, *3*, 3193 (1991).
T128. J. E. Müller, *Surf. Sci.*, *272*, 45 (1992).
T129. C. Mijoule, M. F. Baba, and V. Russier, *J. Molec. Catal.*, *83*, 367 (1993).
T130. R. Santamaris, I. G. Kaplan, and O. Novaro, *Chem. Phys. Lett.*, *218*, 395 (1994).
T131. J. M. Seminario, M. C. Concha, and P. Politzer, *Int. J. Quant. Chem.: Quant. Chem. Symp.*, *27*, 263 (1993).

T132. M. Casarin, G. Granozzi, M. Sambi, and E. Tondello, *Surf. Sci.*, *307–309*, 95 (1994).
T133. F. Mele, N. Russo, and M. Toscano, *Surf. Sci.*, *307–309*, 113 (1994).
T134. D. R. Salahub, in *Ab Initio Methods in Quantum Chemistry-II* (K. P. Lawley, ed.), Wiley, 1987, p. 447.
T135. J. Ushio, I. Pápai, A. St-Amant, and D. R. Salahub, *Surf. Sci. Lett.*, *262*, L134 (1992).
T136. R. Fournier, J. Andzelm, A. Goursot, N. Russo, and D. R. Salahub, *J. Chem. Phys.*, *93*(4), 2919 (1990).
T137. C. Mijoule, Y. Bouteiller, and D. R. Salahub, *Surf. Sci.*, *253*, 375 (1991).
T138. V. B. Malkin, O. L. Malkina, and D. R. Salahub, *Chem. Phys. Lett.*, *221*, 91 (1994).
T139. I. Pápai, A. Goursot, A. St-Amant, and D. R. Salahub, *Theor. Chim. Acta*, 1991.
T140. A. Rochefort, J. Andzelm, N. Russo, and D. R. Salahub, *J. Am. Chem. Soc.*, *112*, 8239 (1990).
T141. I. Pápai, J. Ushi, and D. R. Salahub, *Surf. Sci.*, *282*, 262 (1993).
T142. A. Selmani, J. M. Sichel, and D. R. Salahub, *Surf. Sci.*, *157*, 208 (1985).
T143. M. Castro, D. R. Salahub, and R. Fournier, *J. Chem. Phys.*, *100*(11), 8233 (1994).
T144. I. Pápai, A. St-Amant, and D. R. Salahub, *Surf. Sci. Lett.*, *240*, L604 (1990).
T145. I. P. Goursot and D. R. Salahub, *J. Am. Chem. Soc.*, *114*, 7452 (1992).
T146. I. Pápai, D. R. Salahub, and C. Mijoule, *Surf. Sci.*, *236*, 241 (1990).
T147. R. Fournier and D. R. Salahub, *Surf. Sci.*, *245*, 263 (1991).
T148. I. Pápai, J. Mink, R. Fournier, and D. R. Salahub, *J. Phys. Chem.*, *97*, 9986 (1993).
T149. R. Fournier and D. R. Salahub, *Int. J. Quant. Chem.*, *29*, 1077 (1986).
T150. P. Mlynarski and D. R. Salahub, *J. Chem. Phys.*, *95*(8), 6050 (1991).
T151. F. Raatz and D. R. Salahub, *Surf. Sci.*, *176*, 219 (1986).
T152. N. A. Baykara, J. Andzelm, and D. R. Salahub, *Int. J. Quant. Chem.*, *29*, 1025 (1986).
T153. J. Andzelm, A. Rochefort, N. Russo, and D. R. Salahub, *J. Am. Chem. Soc.*, 1994.
T154. M. Filali Baba, C. Mijoule, N. Godbout, and D. R. Salahub, *Surf. Sci.*, 1994 (accepted).
T155. R. Fournier, N. Russo, D. R. Salahub, and M. Toscano, in *Cluster Models for Surface and Bulk Phenomena* (G. Pacchioni, P. S. Bagus, and F. Parmigiani, eds.), NATO ASI Series 433, 1991.
T156. D. R. Salahub, M. Castro, R. Fournier, P. Calaminici, N. Godbout, A. Goursot, C. Jamorski, H. Kobayashi, A. Martinez, I. Papai, E. Proynv, N. Russo, S. Sirois, J. Ushio, and A. Vela, in *Theoretical and Computational Approaches to Interface Phenomena* (H. Sellers and J. T. Golab, eds.), 1994.
T157. M. Castro and D. R. Salahub, *Phys. Rev. B*, *49*(17), 11842 (1994).
T158. S. Sirois, M. Castro, and D. R. Salahub, *Int. J. Quant. Chem.*, 1994 (accepted).
T159. L. Pedocchi, N. Russo, and D. R. Salahub, *Phys. Rev. B*, *47*(19), 12992 (1993).
T160. L. Goodwin and D. R. Salahub, *Phys. Rev. B*, *47*(2), 774 (1993).

T161. M. Castro and D. R. Salahub, *Phys. Rev. B*, *47*(16), 10955 (1993).
T162. A. Goursot, F. Mele, N. Russo, D. R. Salahub, and M. Toscamo, *Int. J. Quant. Chem.*, *48*, 277 (1993).
T163. S. R. Chubb, E. Wimmer, A. J. Freeman, J. R. Hiskes, and A. M. Karo, *Phys. Rev. B: Conds. Matter*, *36*(8), 4112 (1987).
T164. E. Wimmer, C. L. Fu, and A. J. Freeman, *Phys. Rev. Lett.*, *55*, 2618 (1985).